Second-Order Cyclostationary Feature Based Detection of WiMAX Signals in Pulsed Noise Environments

Joseph M. Davis

Thesis submitted to the Faculty of the
Virginia Polytechnic Institute and State University
in partial fulfillment of the requirements for the degree of

Master of Science
in
Electrical Engineering

Robert W. McGwier, Chair
T. Charles Clancy
Carl B. Dietrich

December 5, 2013
Blacksburg, Virginia

Keywords: WiMAX, OFDM, Cyclostationary Detection, SVM

Second-Order Cyclostationary Feature Based Detection of WiMAX Signals in Pulsed Noise Environments

Joseph M. Davis

(ABSTRACT)

Spectral coexistence and cooperative spectrum sharing techniques are vital to the continued development and proliferation of wireless communications systems. Government directives indicate that certain frequency bands which once were reserved for radar-only applications must now support wireless broadband systems. The effect of co-site interference upon detection techniques for wireless broadband systems is evaluated. Cyclostationary feature based detection methods are evaluated against gaussian noise and interfering radar signals. Alternative decision algorithms utilizing support vector machines are proposed and evaluated and compared against traditional general likelihood ratio test algorithms. Recommendations for certain algorithms and observation window lengths to maximize effectiveness and minimize computational complexity are developed.

This research was funded through Office of Naval Research grant N00014-12-1-0062 and contract N00014-12-C-0702

Acknowledgments

When I left Virginia Tech in 2003 for a tour of duty in the U.S. Air Force, I did not know whether or not I would return to finish my education or where my life would take me. Now through hard work, faith, and the support of my family, friends, coworkers, and the faculty at Virginia Tech I have reached an awesome point in my life. Nearly one decade after I boarded an airplane for San Antonio, I am finishing my M.S. thesis.

I would like to thank my friend Zach Leffke, for introducing me to Dr. Dietrich and Dr. McGwier. Dr. Dietrich introduced me to the problem of co-site interference and coexistence between communications and radar systems with an undergraduate research project. Dr. McGwier and the Ted & Karyn Hume Center at Virginia Tech provided support and guidance during my graduate career.

I also want to recognize the Association of Federal Communications Consulting Engineers (AFCCE). AFCCE generously provided several scholarships in my undergraduate studies, and one scholarship award during my graduate career.

Finally, I would like to recognize my loving wife, Heather, whose patience, empathy, and understanding enabled me to confidently pursue my graduate school interests.

Contents

List of Figures

List of Tables

Definition of Symbols

$\otimes$	Convolution
$\lfloor\rfloor$	The Floor Function
$\square^*$	The Complex Conjugate Operator
α	Cyclic Frequency
$\tilde{\alpha}$	Absolute Cyclic Frequency
A_p	Preamble Boosting Amplitude
CP_{len}	Cyclic Prefix length (fractional)
$\text{cum}\{\cdot\}$	Cumulant Operator
$\delta(t)$	The Dirac Delta Function
ℓ_{cp}	Cyclic Prefix length (time)
f_s	Sampling Rate
$\text{Im}\{\cdot\}$	Imaginary Component
$\mathcal{K}$	The set of all cyclic frequencies
N	Number of sub-channels or subcarriers
N_{GH}	Number of high guard subcarriers
N_{GL}	Number of lower guard subcarriers
$\mathbb{N}$	The set of all Natural Numbers
$P[\cdot]$	Probability of some event
P_{FA}	Probability of False Alarm Detection
P_D	Probability of Detection
R_s	Symbol Rate
$\mathcal{R}_{xy}$	Cross-Correlation Function of x and y
$\mathcal{R}_x$	Autocorrelation Function of x
$\mathcal{R}_x(t_1, t_2)$	Autocorrelation Function of x evaluated at t_1, t_2
$\mathcal{R}_x(\tau)$	Autocorrelation Function of x evaluated at $t, t+\tau$
$\mathcal{R}_x(\alpha, \tau)$	Cyclic Autocorrelation Function of x evaluated at α, τ
$\text{Re}\{\cdot\}$	Real Component
$S_{f_{\tau,\rho}}(\alpha, \omega)$	Cyclic Spectrum of f
τ	Lag Time
$\tilde{\tau}$	Absolute Lag Time
t	Time
$\square^{\mathbf{T}}$	Matrix Transpose Operator
T_s	Symbol Duration
T_u	Useful Symbol Duration
W	Channel Bandwidth
X_k	Data Symbol k in a sequence $\{X_0, X_1, X_2, \cdots\}$
X_k^p	The kth Preamble Data Symbol
$\mathbb{Z}$	The set of all Integers

Definition of Acronyms

AAI	Advanced Air Interface
AAS	Adaptive Antenna System
AMC	Adaptive Modulation and Coding
ASR	Aircraft Surveillance Radar
BPSK	Binary Phase Shift Keying
CA	Cyclic Analysis
CAF	Cyclic Autocorrelation Function
CFAR	Constant False Alarm Rate
CP	Cyclic Prefix
CR	Cognitive Radio
CS	Cyclic Spectra
DFT	Discrete Fourier Transform
DL	Downlink
FCC	Federal Communications Commission
FFT	Fast Fourier Transform
FUSC	Full Use of Subcarriers
IDFT	Inverse Discrete Fourier Transform
IEEE	Institute of Electrical and Electronics Engineers
IMT-Advanced	International Mobile Telecommunications-Advanced
LAN	Local Area Network
LUT	Look-Up Table
MAN	Metropolitan Area Network
NLOS	Near Line of Sight
NPRM	Notice of Proposed Rulemaking
OFDM	Orthogonal Frequency Division Multiplexing
OFDMA	Orthogonal Frequency Division Multiple Access
OSI	Open Systems Interconnection
PA	Primary Advanced (preamble)
PAN	Personal Area Network
PN	Psuedorandom Noise
PRF	Pulse Repetition Frequency
PUSC	Partial Use of Subcarriers
QAM	Quadrature Amplitude Modulation
RTG	Receive-Transmit Transition Gap
SA	Secondary Advanced (preamble)
SM	Spatial Multiplexing
SINR	Signal to Interference Noise Ratio
SNR	Signal to Noise Ratio
STC	Space-Time Coding
TDD	Time Division Duplexing

TTG	Transmit-Receive Transition Gap
UL	Uplink
WAN	Wide Area Network
WiMAX	Worldwide Interoperability for Microwave Access
WSR	Weather Surveillance Radar

Chapter 1

Introduction

The Federal Communications Commission Notice of Proposed Rulemaking (NPRM) 12-148 proposes to make available up to 150 MHz of S-band spectrum for broadband service providers. Prior to the NPRM, the 3.5 GHz spectrum was occupied by U.S. radar systems. This wireless broadband access initiative will require broadband systems and radar systems to coexists with each other and mitigate both in-band and adjacent-channel interference. The coexistance problem between radar and consumer broadband systems is a candidate for the application of cognitive radio (CR) techniques.

One of the challenges in implementing CR techniques in this scenario is the high instantaneous-to-average power ratio used in radar systems. This implies that RF hardware must be resilient against high-energy bursts, and the CR techniques used must be robust against the wide dynamic range of the signals. A challenging part of this CR application is the development of a sensor to detect the existence of broadband systems around a radar.

The sensor is a unique challenge due to the nature of the signals involved. Radar systems typically use high-gain directional antennas coupled with high-power, low duty cycle, amplifiers to perform their mission. The directed energy from an operating radar system can impact in-band and adjacent channel broadband systems at great distances. While a typical broadband wireless cell may be measured on the order of square kilometers, the cell may be affected by a radar system 60-100 kilometers away.

Simply using a wireless broadband receiver at the radar location will not suffice for detection of broadband systems, as their link budgets are designed for much smaller distances. Instead, detection methods which are robust against low received signal energy and pulsed interference must be developed. This thesis will investigate the application of second order cyclostationary feature detection to the problem. Feature detection methods are proven to

be robust in low signal to noise ratio (SNR) environments, and can utilize significant integration gain with long observation periods. The performance of these methods against pulsed noise will be evaluated. Additionally, alternative computationally-efficient methods of feature identification and analysis of useful observation periods are performed.

1.1 Prior Work

Detection of WiMAX and other OFDM systems for cognitive radio applications is a well-researched area. A common theme among proposed detection methods is the use of second order cyclostationarity. Gardner's text provides the foundation upon which feature based detection and classification methods operate [2]. Expanding upon these concepts, statistical tests are formed for the presence of cyclostationary in [3][4].

Detection and classification of standardized OFDM waveforms such as WiMAX, LTE, DVB-T, etc. lend themselves to these second-order feature detection techniques. The parameters of these signals are known a priori because of the published standard. Thus, a detector or classifier need only examine received signals for certain signatures belonging to the signals of interest. Some detector/classifiers utilize pilot tone induced features [5]. Others examine recurring preambles [6], but the predominant features of interest are cyclic-prefix induced [7][8][9][10][11].

Describing the signal of interest in detail are several text resources [12] [13] [14] [15]. Additionally, the standards themselves provide the exact specification of the physical (PHY) layer under various operating modes of the system [1][16].

Some work has addressed the coexistence of radar and OFDM systems, typically suggesting that radar parameters change drastically to avoid interference to the communications systems [17]. However, there is little information describing how a radar system would reliably detect OFDM systems in the presence of its own signals. This thesis explores the application of these detection methods to environments which have short modulated pulses with high instantaneous to average power (typical of most radar systems).

1.2 Thesis Organization

This document is organized into four other major parts. Chapter Two gives an overview of WiMAX, the signal of interest for this document. Orthogonal Frequency Division Multiplexing (OFDM) is described in detail and an in-depth description of the physical (PHY) layer of WiMAX systems is presented. Following the introduction of OFDM and WiMAX

systems, second-order cyclostationary signal analysis is performed in Chapter Three. This cyclostationary analysis (CA) provides the foundation for signal detection methods discussed in Chapter Four. These detection methods are presented with analytical support to justify their use in additive white Gaussian noise (AWGN) environments. The detection methods are distilled into implementable algorithms for use in AWGN environments. The second part of Chapter Four introduces a pulsed interference source, and a potential solution of using CA detection metrics with a support vector machine (SVM) is presented.

Chapter Five outlines the performance metrics each detection algorithm is evaulated against and describes the AWGN and pulsed interference framework in which the simulations operate. After discussion of the simulation framework, select results are presented and discussed (with other relevant results in the Appendix). The document concludes with a sixth chapter to draw conclusions about the work and propose paths of future work.

Chapter 2

WiMAX Systems

In networking topology, there are four primary classifications of networks: Personal Area Network (PAN), Local Area Network (LAN), Metropolitan Area Network (MAN), and Wide Area Network (WAN). A PAN typically has a maximum range of several meters and is used for personal devices; common protocols of the PAN include the 802.15 family (Bluetooth, ZigBee, MiWi, etc.). Many network users are most familiar with the LAN; a LAN is generally an Ethernet or 802.11 wireless network and can range in size from an office to several buildings. The MAN extends the concepts of LAN, interconnecting the networks over a regional area and can include backbone connections over fiber and fixed microwave systems. A WAN connects geographically separated networks over a much larger area. The Internet is considered the classic example of a WAN. Cellular and wireless broadband networks such are also considered WANs (as the network connects smaller, geographically separated networks).

There are several WiMAX implementations covered by different revisions of the 802.16 standard. Some revisions are not backward compatible (e.g. 802.16e-2005 and 802.16-2004) [12]. The 802.16 working group has evolved the standard to polish the mobile user capabilities of the system starting with 802.16e-2005, and later developing 802.16-2009 and 802.16m. 802.16m incorporates an advanced air interface to meet the requirements of IMT-Advanced systems. The latest release 802.16-2012 incorporates the 802.16m amendment into the 802.16 standard (with the exception of the Advanced Air Interface which is incorporated into 802.16.1-2012)[1][16].

The WiMAX Forum is an industry organization that promotes the standardization of the hardware used in 802.16 networks. The IEEE standard only provides for the OSI Layer 1 and 2 specifications and includes many optional features. The WiMAX Forum ensures equipment interoperability and conformance to the 802.16 standard and industry-adopted standards.

WiMAX is organized into three types of stations: a base station, subscriber station, and a mobile station. Subscriber stations are used in fixed service point-to-point links (such as

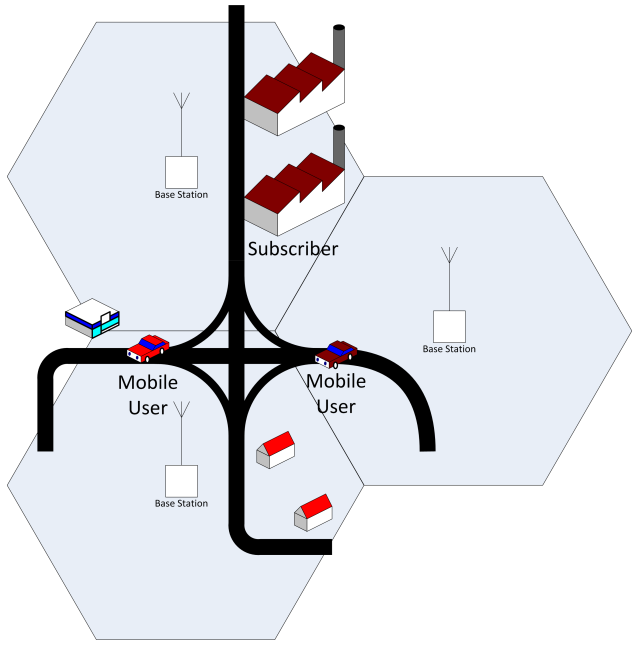

Figure 2.1: *Example Fixed and Mobile WiMAX System*

a gateway for a LAN). Mobile stations are handsets and other devices used by consumers. The latest standard 802.16-2012 incorporates the specifications of 802.16m, which provided for advanced mobile service.

2.1 OFDM

Orthogonal Frequency Division Multiplexing (OFDM) and Orthogonal Frequency Division Multiple Access (OFDMA) are modulation methods used by nearly all latest-generation wireless broadband systems. OFDMA is a special case of OFDM. OFDM is a multicarrier modulation scheme which spaces the carriers at such distances that they are all orthogonal to each other and cause no inter-carrier interference [18].

Given some channel bandwidth W divided into N uniformly distributed sub-channels, orthogonality is achieved at a symbol rate of:

$$\Delta f = \frac{W}{N} \tag{2.1}$$

$$R_s = \frac{1}{\Delta f} \tag{2.2}$$

To achieve a time domain signal which satisfies the othorgonality requirement, an Inverse Fourier Transform is applied to frequency domain symbols. This is typically implemented

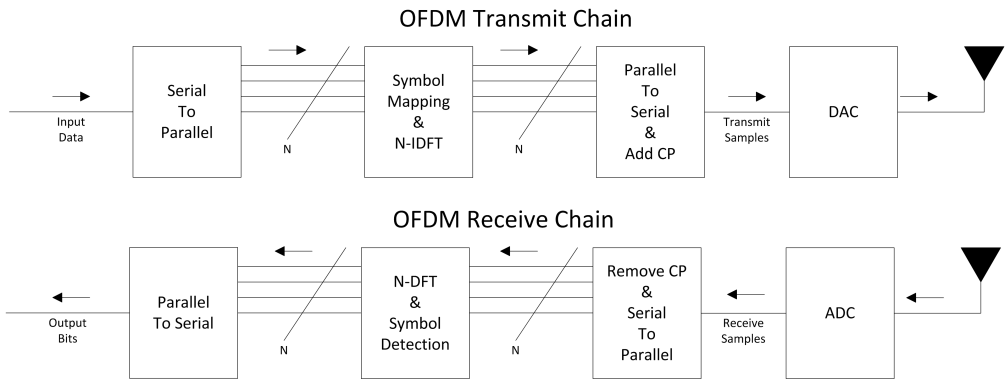

Figure 2.2: *OFDM Block Diagram*

as an Inverse Discrete Fourier Transform as real systems operate in discrete time. The IDFT is generally approximated with an Inverse Fast Fourier Transform, with data symbols populating the bins of the FFT. The FFT size corresponds to the number of subcarriers, N, in Equation (2.1). The sampling rate of the IFFT modulator, using complex samples, corresponds to the bandwidth W of the system. The symbol duration becomes $T_s = N/W$.

Demodulation of an OFDM symbol is simply the converse operation: a DFT applied to received time-domain data (typically approximated with a Fast Fourier Transform). To overcome the effects of multipath propagation effects, the cyclic prefix is introduced. The cyclic prefix is simply copying some fraction of the OFDM time-domain samples (1/4, 1/8, 1/16,etc.) from the tail of the symbol and prepending them to the beginning of the time domain symbol. This allows for a maximum delay spread of $f_s T_u \ell_{cp}$ where f_s is the sampling rate, T_u is the useful symbol duration (a function of the FFT size and oversampling rate), and ℓ_{cp} is the fractional length of the cyclic prefix. Figure 2.2 shows an example OFDM transmitter/receiver pair.

OFDM is described analytically by describing the information on each subcarrier as a generic QAM signal:

$$X_k = A_k e^{j\theta_k} \tag{2.3}$$

And the OFDM symbol is described as the sum of all subcarriers:

$$s(t) = \frac{1}{\sqrt{N}} \sum_{k=0}^{N-1} X_k e^{j2\pi kt/T_u}, 0 \leq t \leq T_u \tag{2.4}$$

To aid with channel estimation and equalization, pilot tones are used on a subset of the OFDM subcarriers. The distribution of pilot tones is governed by the anticipated channel coherence bandwidth and maximum Doppler shift anticipated. Pilot tones are typically boosted in magnitude over the data symbols and have a psuedorandom data sequences that is known a priori by the receiver. Figure 2.3 demonstrates the magnitude of the frequency domain OFDM symbol, with boosted pilot tones in red.

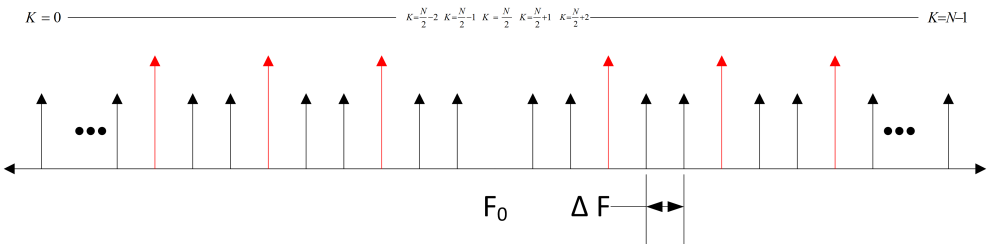

Figure 2.3: *Frequency Domain OFDM Magnitude*

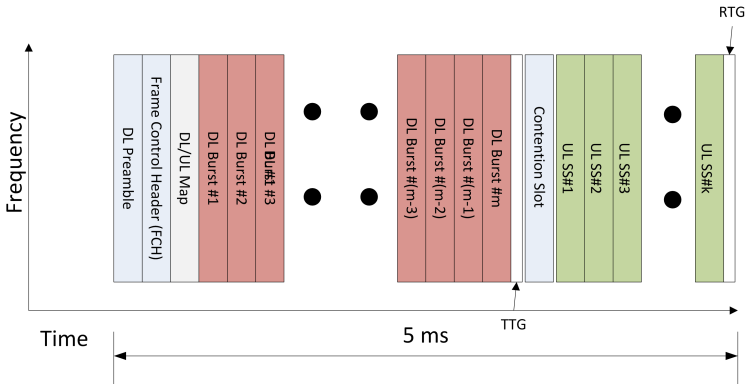

Figure 2.4: *TDD WiMAX OFDM Example*

2.2 WiMAX OFDMA PHY Layer

A multi-user OFDM system uses either Time Division Duplexing (TDD) or Frequency Division Duplexing (FDD) to provide data to different users. OFDMA allows for a more efficient allocation of time and frequency domain resources by assigning users different 'tiles' in a transmission burst as opposed to allocating complete symbols (compare Figures 2.4 and 2.5). 802.16 WirelessMAN-OFDM specifies an OFDM PHY for non-line of sight (NLOS) links. Figure 2.4 illustrates the frame structure of TDD WirelessMAN-OFDM [1, pp. 834].

The basic unit of the WiMAX frame is a single OFDM symbol. As described in the OFDM overview, each symbol contains pilot tones. The 802.16 standard specifies pilot tone modulation as BPSK encoded, with the input binary sequence following a psuedorandom binary sequence (PRBS) generator $X^{11} + X^9 + 1$ [1, pp. 826]. The seed value of the PRBS generator is determined from the *IDCell* and *Segment* properties of the base station. These pilot tones are distributed in a circular buffer over the designated pilot subcarriers. The actual pilot subcarriers vary depending on various operating parameters of the system (such as FUSC, PUSC, STC, etc.). Pilot tones are indexed on the first useable subcarrier above the lower guard band. Table 2.1 shows an example distribution of pilot subcarriers.

In addition to the defined pilot tones, each WiMAX frame has a specified preamble. The preamble is another BPSK modulated psuedorandom sequence. The modulation data orig-

Table 2.1: *Example Pilot Tone Subcarrier Distribution, N_{fft} = 1024, FUSC, non-STC [1, pp 1171]*

Subcarrier Set	Subcarrier Indicies
Variable Set 0	[0,24,48,72,96,120,144,168,192,216,240,264,288, 312,336,360,384,408,432,456,480,504,528,552,576, 600,624,648,672,696,720,744,768,792,816,840]
Constant Set 0	$72 * (2 * (k)) + 9,\ k = \{0, 1, 2, 3, 4, 5\}$
Variable Set 1	[12,36,60,84,108,132,156,180,204,228,252,276,300, 324,348,372,396,420,444,468,492,516,540,564,588,612, 636,660,684,708,732,756,780,804,828]
Constant Set 1	$72 * (2 * (k) + 1) + 9,\ k = \{0, 1, 2, 3, 4\}$

Table 2.2: *WiMAX OFDMA Preamble Subcarrier Distribution*

FFT Size	Parameter k
2048	$\{0, \ldots, 567\}$
1024	$\{0, \ldots, 283\}$
512	$\{0, \ldots, 142\}$
128	$\{0, \ldots, 35\}$

inates from lookup tables corresponding to the *IDCell* and *Segment* properties of the base station [1, pp. 1143-1161]. The allocated preamble subcarriers for WirelessMAN-OFDMA are described with Equation (2.5) and k defined in Table 2.2.

$$PreambleCarrierSet_n = n + 3K \tag{2.5}$$

Every third subcarrier is populated in the preamble, which results in a time-domain repetition of three preamble symbols within the useful symbol duration. Both the pilot tones and preamble subcarriers are boosted over unit-energy according to their system parameters as shown in Table 2.3.

Expanding on WirelessMAN-OFDM, WirelessMAN-OFDMA provides for a multi-user system with a more flexible framework to distribute bandwidth. The legacy TDD OFDMA air interface uses a frame size of 5ms with the uplink (UL) and downlink (DL) times specified as an UL/DL ratio (similar to WirelessMAN-OFDM). There are pauses between the UL and DL bursts known as the transmit to receive transition gap (TTG) and receive to transmit transition gap (RTG). The frame preamble, header (DL/UL map), DL burst, TTG, UL burst, and RTG form the entire 5ms frame as shown in Figure 2.5[1, pp. 897].

An "advanced air interface" (AAI) builds upon the legacy OFDMA frames, incorporating four legacy frames into a superframe as shown in Figure 2.6. The AAI was designed to meet the specifications of IMT-Advanced systems. Within the superframe are three advanced preambles: two secondary advanced (SA) preambles and one primary advanced (PA) pream-

Table 2.3: *WiMAX Subcarrier Boosting Parameters [1, pp. 1293]*

Subcarrier Type	Boosting Level	Notes
Pilot	2.5dB	All Except UL PUSC, DL TUSC1, DL/UL STC
Pilot	5.5dB	DL STC, UL AMC, Collaborative SM
Pilot	3dB	UL STC & PUSC
Pilot	0dB	All Others
Preamble	9dB	DL (non-AAS)
Preamble	0dB	UL & DL AAS

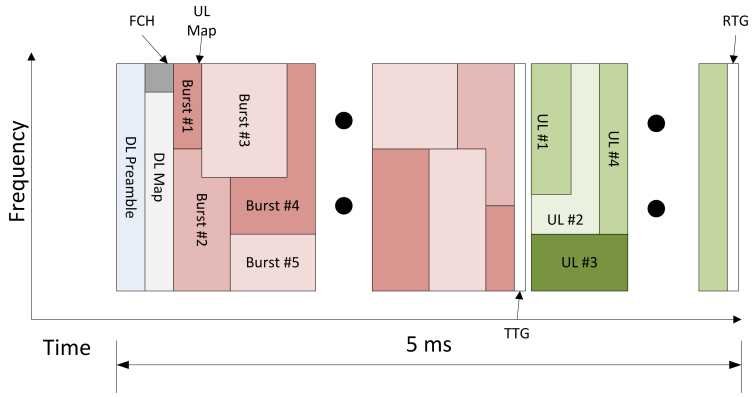

Figure 2.5: *TDD WiMAX OFDMA Example*

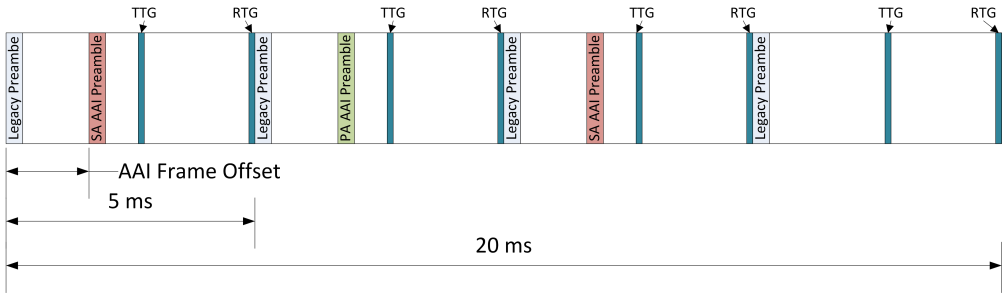

Figure 2.6: *Overview of TDD WiMAX AAI Superframe Structure*

ble. When interoperating with legacy systems, these preambles are offset from the start of the AAI superframe with a delay called the Frame Offset[12][19]. The symbols following the PA and SA preambles contain detailed information for the AAI resource allocations for both the DL and UL. Figure 2.6 describes the sequence of preambles in the 20ms AAI superframe [16, pp. 580].

Both PA and SA preambles are specified in a manner similar to the legacy preamble. In an SA preamble symbol the subcarriers are allocated similar to the legacy preamble (every third subcarrier), which results in a three-fold time domain repetition for synchronization purposes. These features allow user equipment to uniquely identify several base stations as the equipment connects to a network and performs periodic re-evaluations of its connection. The AAI can be configured to be backward-compatible with legacy OFDMA systems, allocating frame symbols for both a legacy DL/UL map and an AAI DL/UL map [12]. The legacy and AAI both have different pilot tone distributions available, with the AAI capable of adapting pilot distribution on a per-burst basis.

Chapter 3

Second-Order Cyclostationary Signal Analysis

A process is described as wide-sense stationary if the mean and autocorrelation function have no dependence on time. That is, the autocorrelation function can be described completely as a function of a time lag τ:

$$\mathcal{R}_s(t_1, t_2) = \mathcal{R}_s(t, t+\tau), \qquad \tau = t_2 - t_1 \quad \forall t \tag{3.1}$$

A process is second-order cyclostationary if the mean and autocorrelation function are periodic[2]. The autocorrelation function can be written as a sum over the set $\mathcal{K}$ of all cyclic frequencies α of the signal :

$$\mathcal{R}_s(t, t+\tau) = \sum_{\alpha \exists \mathcal{K}} \mathcal{R}_s(\alpha, \tau) e^{\jmath 2\pi\alpha t} \tag{3.2}$$

Where $\mathcal{R}_s(\alpha, \tau)$ is the cyclic autocorrelation function (CAF) of $s(t)$ at cyclic frequency (CF) α and time lag τ as defined by [2]:

$$\mathcal{R}_s(\alpha, \tau) \triangleq \lim_{I \to \infty} \frac{1}{I} \int_{-I/2}^{I/2} \mathcal{R}_s(t, t+\tau) e^{-\jmath 2\pi\alpha t} \tag{3.3}$$

The ideal CAF estimate from a finite length sampled signal of M samples $\{s(n)\}_{n=0}^{M-1}$ is of the form [3]:

$$\hat{\mathcal{R}}_s(\alpha, \tau) = \frac{1}{M} \sum_{n=0}^{M-\tau-1} s(n) s^*(n+\tau) e^{\jmath 2\pi\alpha n} \tag{3.4}$$

The estimate $\hat{\mathcal{R}}_s$ is related to $\mathcal{R}_s(\alpha, \tau)$ with an error value ϵ. As M approaches infinity, ϵ approaches zero [3].

$$\hat{\mathcal{R}}_s(\alpha, \tau) = \mathcal{R}_s(\alpha, \tau) + \epsilon_s(\alpha, \tau) \tag{3.5}$$

One can observe that (α, τ) in Equation (3.4) is dependent upon the sampling frequency f_s of a discrete signal, and thus not equivalent to the same parameters in Equation (3.3). To describe the relationship between the parameters in Equations (3.3) and (3.4), it is common to use the notation $(\tilde{\alpha}, \tilde{\tau})$ to describe the absolute cyclic frequency and time lag. Therefore, the following relationship is defined, and Equation (3.3) re-defined:

$$(\alpha, \tau) = (\tilde{\alpha} f_s^{-1}, \tilde{\tau} f_s) \tag{3.6}$$

$$\mathcal{R}_s(\tilde{\alpha}, \tilde{\tau}) = \lim_{I \to \infty} \frac{1}{I} \int_{-I/2}^{I/2} \mathcal{R}_s(t, t + \tilde{\tau}) e^{-\jmath 2\pi \tilde{\alpha} t} \tag{3.7}$$

3.1 Cyclic Analysis of WiMAX Signals

3.1.1 OFDM CAF

In Chapter 2, a continuous time representation of an OFDM symbol was defined as:

$$s(t) = \frac{1}{\sqrt{N}} \sum_{k=0}^{N-1} X_k e^{\jmath 2\pi k t / T_u}, \qquad 0 \leq t \leq T_u \tag{3.8}$$

In real systems, the OFDM symbol is prefixed with a portion of the tail of the symbol. This is the Cyclic Prefix (CP). A discrete time (sampled) definition of an OFDM symbol takes the form:

$$s(t) = \begin{cases} \sum_{n=0}^{N-1} \left[\delta\left(t - n\frac{T_u}{N}\right) \frac{1}{\sqrt{N}} \sum_{k=0}^{N-1} X_k e^{\jmath 2\pi k t / T_u} \right] & 0 \leq t \leq T_u \\ 0 & \text{otherwise} \end{cases} \tag{3.9}$$

Defining the CP length as a fraction of the useful symbol time T_u, the sampled CP is described as:

$$0 \leq CP_{len} \leq 1, \qquad CP_{len} \cdot N \;\; \exists \;\; \mathbb{N} \tag{3.10}$$

$$\ell_{cp} = CP_{len} \cdot T_u \tag{3.11}$$

$$CP_{CP_{len}}(t) = \begin{cases} \sum_{n=0}^{CP_{len}N-1} \left[\delta\left(t - n\frac{T_u}{N}\right) \frac{1}{\sqrt{N}} \sum_{k=0}^{N-1} X_k e^{\jmath 2\pi k (t + T_u - \ell_{cp}) / T_u} \right] & 0 \leq t < \ell_{cp} \\ 0 & \text{otherwise} \end{cases} \tag{3.12}$$

Then the complete transmitted symbol becomes:

$$m(t) = CP_{CP_{len}}(t) + s(t - \ell_{cp}) \tag{3.13}$$

Evaluating the CAF Estimate:

$$\hat{\mathcal{R}}_m(\alpha,\tau) = \frac{1}{M}\sum_{n=0}^{M-\tau-1} m(n)m^*(n+\tau)e^{\jmath 2\pi\alpha n} \tag{3.14}$$

$$= \frac{1}{M}\sum_{n=0}^{M-\tau-1}\left[CP_{CP_{len}}\left(n\frac{T_u}{N}\right)+s\left(n\frac{T_u}{N}-\ell_{cp}\right)\right]\left[CP_{CP_{len}}\left((n+\tau)\frac{T_u}{N}\right)\right.$$
$$\left.+s\left((n+\tau)\frac{T_u}{N}-\ell_{cp}\right)\right]^* e^{\jmath 2\pi\alpha n} \tag{3.15}$$

$$= \frac{1}{M}\sum_{n=0}^{M-\tau-1}\left[CP_{CP_{len}}\left(n\frac{T_u}{N}\right)CP^*_{CP_{len}}\left((n+\tau)\frac{T_u}{N}\right)\right.$$
$$+s\left(n\frac{T_u}{N}-\ell_{cp}\right)s^*\left((n+\tau)\frac{T_u}{N}-\ell_{cp}\right)$$
$$+CP_{CP_{len}}\left(n\frac{T_u}{N}\right)s^*\left((n+\tau)\frac{T_u}{N}-\ell_{cp}\right)$$
$$\left.+s\left(n\frac{T_u}{N}-\ell_{cp}\right)CP^*_{CP_{len}}\left((n+\tau)\frac{T_u}{N}\right)\right]e^{\jmath 2\pi\alpha n} \tag{3.16}$$

Now examine the four parts of Equation (3.16) separately. First, consider for any $M \geq N(1+CP_{len})$:

$$\frac{1}{M}\sum_{n=0}^{M-\tau-1} CP_{CP_{len}}\left(n\frac{T_u}{N}\right)CP^*_{CP_{len}}\left((n+\tau)\frac{T_u}{N}\right)e^{\jmath 2\pi\alpha n} \tag{3.17}$$

From the definition of $CP_{CP_{len}}(t)$ in Equation (3.12) we observe the following results:

$$\tau \neq 0 \longrightarrow 0 \tag{3.18}$$

$$\tau = 0 \longrightarrow \frac{1}{M}\sum_{sym=0}^{\left\lfloor\frac{M}{(1+CP_{len})N}\right\rfloor-1}\left[\sum_{n=sym(1+CP_{len})N}^{sym(1+CP_{len})N+CP_{len}N-1}\left|CP^{sym}_{CP_{len}}\left(n\frac{T_u}{N}\right)\right|^2 e^{\jmath 2\pi\alpha n}\right] \tag{3.19}$$

Similarly for

$$\frac{1}{M}\sum_{n=0}^{M-\tau-1} s\left(n\frac{T_u}{N}-\ell_{cp}\right)s^*\left((n+\tau)\frac{T_u}{N}-\ell_{cp}\right)e^{\jmath 2\pi\alpha n} \tag{3.20}$$

The definition of $s(t)$ in Equation (3.9) yields:

$$\tau \neq 0 \longrightarrow 0 \tag{3.21}$$

$$\tau = 0 \longrightarrow \frac{1}{M}\sum_{sym=0}^{\left\lfloor\frac{M}{(1+CP_{len})N}\right\rfloor-1}\left[\sum_{n=CP_{len}N+sym(1+CP_{len})N}^{sym(1+CP_{len})N-1}\left|s^{sym}\left(n\frac{T_u}{N}-\ell_{cp}\right)\right|^2 e^{\jmath 2\pi\alpha n}\right] \tag{3.22}$$

Because the data X_k is I.I.D. uniformly distributed random data, both Equations (3.19) and (3.22) result in a CAF response only at $\alpha = 0$; the summation of the two is an autocorrelation of the complete observed signal with itself at $\tau = 0$, thus having constant mean and $\mathcal{R}_m$ independent of t.

$$\hat{\mathcal{R}}_m(\alpha, \tau = 0) = \frac{1}{M} \sum_{n=0}^{M-1} \left| m\left(n\frac{T_u}{N}\right)\right|^2 e^{\jmath 2\pi\alpha n} \tag{3.23}$$

$$\hat{\mathcal{R}}_m(\alpha, \tau = 0) = \frac{1}{M} \sum_{n=0}^{M-1} \left| m\left(n\frac{T_u}{N}\right)\right|^2 \delta(\alpha) \tag{3.24}$$

Realizing that $\mathcal{R}_{xy}(t,\tau) = \mathcal{R}_{yx}(t,-\tau)$ only one remaining combination need be evaluated.

$$\frac{1}{M} \sum_{n=0}^{M-\tau-1} CP_{CP_{len}}\left(n\frac{T_u}{N}\right) s^*\left((n+\tau)\frac{T_u}{N} - \ell_{cp}\right) e^{\jmath 2\pi\alpha n} \tag{3.25}$$

$$\tau \neq T_u f_s \longrightarrow 0 \tag{3.26}$$

$$\tau = \pm T_u f_s \longrightarrow \frac{1}{M} \sum_{sym=0}^{\left\lfloor \frac{M - T_u f_s}{(1+CP_{len})N} \right\rfloor - 1} \left[\sum_{n=sym(1+CP_{len})N}^{sym(1+CP_{len})N + CP_{len}N - 1} \left| CP^{sym}_{CP_{len}}\left(n\frac{T_u}{N}\right)\right|^2 e^{\jmath 2\pi\alpha n} \right] \tag{3.27}$$

Because of the nozero lag $\tau = \pm T_u f_s$, this implies a periodic structure (and nonzero CAF at $\alpha \neq 0$). $\mathcal{R}_m$ has a time dependence. If an infinite sampling of OFDM symbols are considered, then the CAF has the form:

$$\hat{\mathcal{R}}_m(\alpha, \tau = \pm T_u f_s) = A \cdot sinc\left(\frac{\alpha}{CP_{len}N}\right) \sum_{k=-\infty}^{\infty} \delta\left(\alpha - \frac{k}{(1+CP_{len})N}\right) \tag{3.28}$$

Where A is the magnitude of the CAF response at $(\alpha, \tau) = (0, 0)$. Because the observed sample sequence is finite, the above impulse train is convolved with another sinc function corresponding to the entire observation window:

$$\hat{\mathcal{R}}_m(\alpha, \tau = \pm T_u f_s) = \left[A \cdot sinc\left(\frac{\alpha}{CP_{len}N}\right) \sum_{k=-\infty}^{\infty} \delta\left(\alpha - \frac{k}{(1+CP_{len})N}\right)\right] \otimes sinc\left(\frac{1}{M}\right) \tag{3.29}$$

Therefore, one can see as M becomes large, $\hat{\mathcal{R}}_m(\alpha, \tau = \pm T_u f_s)$ approaches (3.28). The resulting CAF with nonzero magnitude at the lags and frequencies indicated in Table 3.1. Figure 3.1 illustrates the CAF at $\tilde{\tau} = 0$ of a sequence of 300 OFDMA symbols, and Figure 3.2 shows the CAF response at $\tilde{\tau} = T_u$.

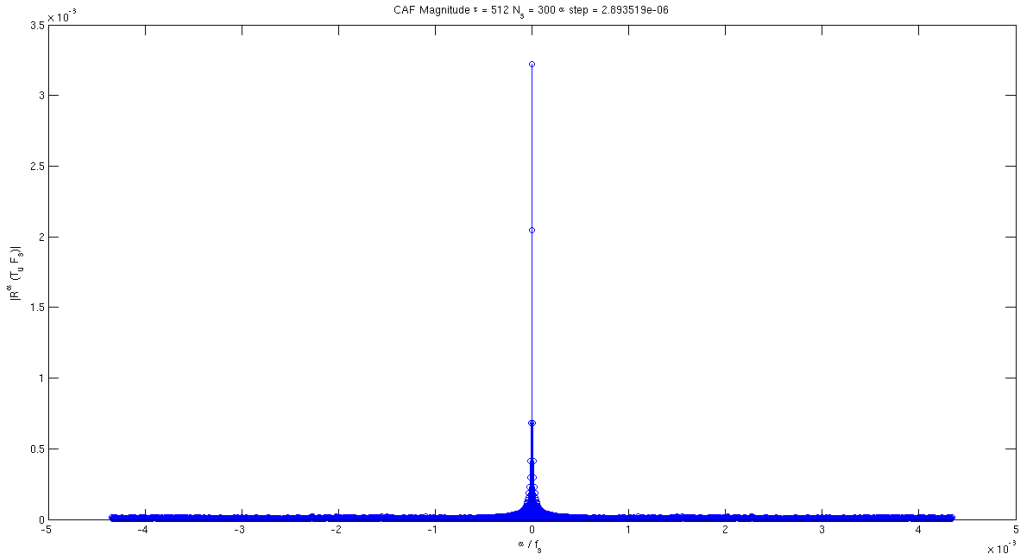

Figure 3.1: $CAF\ N_{sym} = 300\ \tilde{\tau} = 0\ N = 512\ CP_{len} = 1/8$

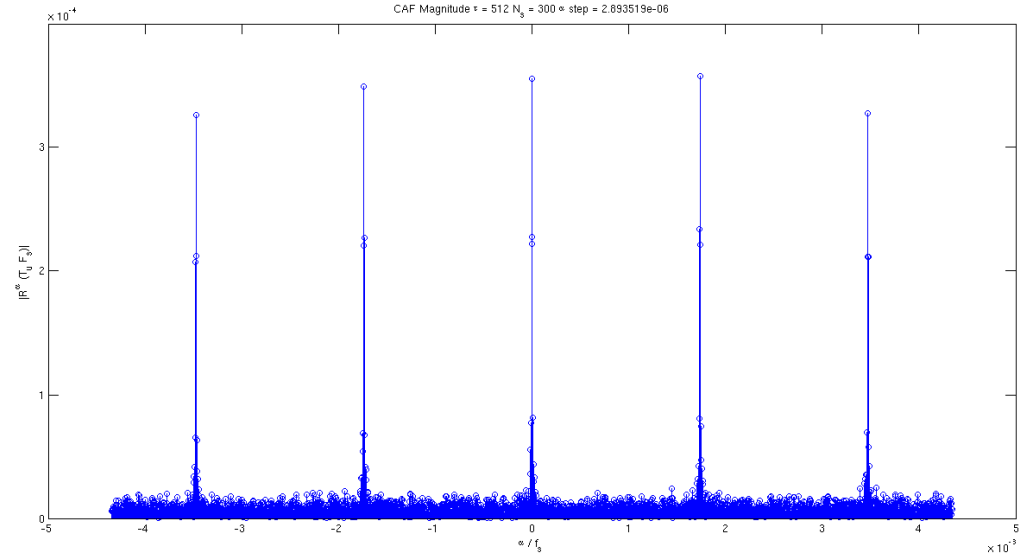

Figure 3.2: $CAF\ N_{sym} = 300\ \tilde{\tau} = T_u\ N = 512\ CP_{len} = 1/8$

Table 3.1: *OFDM Symbol CAF Results*

$\tilde{\alpha}$	$\tilde{\tau}$	Feature Description
0	0	The autocorrelation of the signal with itself
$\frac{k}{T_s}, k \exists \mathbb{Z}$	$\pm T_u$	CP induced cyclostationarity

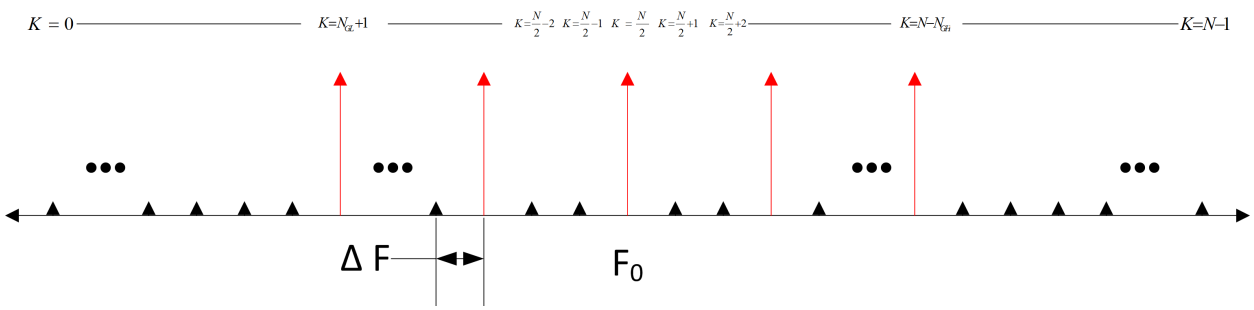

Figure 3.3: *Example Distribution of Preamble Tones*

3.1.2 WiMAX OFDMA Frame CA

The previous section showed the CAF estimate for a sequence of OFDM symbols. In addition to the CP induced cyclostationarity, a WiMAX frame contains a preamble symbol every $5ms$. The 802.16 standard specifies in §8.4.6.1.1 the subcarrier allocation shown in Equation (3.30). Where n is the *SegmentID* of the base station and k is one of the sets specified by Table 3.2. Figure 3.3 provides a graphical representation of the preamble subcarrier distribution.

$$PreambleCarrierSet_n = n + 3K \tag{3.30}$$

The preamble subcarriers are offset where the 0th subcarrier is the first useable subcarrier in the OFDM symbol. The first useable subcarrier is the first index above the lower guard band. X_k^p is the kth preamble data bit from the tables specified in §8.4.6.1.1 mapped such

Table 3.2: *WiMAX OFDMA Preamble Subcarrier Distribution*

FFT Size	Parameter k
2048	$\{0, \ldots, 567\}$
1024	$\{0, \ldots, 283\}$
512	$\{0, \ldots, 142\}$
128	$\{0, \ldots, 35\}$

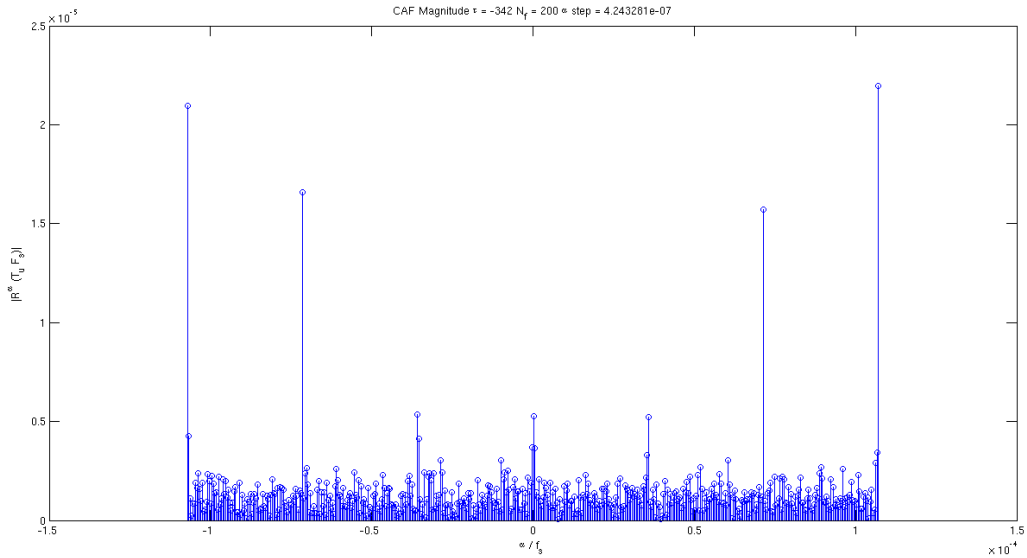

Figure 3.4: *CAF* $N_{frame} = 200$ $\tilde{\tau} = -2T_u/3$ $N = 512$ $CP_{len} = 1/8$

that $X_k^p \exists \{-1, 1\}$ and A_p is the specified preamble boosting level:

$$X_k = \begin{cases} 0 & k \leq N_{GL} \\ 0 & k \geq N - N_{GH} + 1 \\ 0 & (k - N_{GL} - n)\, mod(3) \neq 0 \\ A_p X^p_{\left\lfloor \frac{K - N_{GL} - n}{3} \right\rfloor} & (k - N_{GL} - n)\, mod(3) = 0 \end{cases} \tag{3.31}$$

This distribution of subcarriers results in a nonzero CAF at[11]:

$$(\tilde{\alpha}, \tilde{\tau}) = \left(\frac{i}{T_f}, \frac{nT_u}{3} \right) \qquad i = \{0, \pm 1, \pm 2 \ldots\}$$

$$n = \{0, \pm 1, \pm 2\} \tag{3.32}$$

$$(\tilde{\alpha}, \tilde{\tau}) = \left(\frac{i}{T_f}, nT_f \right) \qquad i = \{0, \pm 1, \pm 2, \ldots\}$$

$$n = \{0, \pm 1, \pm 2, \ldots\} \tag{3.33}$$

The lag $\tilde{\tau} = \frac{nT_u}{3}$ is caused by the time-domain repetition of the preamble symbol. Due to populating every third IFFT bin, the preamble symbol repeats three times over the course of one useful symbol period T_u. Figures 3.4,3.5, and 3.6 demonstrate the CAF response due to the preamble symbol over an observation of 200 frames.

Because the preamble is unchanging $\tilde{\tau} = nT_f$ is also a nonzero lag. CFs $\tilde{\alpha} = \frac{i}{T_u}$ are noted at each specified lag. These CFs are induced because of similar structure to the CP induced

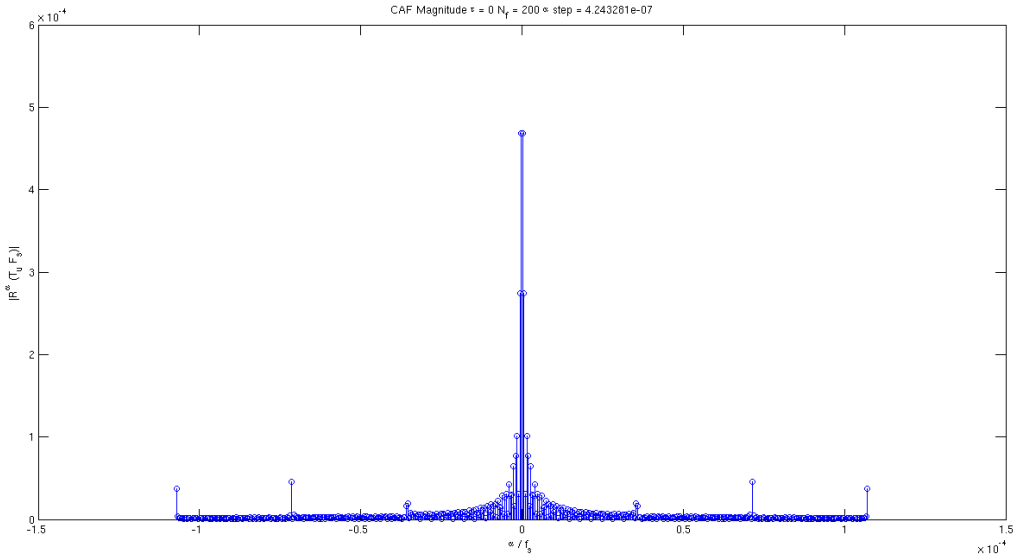

Figure 3.5: *CAF* $N_{frame} = 200$ $\tilde{\tau} = 0$ $N = 512$ $CP_{len} = 1/8$

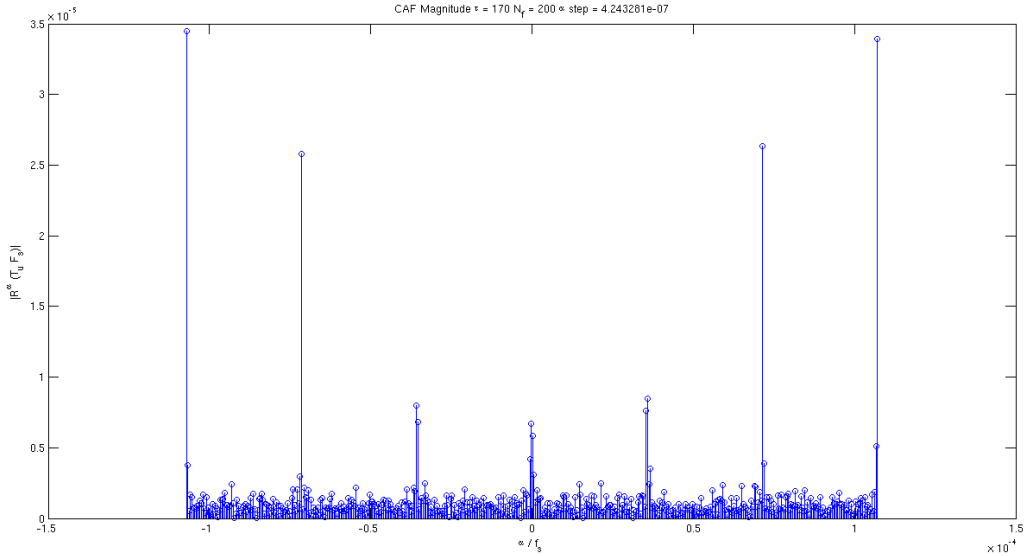

Figure 3.6: *CAF* $N_{frame} = 200$ $\tilde{\tau} = T_u/3$ $N = 512$ $CP_{len} = 1/8$

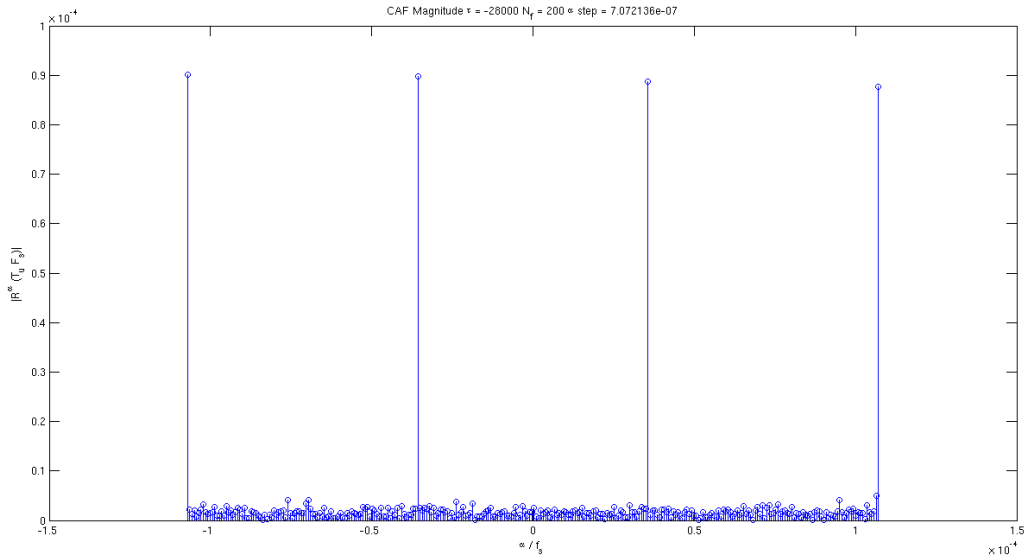

Figure 3.7: *CAF* $N_{frame} = 200$ $\tilde{\tau} = -T_f$ $N = 512$ $CP_{len} = 1/8$

CFs from Equation 3.28. The resulting analysis of the CAF structure from a sequence of WiMAX frames yields nonzero results at the CFs and lags shown in Table 3.3. Figures 3.7 and 3.8 demonstrate these nonzero CAF responses.

Table 3.3: *WiMAX OFDMA Frame CAF Results*

$\tilde{\alpha}$	$\tilde{\tau}$	Feature Description
0	0	The autocorrelation of the signal with itself
$\frac{i}{T_f}, i\exists\mathbb{Z}$	$\frac{nT_u}{3}, n\exists\{0, \pm1, \pm2\}$	Every third subcarrier populated in the preamble symbol
$\frac{i}{T_f}, i\exists\mathbb{Z}$	$nT_f, n\exists\mathbb{Z}$	The preamble symbol recurs every T_f

Considering a WiMAX frame has irregular gaps between the DL and UL block (TTG and RTG, respectively), the CP-induced cyclostationarity $(\tilde{\alpha}, \tilde{\tau}) = (\frac{k}{T_s}, \pm T_u), k\exists\mathbb{Z}$ is convolved with the fourier series representation of two rectangular waves, both with period T_f and with duty cycles $\frac{N_{DL}T_s}{T_f}$ and $\frac{N_{UL}T_s}{T_f}$ for the DL and UL blocks respectively. Furthermore, the TTG and RTG may vary from frame to frame leading to the only predictable CP-induced CAF response at $(\tilde{\alpha}, \tilde{\tau}) = (0, \pm T_u)$.

3.1.3 Summary

In this chapter, the second-order cyclic features of OFDM symbols and the WiMAX signal were discussed. OFDM exhibits a nonzero CAF response due to the cyclic prefix. Because WiMAX frames are a sequence of OFDM symbols, they share this same feature. WiMAX also

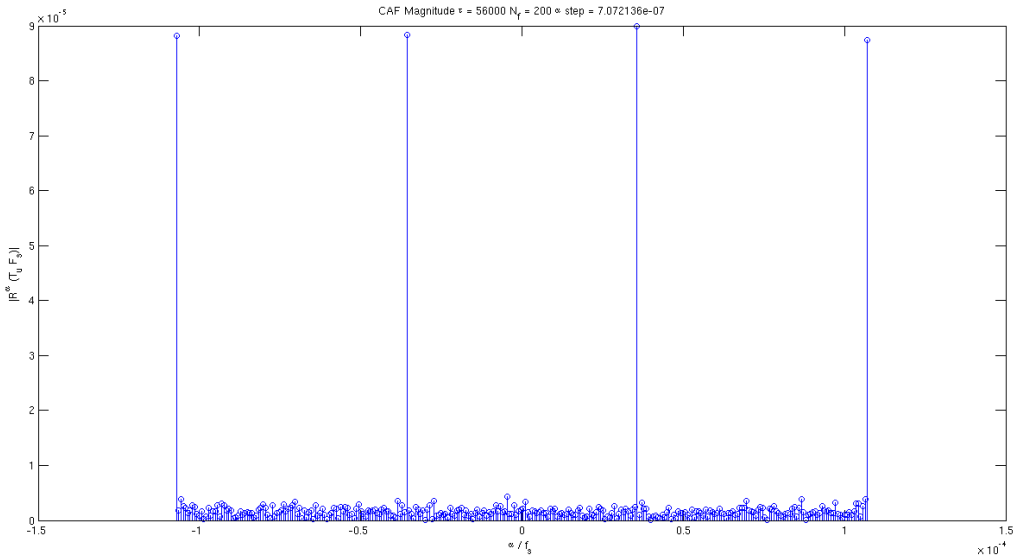

Figure 3.8: *CAF* $N_{frame} = 200$ $\tilde{\tau} = 2T_f$ $N = 512$ $CP_{len} = 1/8$

introduces nonzero CAF response because of the frame preamble structure (which repeats every 5ms frame). Tables 3.1 and 3.3 summarize the CAF responses of interest.

Chapter 4

Signal Detection and Identification

Cyclic features are used for detection, identification, and classification [2]. In this chapter, the application of cyclostationary analysis to the detection of WiMAX is discussed. A statistical test for the detection of cyclic frequencies is presented first[3], followed by a method for detection of multiple CFs[4]. Both tests require the computation of a covariance matrix. A third method which simplifies the test statistic does not require calculation of a covariance matrix[7]. After discussion of the three detection methods, a support vector machine binary classifier is suggested.

4.1 Theoretical Analysis

4.1.1 Statistical Test for Presence of Cyclostationarity

Assuming the samples of the process s well separated in time are independent, the CAF estimate in Equation (4.1) converges upon the true CAF as M becomes large[3].

$$\hat{\mathcal{R}}_s(\alpha,\tau) = \frac{1}{M}\sum_{n=0}^{M-\tau-1} s(n)s^*(n+\tau)e^{j2\pi\alpha n} \tag{4.1}$$

$$\hat{\mathcal{R}}_s(\alpha,\tau) = \mathcal{R}_s(\alpha,\tau) + \epsilon_s(\alpha,\tau) \tag{4.2}$$

$$\lim_{M\to\infty} \hat{\mathcal{R}}_s(\alpha,\tau) = \mathcal{R}_s(\alpha,\tau) \tag{4.3}$$

The error quantity $\sqrt{M}\left[\hat{\mathcal{R}}_s(\alpha,\tau) - \mathcal{R}_s(\alpha,\tau)\right]$ is asymptotically complex normal

$$\lim_{M\to\infty} \sqrt{M}\epsilon_s(\alpha,\tau) \Rightarrow \mathcal{N}(0,\Sigma) \tag{4.4}$$

Where Σ is the covariance matrix

$$\Sigma = \begin{bmatrix} \mathrm{Re}\left\{\frac{Q+Q^*}{2}\right\} & \mathrm{Im}\left\{\frac{Q-Q^*}{2}\right\} \\ \mathrm{Im}\left\{\frac{Q+Q^*}{2}\right\} & \mathrm{Re}\left\{\frac{Q^*-Q}{2}\right\} \end{bmatrix} \tag{4.5}$$

Where

$$Q(m,n) \triangleq S_{f_{\tau_m,\tau_n}}(2\alpha,\alpha) \tag{4.6}$$

$$Q^*(m,n) \triangleq S^*_{f_{\tau_m,\tau_n}}(0,-\alpha) \tag{4.7}$$

$$S_{f_{\tau,\rho}}(\alpha,\omega) \triangleq \lim_{M\to\infty} \frac{1}{M} \sum_{t=0}^{M-1} \sum_{\xi=-\infty}^{\infty} \mathrm{cum}\{\mathcal{R}_s(t,\tau), \mathcal{R}_s(t+\xi,\rho)\} e^{-\jmath\omega\xi} e^{-\jmath\alpha t} \tag{4.8}$$

$$S^*_{f_{\tau,\rho}}(\alpha,\omega) \triangleq \lim_{M\to\infty} \frac{1}{M} \sum_{t=0}^{M-1} \sum_{\xi=-\infty}^{\infty} \mathrm{cum}\{\mathcal{R}_s(t,\tau), \mathcal{R}^*_s(t+\xi,\rho)\} e^{-\jmath\omega\xi} e^{-\jmath\alpha t} \tag{4.9}$$

The parameters of the covariance matrix Σ are estimated with the frequency smoothed cyclic periodigram[3][11][4].

$$Q(m,n) = \hat{S}_{f_{\tau_m,\tau_n}}(2\alpha,\alpha) = \frac{1}{ML} \sum_{s=\frac{-(L-1)}{2}}^{\frac{(L-1)}{2}} W(s) F_{M,\tau_n}\left(\alpha - \frac{2\pi s}{M}\right) F_{M,\tau_m}\left(\alpha + \frac{2\pi s}{M}\right) \tag{4.10}$$

$$Q^*(m,n) = \hat{S}^*_{f_{\tau_m,\tau_n}}(0,-\alpha) = \frac{1}{ML} \sum_{s=\frac{-(L-1)}{2}}^{\frac{(L-1)}{2}} W(s) F^*_{M,\tau_n}\left(\alpha + \frac{2\pi s}{M}\right) F_{M,\tau_m}\left(\alpha + \frac{2\pi s}{M}\right) \tag{4.11}$$

Where $W(s)$ is a spectral window function with length L and

$$F_{T,\tau}(\omega) = \sum_{t=0}^{T-1} x(t) x^*(t+\tau) e^{-\jmath\omega t} \tag{4.12}$$

To determine the presence of a cyclic frequency, create a hypothesis test:

$$\begin{aligned} \mathbb{H}_0 : \alpha \quad & \nexists \mathcal{K} \quad \forall \quad \{\tau_n\}_{n=1}^N \Rightarrow \qquad \hat{\mathcal{R}}_s(\alpha,\tau) = \epsilon_s(\alpha,\tau) \\ \mathbb{H}_1 : \alpha \quad & \exists \mathcal{K} \quad \text{for some} \{\tau_n\}_{n=1}^N \Rightarrow \hat{\mathcal{R}}_s(\alpha,\tau) = \mathcal{R}_s(\alpha,\tau) + \epsilon_s(\alpha,\tau) \end{aligned}$$

Creating a generalized likelihood ratio test statistic Ψ[3][4]:

$$\hat{\mathbf{r}} \triangleq \left[\mathrm{Re}\left\{\hat{\mathcal{R}}_s(\alpha,\tau_1),\ldots,\hat{\mathcal{R}}_s(\alpha,\tau_n)\right\}, \mathrm{Im}\left\{\hat{\mathcal{R}}_s(\alpha,\tau_1),\ldots,\hat{\mathcal{R}}_s(\alpha,\tau_n)\right\}\right] \tag{4.13}$$

$$\Psi \triangleq M\hat{\mathbf{r}}\hat{\Sigma}^{-1}\hat{\mathbf{r}}^{\mathbf{T}} \tag{4.14}$$

Where $\mathbf{r}$ is a $1 \times 2N$ row vector and N is the number of lags considered for CF α. The residual ϵ under $\mathbb{H}_1$ converges on a normal distribution as previously noted[3][4]:

$$\mathbb{H}_1 : \lim_{M\to\infty} \sqrt{M}\left(\hat{\mathbf{r}}\hat{\Sigma}^{-1}\hat{\mathbf{r}}^{\mathbf{T}} - \mathbf{r}\Sigma^{-1}\mathbf{r}^{\mathbf{T}}\right) \Rightarrow \mathcal{N}\left(0, 4\mathbf{r}\Sigma^{-1}\mathbf{r}^{\mathbf{T}}\right) \tag{4.15}$$

The behavior of Ψ under the two hypotheses is:

$$\mathbb{H}_0 : \lim_{M\to\infty} \Psi \Rightarrow \chi^2_{2N} \tag{4.16}$$

$$\mathbb{H}_1 : \lim_{M\to\infty} \Psi \Rightarrow \mathcal{N}\left(\mathbf{r}\Sigma^{-1}\mathbf{r}^{\mathbf{T}}, 4\mathbf{r}\Sigma^{-1}\mathbf{r}^{\mathbf{T}}\right) \tag{4.17}$$

Under $\mathbb{H}_0$ a constant false alarm rate (CFAR) threshold Γ is set by evaluating the resulting chi-squared distribution with $2N$ degrees of freedom.

$$P_{FA} \triangleq P\left[\Psi \geq \Gamma | \mathbb{H}_0\right] \tag{4.18}$$

The probability of detection is approximated by substituting the estimates $\hat{\mathbf{r}}$ and $\hat{\Sigma}$ into the result from (4.17):

$$P_D \triangleq P\left[\Psi \geq \Gamma | \mathbb{H}_1\right] \tag{4.19}$$

$$P_D \approx \frac{1}{2} - \operatorname{erf}\left(\frac{\Gamma - \hat{\mathbf{r}}\hat{\Sigma}^{-1}\hat{\mathbf{r}}^{\mathbf{T}}}{\sqrt{2 \cdot 4\hat{\mathbf{r}}\hat{\Sigma}^{-1}\hat{\mathbf{r}}^{\mathbf{T}}}}\right) \tag{4.20}$$

4.1.2 Multiple CF Test

Expanding upon the previous test for a single cyclic frequency, a test can be constructed to detect a process which contains several cyclic frequencies. Considering the same test statistic Ψ from Equation (4.14) one can derive two test combined test statistics[4]:

$$\mathcal{D}_m = \underset{\alpha\exists\mathcal{K}}{\operatorname{argmax}}\Psi = \underset{\alpha\exists\mathcal{K}}{M}\hat{\mathbf{r}}\hat{\Sigma}^{-1}\hat{\mathbf{r}}^{\mathbf{T}} \tag{4.21}$$

$$\mathcal{D}_s = \sum_{\alpha\exists\mathcal{K}} \Psi = M \sum_{\alpha\exists\mathcal{K}} \hat{\mathbf{r}}\hat{\Sigma}^{-1}\hat{\mathbf{r}}^{\mathbf{T}} \tag{4.22}$$

The decision statistic $\mathcal{D}_s$ is the most interesting, as it converges on a chi-squared distribution with $2NN_\alpha$ degrees of freedom where N is the number of time lags for a certain cyclic frequency and N_α is the number of cyclic frequencies considered[4]. The hypothesis test is constructed similar to that of a single CF:

$$\mathbb{H}_0 : \alpha \quad \nexists\mathcal{K} \quad \forall \quad \{\tau_n\}_{n=1}^N \Rightarrow \qquad \hat{\mathcal{R}}_s(\alpha,\tau) = \epsilon_s(\alpha,\tau)$$

$$\mathbb{H}_1 : \alpha \quad \exists\mathcal{K} \quad \text{for some}\{\tau_n\}_{n=1}^N \Rightarrow \hat{\mathcal{R}}_s(\alpha,\tau) = \mathcal{R}_s(\alpha,\tau) + \epsilon_s(\alpha,\tau)$$

$\mathbb{H}_0$ is rejected if $\mathcal{D}_s \geq \Gamma$ where Γ is the CFAR threshold set from the resulting $\chi^2_{2NN_\alpha}$ distribution. Examining the probability of detection P_D, the performance of the multi-CF detector can be approximated:

$$P_D \triangleq P\left[\mathcal{D}_s \geq \Gamma | \mathbb{H}_0\right] \tag{4.23}$$

Observing for a single CF, $\mathcal{D}_s$ is equivalent to the single-CF detector:

$$\lim_{M\to\infty} \mathcal{D}_s \Rightarrow \mathcal{N}\left(M\hat{\mathbf{r}}\hat{\Sigma}^{-1}\hat{\mathbf{r}}^{\mathbf{T}}, 4M\hat{\mathbf{r}}\hat{\Sigma}^{-1}\hat{\mathbf{r}}^{\mathbf{T}}\right) \tag{4.24}$$

Because the sum of Gaussian processes results in a Gaussian process:

$$\lim_{M\to\infty} \mathcal{D}_s \Rightarrow \mathcal{N}\left(M\sum_{\alpha\exists\mathcal{K}}\Psi, 4M\sum_{\alpha\exists\mathcal{K}}\Psi\right) \tag{4.25}$$

Then the P_D may be estimated with a similar evaluation of the error function:

$$P_D \approx \frac{1}{2} - \operatorname{erf}\left(\frac{\Gamma - M\sum_{\alpha\exists\mathcal{K}}\Psi}{\sqrt{2\cdot 4M\sum_{\alpha\exists\mathcal{K}}\Psi}}\right) \tag{4.26}$$

4.1.3 Ratio Detector

An alternative test statistic considers the ratio of the CAF response at a known CF to that of some other CF or lag which is known not to exist in the signal of interest [7][8]:

$$\Psi_\alpha = \left|\frac{\hat{R}_s(\alpha,\tau)}{\hat{R}_s(\alpha+S,\tau)}\right|, \quad (\alpha+S) \quad \nexists\mathcal{K} \tag{4.27}$$

$$\Psi_\tau = \left|\frac{\hat{R}_s(\alpha,\tau)}{\hat{R}_s(\alpha,\tau+x)}\right|, \quad (\tau+x) \quad \nexists\{\tau_n\}_{n=1}^N \tag{4.28}$$

The behavior of this statistic is analyzed under the following hypothesis test:

$$\begin{aligned}
\mathbb{H}_0 : \alpha \quad \nexists\mathcal{K} \quad \forall \quad \{\tau_n\}_{n=1}^N \Rightarrow \qquad & \hat{\mathcal{R}}_s(\alpha,\tau) = \epsilon_s(\alpha,\tau) \\
\mathbb{H}_1 : \alpha \quad \exists\mathcal{K} \quad \text{for some}\{\tau_n\}_{n=1}^N \Rightarrow & \hat{\mathcal{R}}_s(\alpha,\tau) = \mathcal{R}_s(\alpha,\tau) + \epsilon_s(\alpha,\tau)
\end{aligned}$$

ϵ is asymptotically complex normal. Under hypothesis $\mathbb{H}_0$ the test statistic Ψ becomes a ratio of normal distributions, which results in a Cauchy distribution[7][8]:

$$P\left[\Psi|\mathbb{H}_0\right] = \frac{1}{\pi\left(1+\Psi^2\right)} \tag{4.29}$$

A CFAR threshold is set using the CDF of the Cauchy distribution:

$$P_{FA} \triangleq P\left[\Psi \geq \Gamma|\mathbb{H}_0\right] = 1 - \left[\frac{1}{2} - \frac{\tan^{-1}(\Gamma)}{\pi}\right] \tag{4.30}$$

Table 4.1: *CAF Features For Detection of WiMAX Signals*

$\hat{\alpha}$	$\hat{\tau}$	Description
0	T_u	Cyclic Prefix
$\frac{1}{T_f}$	$\frac{T_u}{3}$	Preamble
0	T_f	Preamble
$\frac{1}{T_f}$	T_f	Preamble

Table 4.2: *Select χ^2_n Distribution Tail Values*

n	$P[X \geq x]$	x	n	$P[X \geq x]$	x	n	$P[X \geq x]$	x	n	$P[X \geq x]$	x
2	0.1	4.605	4	0.1	7.779	6	0.1	10.645	8	0.1	13.362
2	0.01	9.210	4	0.01	13.277	6	0.01	16.812	8	0.01	20.090
2	0.005	10.597	4	0.005	14.860	6	0.005	18.548	8	0.005	21.955
2	0.001	13.82	4	0.001	18.47	6	0.001	22.46	8	0.001	26.13

4.2 Hypothesis Test Approach

The previously described hypothesis tests can be grouped together into a library of cyclostationary detectors, as the underlying functionality is consistent across all three detectors. These three detectors are separated into two groups: single cycle and multi-cycle detectors. The first and third test discussed previously are classified as single-cycle detectors, with the multi-cycle test falling in the latter category.

The algorithms will accept the equivalent of in-phase and quadrature (IQ) samples from a receiver. In C++ these are specified as either `complex < float >` or `complex < double >` for single and double-precision floating point numbers, respectively. The CAF features used for detection are described it Table 4.1. Tables 4.2 and 4.3 provide selected threshold results from the χ^2_n and Cauchy distributions, respectively.

Table 4.3: *Select Cauchy Distribution Tail Values*

$P[X \geq x]$	x
0.1	3.078
0.01	31.82
0.005	63.66
0.001	318.3

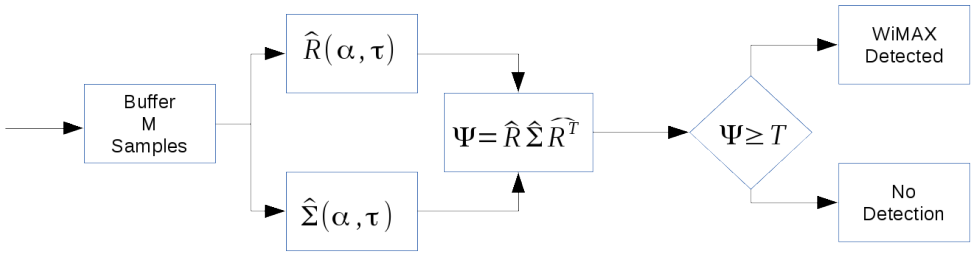

(a) *Block Diagram of the Single CF Detector*

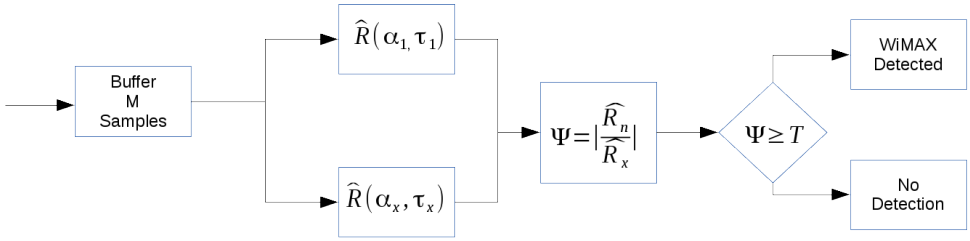

(b) *Block Diagram of the Ratio Detector*

Figure 4.1: *Block Diagrams of Detectors for Single CF*

4.2.1 Implementation

Figures 4.1a and 4.1b describe the basic algorithms for analysis of a single CF for detection of WiMAX systems. The CAF estimate $\mathcal{R}(\hat{\alpha},\tau)$ is performed as specified in Equation (3.4). The covariance matrix estimate $\hat{\Sigma}$ is computed with Equations (4.5), (4.10), and (4.11).

The multiple CF detector described in Figure 4.2 follows the computation of the decision statistic $\mathcal{D}_s$ in Equation (4.22). The thresholds for all three detectors are chosen from their corresponding distribution tables (Tables 4.2 4.3).

4.3 Pulsed Noise Interference

The pulsed "noise" applied to the received signal models a typical radar systems transmission. High energy and low duty cycle are the key characteristics of the pulsed signal. Within the pulses, psuedorandom biphase coding is used to model typical radar system pulse compression. Other techniques some radar systems use for pulse compression include frequency diversity and chirp sequences [20][21]. For modeling the effect of radar pulses upon these feature-based detection methods, the simple method of biphase modulation is sufficient to understand the effects of low duty cycle, high energy pulses. The rate of modulation is typically at least an order of magnitude over the pulse bandwidth.

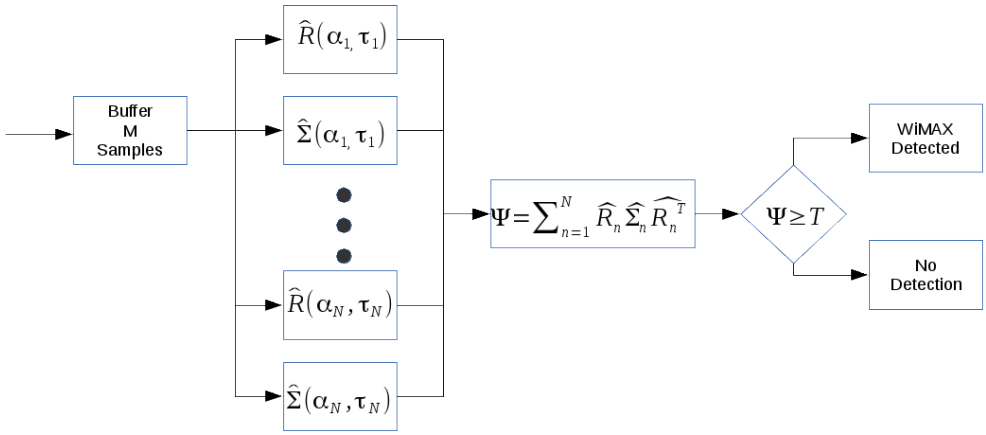

Figure 4.2: *Block Diagram of the Multiple CF Detector*

The previously described hypothesis tests were analyzed assuming a zero-mean AWGN process. The radar signal presents a unique noise process whose analysis in terms of these hypotheses is nontrivial. The psuedorandom codes used in the modulation sequence attempts to maximize the autocorrelation response (minimizing the correlation between pulses in any dwell). The computer algorithms used operate under the same AWGN assumption, and will be evaluated against the simulated puled noise.

4.4 SVM Approach

Machine learning techniques are attractive solutions to regression and binary classification problems [22][23]. The classic approach to formulating a linear classifier defines a relationship between a set of vectors $\mathbf{x}$ in some feature space that can be mapped to the set $y \exists \{-1, +1\}$. A hyperplane is drawn to separate the sets $\left[\{(\mathbf{x}_i, y_i = -1)\}_{i=1}^{N}, \{(\mathbf{x}_i, y_i = +1)\}_{i=1}^{N}\right]$ over a data set of size N with the form[23]:

$$\mathbf{wx} + b = \begin{cases} \geq 0 & y = +1 \\ < 0 & y = -1 \end{cases} \tag{4.31}$$

Figure 4.3 describes an example of a hyperplane $\mathbf{wx} + b = 0$ in a two-dimensional space with linearly separable data. One can note that small variations in certain data points near decision boundaries can result in changes of classification. While the classification boundary certainly fits the dataset, a casual observer may infer that it is not ideal. To minimize the number of data points near a decision boundary, a margin ϵ is introduced for

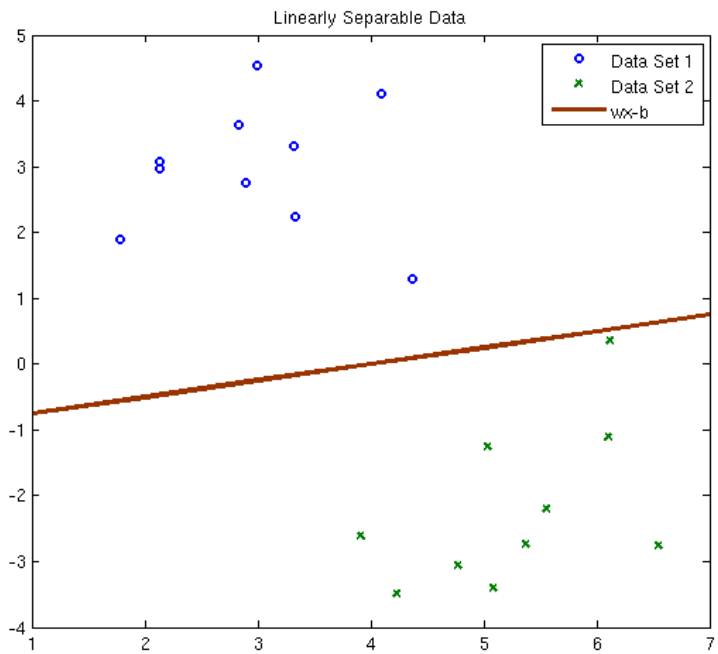

Figure 4.3: *Example of a Linear Classifier in Two Dimensions*

maximization[23]:

$$\mathbf{wx} + b = \begin{cases} \geq \epsilon & y = +1 \\ \leq -\epsilon & y = -1 \end{cases} \tag{4.32}$$

Any set of linearly independent data can be linearly separated with as many dimensions as data points. This is similar to the principle in communications of a modulation scheme containing a quantity of basis functions less than or equal to the number of symbols used. Likewise, one can think of the dimensions of a linearly separable data set as a set of basis functions from which the data set is generated. Figure 4.5 shows an example of a set of data represented in two dimensions whose basis functions cause the set of data to be inseparable linearly. One can apply a function to the data (the "kernel trick") to produce linearly separable data (as shown in Figure 4.6) :

The points which lie along the lines of maximum margin are known as support vectors. These support vectors define the decision boundaries of the classifier. Frequently it is impractical to provide a feature space with sufficient dimensionality to ensure linear separation of all training data. Support vector machines provide for a slack variable ξ to accommodate these inseparable mis-classifications. This slack variable is introduced to classifier as[23]:

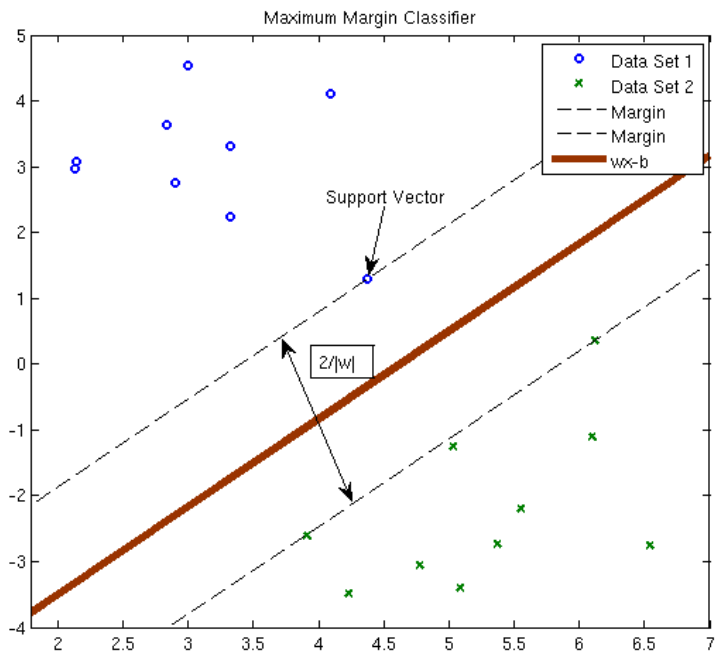

Figure 4.4: *Example of a Linear Classifier in Two Dimensions with Maximum Margin*

$$y_i\left(\mathbf{w}\mathbf{x}_i - b\right) \geq 1 - \xi_i \tag{4.33}$$

Where ξ is the distance from the margin, and if $\xi_i > 1$ for point i then the result is a mis-classification. A common approach to minimize mis-classifications is to constrain the system with a 2-Norm "soft margin" objective function:

$$\underset{\mathbf{w},\xi,b}{\operatorname{argmmin}} \left\{ \frac{1}{2}\left|\mathbf{w}\right|^2 + C\sum_{n=1}^{N}\xi_i \right\} \tag{4.34}$$

Optimizing Equation (4.34) is a quadratic programming exercise with computational cost $O(N^3)$[23]. The advantage an SVM would present over a multi-cycle GLRT detector comes at the computational savings avoiding the computation of the covariance matrix.

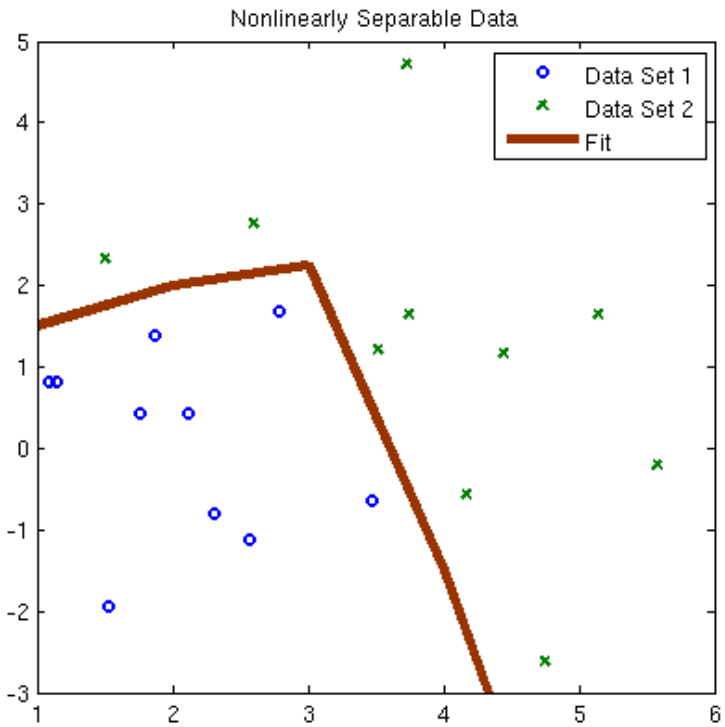

Figure 4.5: *Example of Non-Linearly Separable Data in Two Dimensions*

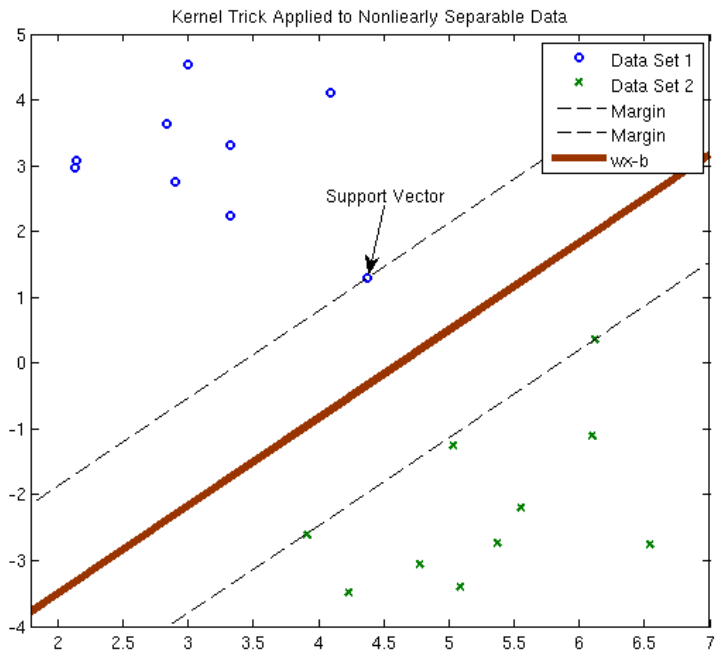

Figure 4.6: *Kernel Trick Applied to Data*

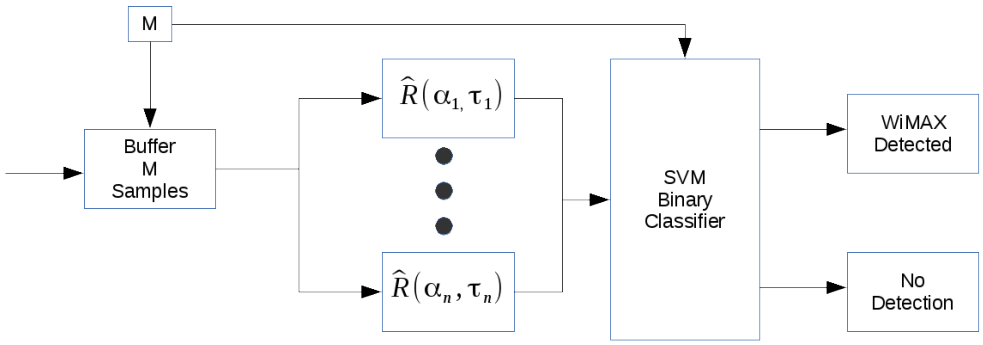

Figure 4.7: *Block Diagram of SVM Detector*

4.4.1 Implementation

Figure 4.7 shows a block diagram of the proposed SVM detector. The SVM requires a training sequence prior to evaluation. Three different types of training sequences will be used on the SVM detector: WiMAX without noise, WiMAX with 0dB SNR AWGN, WiMAX with 0dB SINR pulsed noise. The features used for the SVM classifier will be the test statistic computed at $(\hat{\alpha}, \hat{\tau}) = (0, T_u)$, $(\hat{\alpha}, \hat{\tau}) = (0, T_u/2)$ and the observation window length. Two kernels will be evaluated: Gaussian and χ^2.

The software used to construct the SVM framework is the SHOGUN SVM Toolbox (specifically, version 3.0.0)[24]. SHOGUN provides a C++ front-end to libSVM and other SVM libraries. Additionally SHOGUN expands upon available kernels and offers interfaces to other languages (MATLAB, Python, Ruby, etc.). Each kernel will require cross-validation to determine the optimal radial basis function width and weight of C for each classifier. These optimizations will be performed over the training data sets in a simple exhaustive search over a range of values for the parameters. The kernels with the least cross-validation error will be chosen to continue for evaluation. The result will be a total of three kernels available; the best Gaussian or χ^2 from each of the three training data sets.

Chapter 5

Evaluation of Detection Methods

The previous chapter identified four different second-order cyclostationary feature based detection methods. In this chapter these methods are evaluated against the classic AWGN channel; then their performance is evaluated in a simulated radar environment. The simulated radar signal consists of low duty cycle biphase modulated pulses with chip sequences generated from Gold Codes from the preferred pair $(X^{10}+X^3+1)$,$(X^{10}+X^8+X^3+X^2+1)$. The duty cycle of the radar pulses will be fixed at 1.5%, which is a reasonable approximation of the low duty cycle used by most radar systems. The coding rate is also fixed at 5MHz, which would provide a moderate range resolution of 30 meters to a radar system. Two different pulse repetition frequencies (PRFs) will be examined, 300Hz and 1500Hz. There PRFs were chosen to examine the effects of two different scenarios: one at 300Hz such that there are only one to two pulses per WiMAX frame (allowing for 32 symbol durations between pulses), and a second at 1500Hz which would provide much shorter duration pulses (one tenth of a symbol duration) at much greater frequency. Table 5.1 summarizes these radar parameters.

The WiMAX simulation will also be fixed in its parameters. Shown in Chapter 3, the CAF response magnitude at certain lags such as T_u are dependent upon the cyclic prefix length. Considering the CAF response is the magnitude squared of the cyclic prefix, a doubling or halving of the CP length results in a 6 dB gain or loss in response. For these analyses, the CP length is fixed at 1/8 with the understanding that the 1/4 length will have better perfor-

Table 5.1: *Radar System Parameters for Simulation*

Parameter	Value(s)
Duty Cycle	1.5%
PRF	[300,1500] Hz
Pulse Width	[50,250] μs
Coding Rate	5MHz

Table 5.2: *WiMAX System Parameters for Simulation*

Parameter	Value(s)
FFT Size	512
CP Length	1/8
Useful Symbol Duration	91.429 μs
Total Symbol Duration	102.857 μs
Frame Duration	5 ms
Symbols Per Frame	47

Table 5.3: *WiMAX Detection Decision Engines*

Multi-Cycle GLRT
Single-Cycle GLRT
Single-Cycle "Ratio Test"
SVM with No-Noise training
SVM with 0dB SNR AWGN training
SVM with 0dB SINR Pulsed Noise training

mance and the 1/16 will have worse performance. The FFT size of the symbol only affects the system bandwidth. For these simulations, the FFT size is fixed at 512, which results in a system bandwidth of 5.6MHz; all system parameters are reviewed in Table 5.2. The WiMAX is upsampled to 10MHz and combined with the radar signal generated at 10MHz, effectively simulating 5.6MHz of receiver bandwidth sampled at 10MHz.

5.1 Simulation Parameters

The previous section described the fixed parameters of the radar and WiMAX systems for simulation. The simulation architecture will vary other parameters to compare the performance of the four detectors in the AWGN and radar noise environments. The decision engines under consideration are defined in Table 5.3. The CFAR parameters and observation window length M for the decision engines are described in Table 5.4. Table 5.5 describes the different noise environments tested. For each pulsed noise range, the underlying AWGN noise is varied from -10dB to 30dB SNR in 10 dB steps (four AWGN levels per pulsed noise SINR sweep).

Table 5.4: *Decision Engine Parameters*

Attribute	Parameter
CFAR P_{FA}	[0.1,0.01]
$\frac{M}{T_s}$	[5,10,25,50,100,250,500] symbol durations

Table 5.5: *Simulation Noise Parameters*

Noise Type	Noise Level	Other Parameters
AWGN	-15:3:12 dB SNR	
Pulsed Noise	-10:5:30 dB SINR	PRF 300 Hz
Pulsed Noise	-10:5:30 dB SINR	PRF 1500 Hz

5.2 Simulation Resolution

The simulations were designed to generate a series of test data corresponding to ten trials of 500-symbol windows at most two times per configuration. The resolution of the simulation increases with decreasing window size, as the smaller windows are run over the large dataset generated for the 500-symbol window. For example, each test run of ten trials of 500-symbols yields over 1,000 trials for the 5-symbol window.

Limiting the test runs to a maximum of 20 trials for the 500-symbol window restricts the resolution. This can be improved with a greater number of trials at the cost of greatly increasing computation time. The CAF estimator and covariance estimator are implemented using their formal definition. While Fast Fourier Transform techniques can produce similar estimates, they were not implemented in favor of establishing a proof-of-concept simulation using the aforementioned estimate definitions.

5.3 Selected Results

The entire results from the described simulations are contained in Appendix A (approximately 286 plots). Some of the results are selected for discussion in this chapter. The reader is encouraged to review all of the plots contained in the Appendix.

5.3.1 Cauchy Ratio Test

The Cauchy Ratio Test is the least complex of all the decision algorithms. Figure 5.1 demonstrates the ratio test in against an AWGN channel. The legend of the graphs describe the

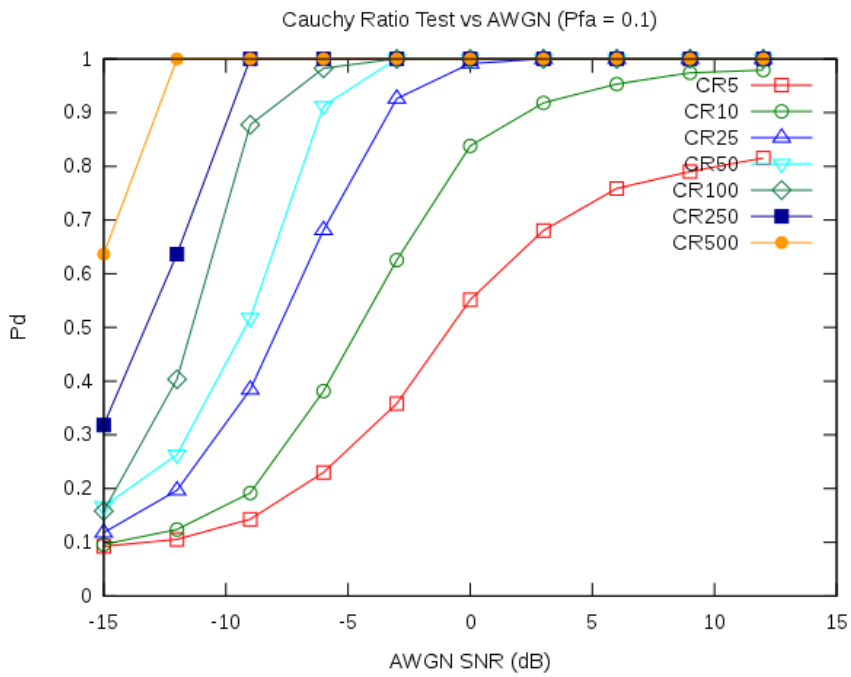

Figure 5.1: *CRT P_d vs. AWGN with 10% False Alarm Rate*

observation window in terms of WiMAX useful symbol durations (about 102μs). "CR5" corresponds to a 5-symbol observation window and "CR250" corresponds to a 250-symbol observation window. This ratio test, as a tradeoff in computational complexity, does not estimate the covariance matrix of the observed signal and relies on the CAF response at a known non-CF of the signal. Figures 5.2a and 5.2b demonstrate the effectiveness of this technique in the presence of a pulsed radar signal.

Many cyclostationary techniques work well below the 0dB SNR threshold given long observation windows. To highlight the performance of these detectors in this chapter, the 0dB SNR was chosen. While the techniques may work below 0dB SNR, a deliberately designed sensor should yield satisfactory SNR levels with the desired signal. The Appendix contains additional analysis from -10 dB through 30 dB SNR.

5.3.2 General Likelihood Ratio Test

The GLRT is more robust against noise, as the test statistic incorporates a covariance estimate. Figure 5.3a demonstrates the single-cycle GLRT detector against AWGN with a 10% CFAR threshold. Figure 5.3b illustrates the performance of the four-cycle GLRT detector, also with a 10% CFAR threshold. Due to the lags for cycles three and four in the multi-cycle

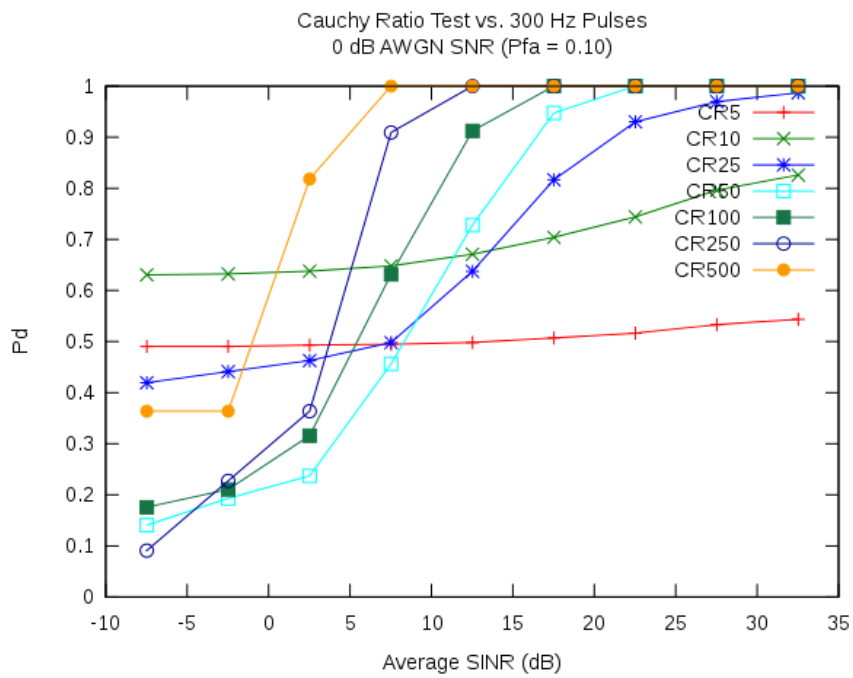

(a) *CRT P_d vs. 300Hz Pulses with 10% False Alarm Rate*

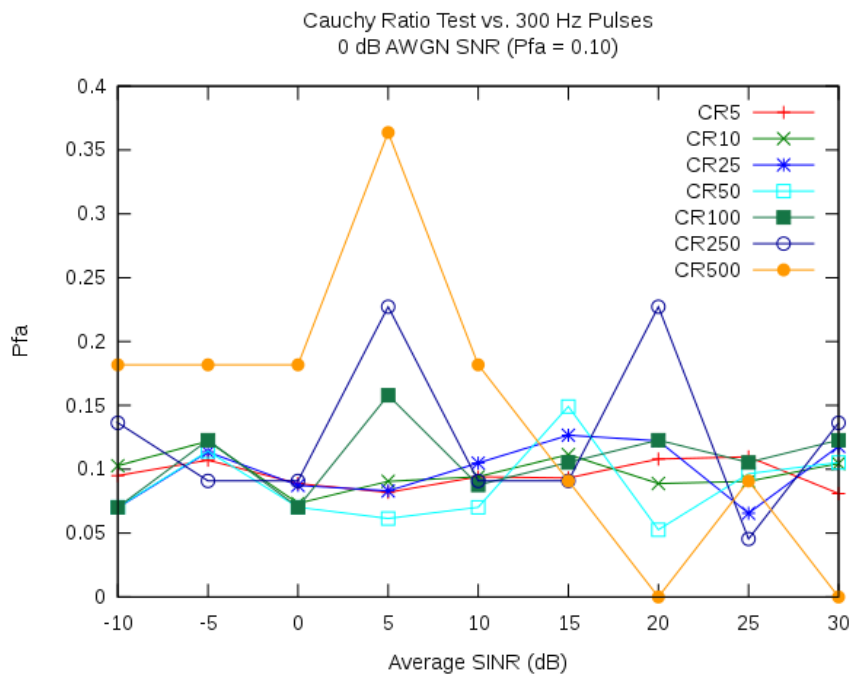

(b) *CRT P_{fa} vs. 300Hz Pulses with 10% False Alarm Rate, 0 dB AWGN SNR*

Figure 5.2: *Cauchy Ratio Test vs. 300Hz Pulses with 10% False Alarm Rate, 0 dB AWGN SNR*

Table 5.6: *SVM Parameters*

Training Data Description	Kernel Type	libsvm C1	libsvm C2	RBF Width	Cross-Validation Error Rate
AWGN	χ^2	7.61	11.62	6.53	0.00608
No Noise	χ^2	1.9	2.9	15.9	0.00267
Pulse Noise	Gaussian	1.6	2.6	12.5	0.03442

detectors, the minimum observation window used in the simulation is 100 symbol periods. A 5 ms WiMAX frame has only 49 T_U periods, and the 50 symbol observation window yields a very small number of samples over which the cross-correlation is evaluated.

Introducing the same level of pulsed radar interference from Figure 5.2a, the GLRT single-cycle detector is evaluated in Figures 5.4a and 5.4b. The single-cycle detector is impacted by the pulse energy, and degrades its performance (Figure 5.3a). However, the false alarm rate of the single-cycle detector is more manageable than that of the Cauchy Ratio Test detector, as it typically surpassed it's CFAR performance.

Expanding upon the single-cycle detector, the four-cycle detector utilizes a summation of several CF decision statistics. It's AWGN performance (Figure 5.3b vs 5.3a) is significantly greater than that of the single-cycle detector, however it's P_d in the pulsed environment is nearly identical to the single-cycle detector (Figure 5.5a vs. 5.4a). The advantage of the four-cycle detector over the single-cycle detector rests with it P_{fa} performance, and rejecting false positives from the interfering signal (Figure 5.5b vs. 5.4b).

5.3.3 Support Vector Machine Detector

The three SVMs were trained with a series of 600 "positive" vectors and 600 "null" vectors. The groups of 600 were divided into 100-vector groups, each with a different observation window length. Thus there are 100 vectors from a 5-symbol observation, 100 vectors from a 10-symbol observation, etc. for the set of [5,10,50,100,250,500]. Optimal SVM parameters were found using a linear search over a range of slack weights and basis function widths. Two different kernels were also tested in the linear search. The search was evaluated using a 10-fold cross validation on the respective data set with ten runs. Table 5.6 shows the SVM and kernel parameters used for each machine. The trained SVMs were then run against the complete training data set to evaluate their efficacy before in-depth simulations were run. These results are shown it Table 5.7, whose diagonal represents the "training error" of the SVMs.

The disparity of results between the training data set and the AWGN evaluation indicate

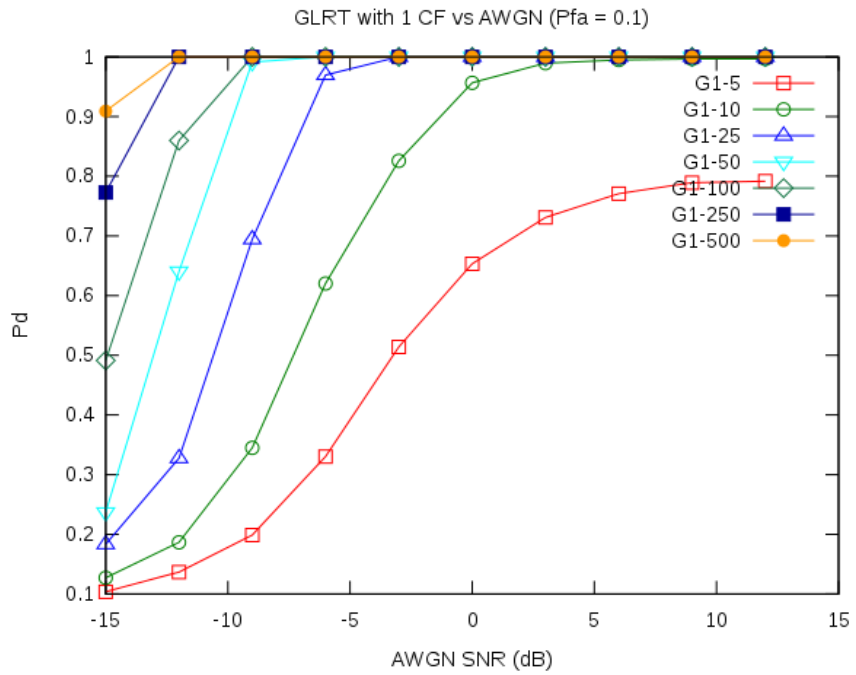

(a) *GLRT 1 CF P_d vs. AWGN with 10% False Alarm Rate*

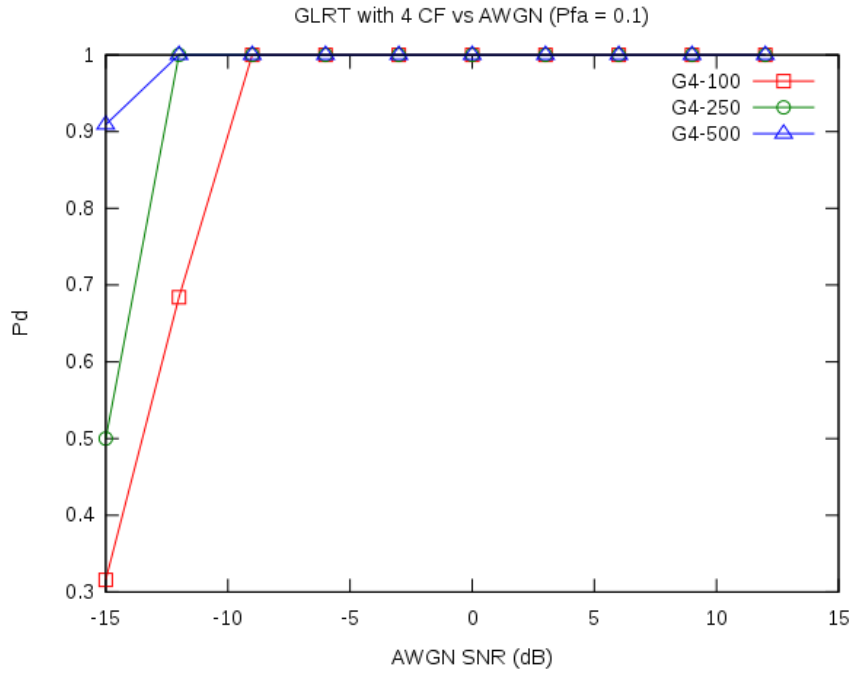

(b) *GLRT 4 CF P_d vs. AWGN with 10% False Alarm Rate*

Figure 5.3: *Selected GLRT Results*

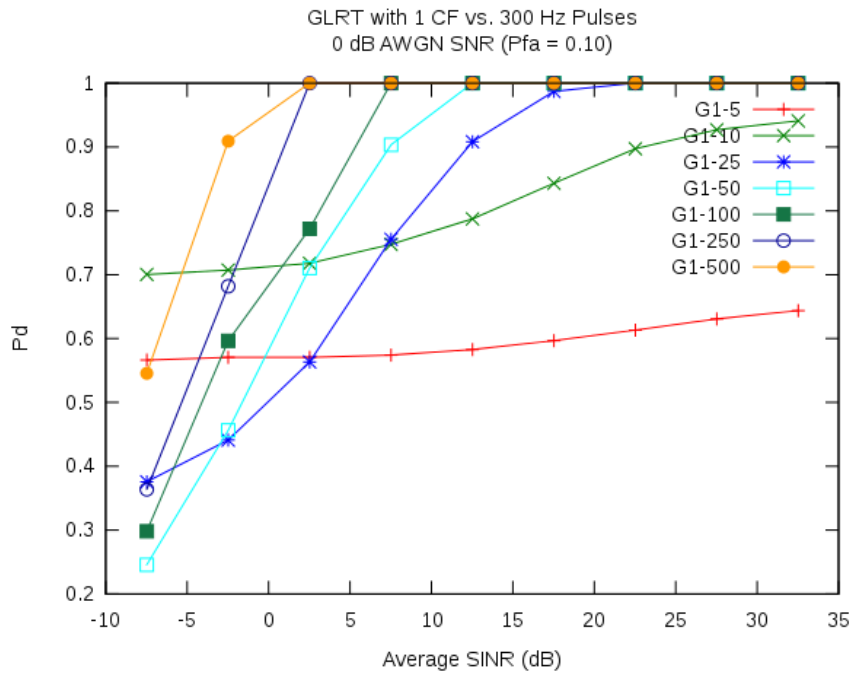

(a) P_d

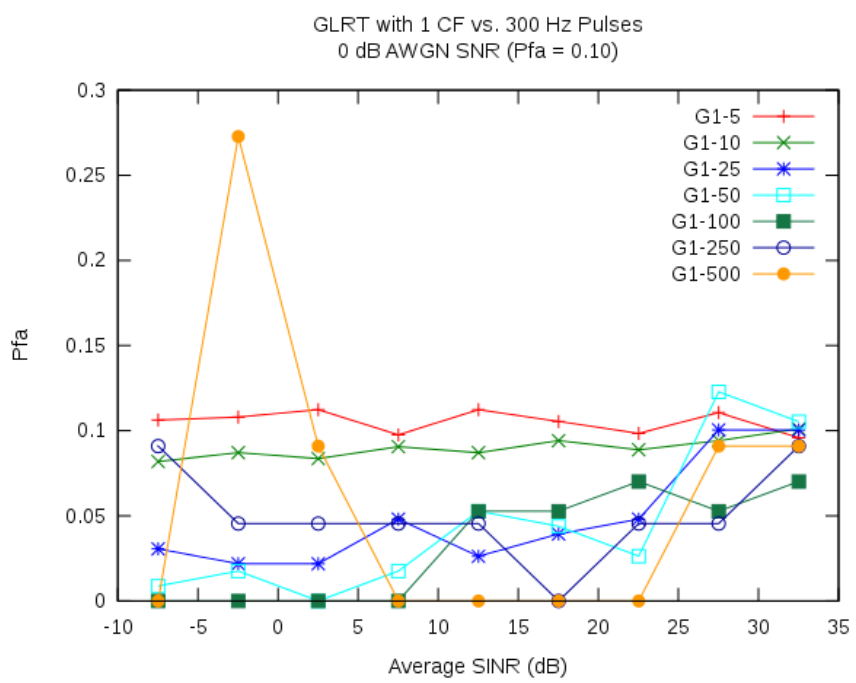

(b) P_{fa}

Figure 5.4: *GLRT 1 CF vs. 300Hz Pulses with 10% False Alarm Rate, 0 dB AWGN SNR*

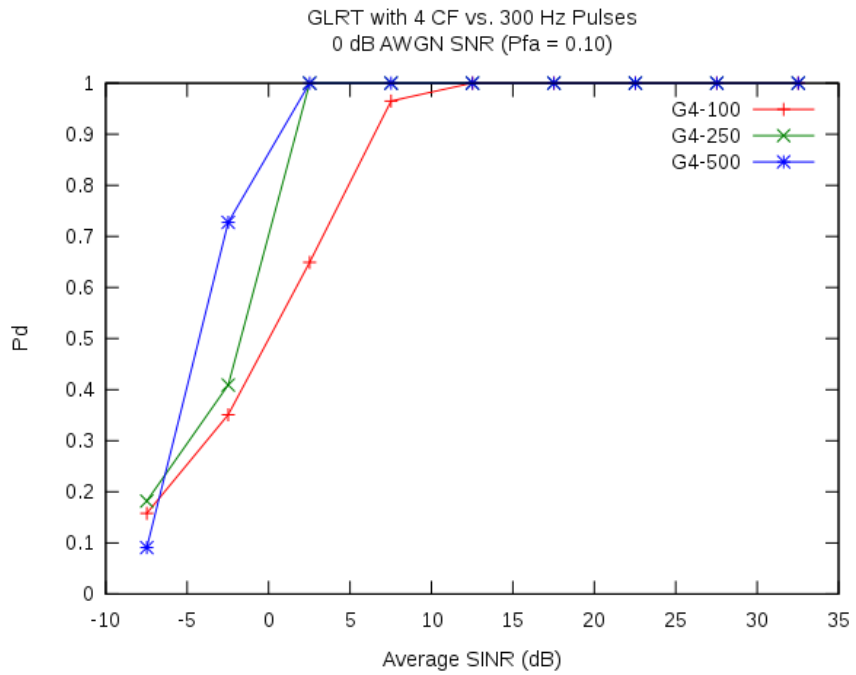

(a) P_d

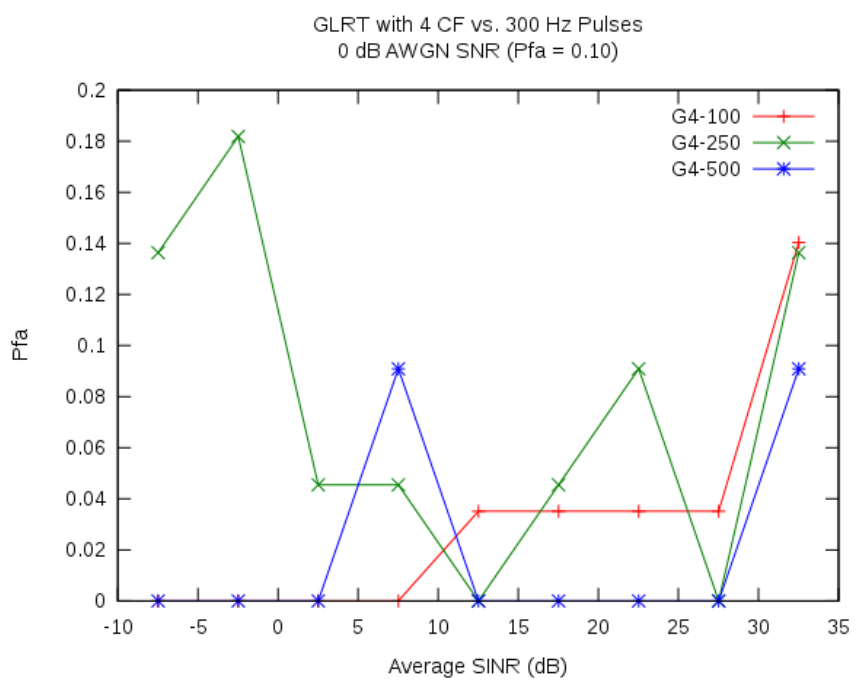

(b) P_{fa}

Figure 5.5: *GLRT 4 CF vs. 300Hz Pulses with 10% False Alarm Rate, 0 dB AWGN SNR*

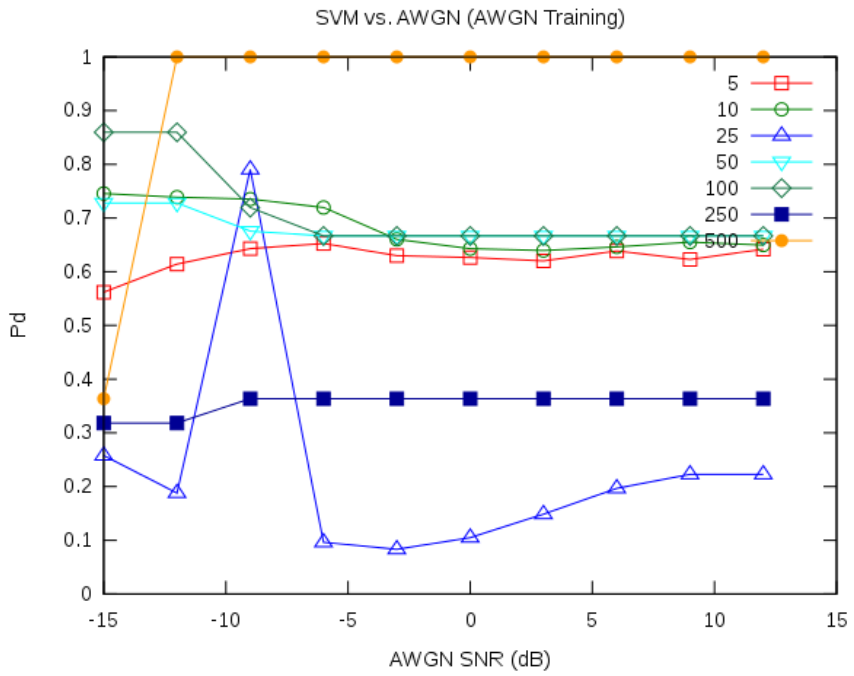

(a) *SVM Detector with 0dB AWGN Training P_d vs. AWGN*

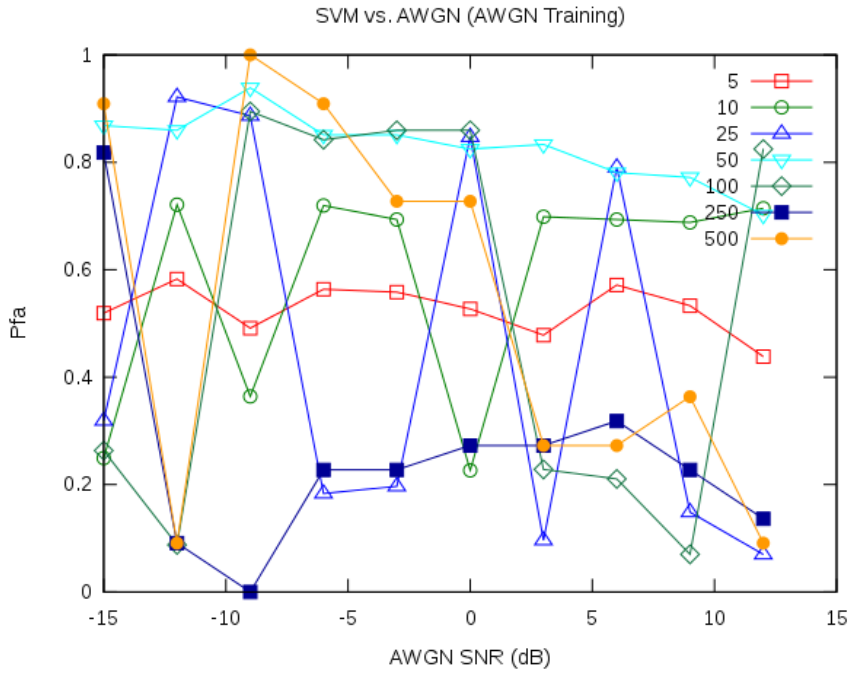

(b) *SVM Detector with 0dB AWGN Training P_{fa} vs. AWGN*

Figure 5.6: *Selected SVM vs. AWGN Results*

Table 5.7: *SVM Training Results*

SVM \ Data	AWGN	No Noise	Pulse
AWGN	0.0050	0.1883	0.0567
No Noise	0.1025	0.0025	0.1383
Pulse	0.1400	0.1275	0.0258

an improper fit to the signal of interest. This can result from a binary classifier which is over-fit to the training data, improper feature selection, or implementation errors moving from training data to evaluation data. In the case of the AWGN evaluations in Figures 5.6a and 5.6b, only the 500-symbol window behaves as expected: low P_d at lower SNRs, and low P_{fa} at higher SNRs.

5.4 Summary & Observations

In this chapter, the method of evaluation for the various detectors was discussed. Selected results were presented, with complete results available in Appendix A for all test cases. The GLRT works reasonably well when exposed to pulses, but only at favorable SINR levels ($>$ 0dB). Examining the additional results in the Appendix will show that the 300 Hz pulses affect the performance of the GLRT more than the 1500 Hz pulses. The SVM approach shows some promise as indicated with the 300 Hz performance, but as shown with the AWGN and 1500 Hz, the features selected for the SVM and the degree of fit are likely inappropriate for this data set.

The Cauchy Ratio Test, at long observation windows (250, 500 symbols) and a $P_{fa} = 0.1$, yields performance about 10 dB under those of the GLRT with one and two CFs. The evaluated P_{fa} under the radar noise for the CRT remained consistent with the CFAR threshold, while the GLRT typically surpassed the CFAR performance. An advantage to choosing the CRT over the GLRT is the CRT does not require the computation of a covariance matrix. The CRT, as defined earlier is simply the ratio of the CAF response at a known CF and a known non-CF.

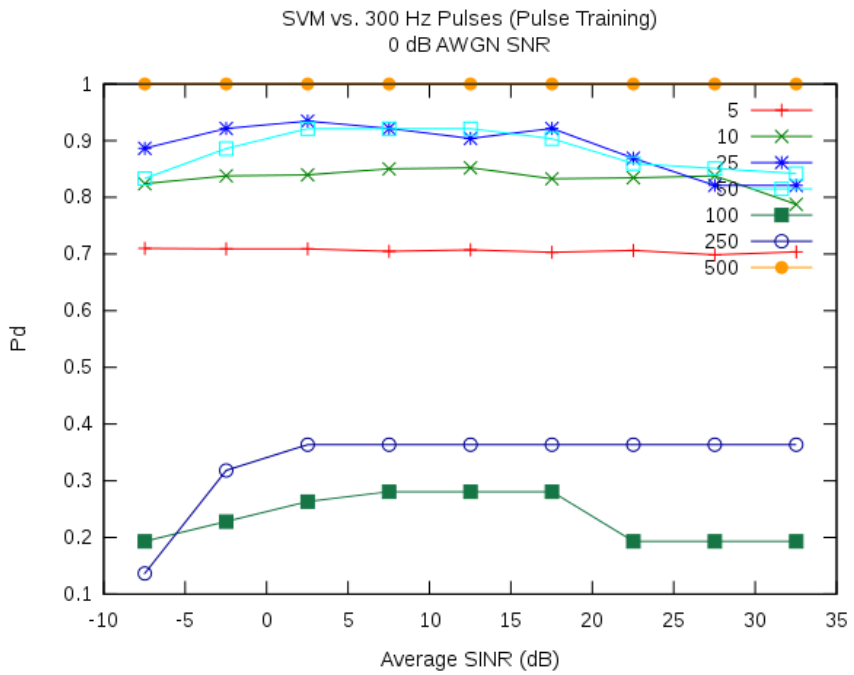

(a) *SVM Detector with 0dB SINR Pulse Training P_d vs. 300Hz Pulses, 0 dB AWGN SNR*

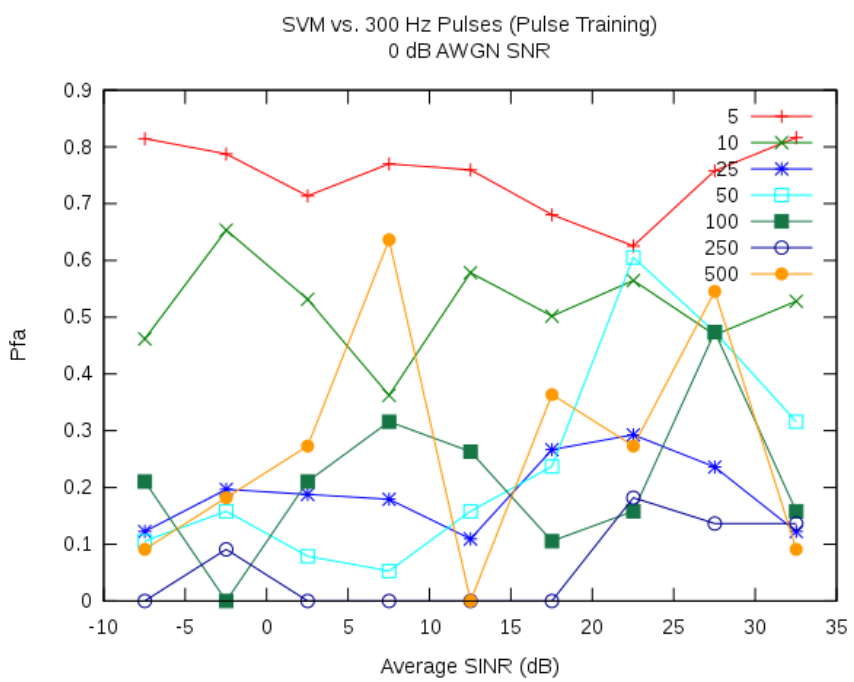

(b) *SVM Detector with 0dB SINR Pulse Training P_d vs. 300Hz Pulses, 0 dB AWGN SNR*

Figure 5.7: *Selected SVM vs. 300 Hz Pulses Results*

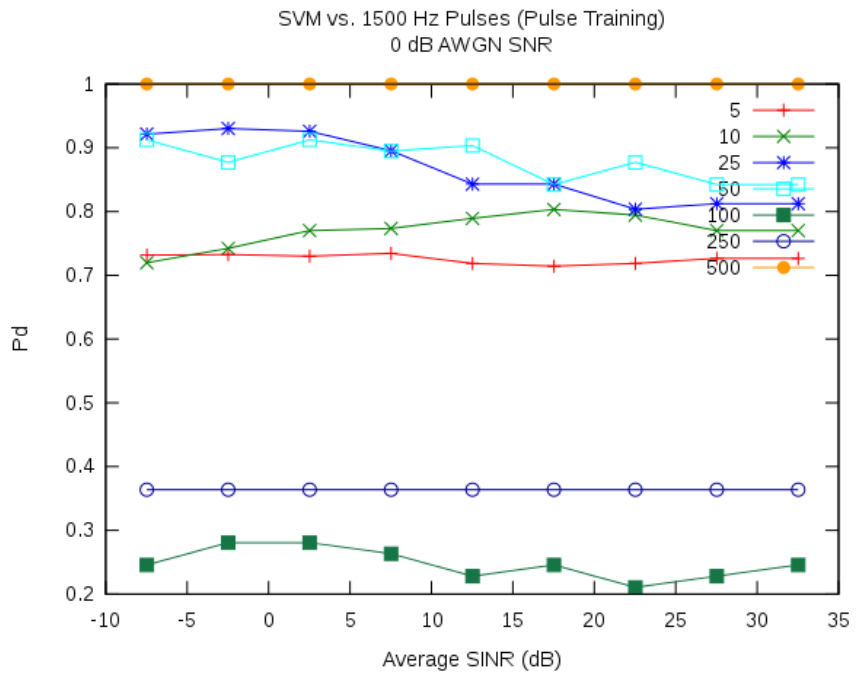

(a) *SVM Detector with 0dB SINR Pulse Training P_d vs. 1500Hz Pulses, 0 dB AWGN SNR*

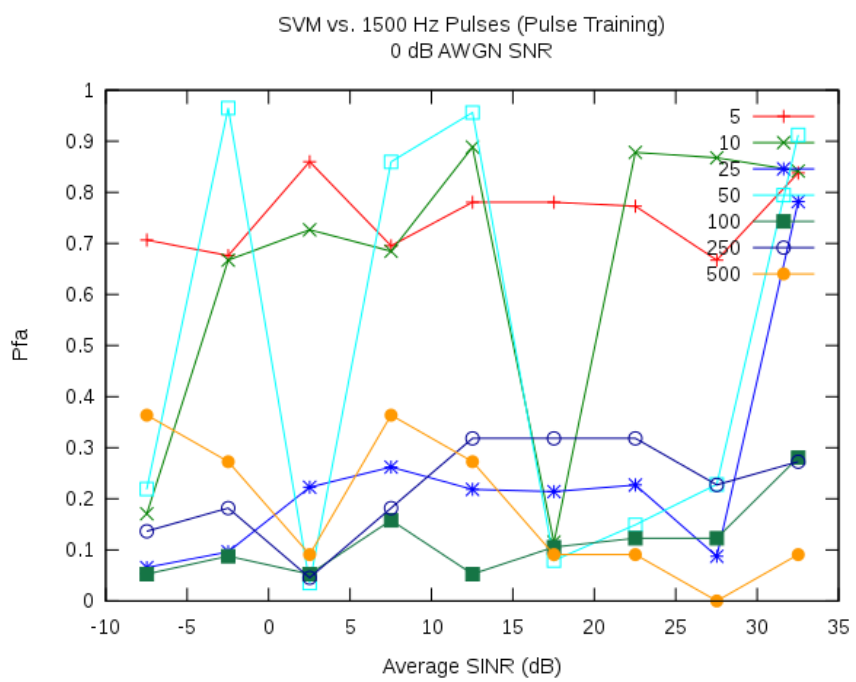

(b) *SVM Detector with 0dB SINR Pulse Training P_{fa} vs. 1500Hz Pulses, 0 dB AWGN SNR*

Figure 5.8: *Selected SVM vs. 1500 Hz Pulses Results*

Chapter 6

Conclusion

The presence of high energy pulsed noise can create unique challenges for congnitive radio and spectrum sharing. This thesis examined the application of second order cyclostationary features to the detection of WiMAX signals in the presence of AWGN and pulsed noise. In addition to classical general likelihood ratio tests, a support vector machine solution was proposed and evaluated. All of the detectors were evaluated in an array of varying noise parameters and observation window length to determine the optimum application of these second order statistics.

6.1 Detector Analysis & Recommendation

Chapter Five presented the evaluation methods and selected results of the detectors considered. Table 6.1 describes the performance difference between two of the least computationally complex detection methods. The CRT requires the computation of two CAF estimates. Each CAF estimate, when computed with the formal definition of the CAF has a computational complexity of $O(N^2)$. If one applies FFT approximation techniques to the CAF, the complexity is reduced to $O(N \log N)$.

Table 6.1: *90% P_d SINR Threshold in 0 dB AWGN SNR, $P_{fa} = 10\%$, 300 Hz Pulses*

Detector Type	Observation Length	SINR	Detector Type	Observation Length	SINR
Cauchy	500	5	GLRT 1 CF	500	-3
Cauchy	250	7	GLRT 1 CF	250	1
Cauchy	100	12	GLRT 1 CF	100	5
Cauchy	50	17	GLRT 1 CF	50	7
Cauchy	25	22	GLRT 1 CF	25	12

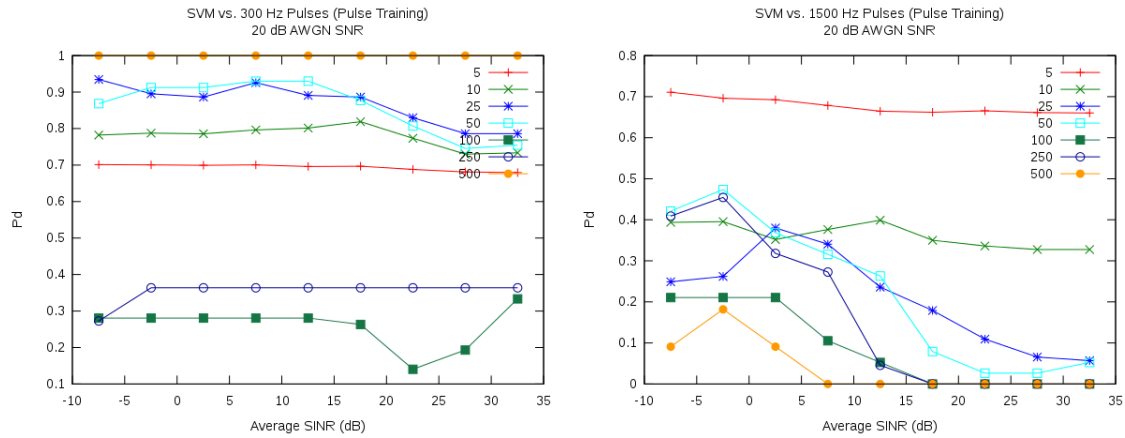

(a) *SVM vs. 300Hz Pulses with Pulse Training, 20 dB AWGN SNR* **(b)** *SVM vs. 1500Hz Pulses with Pulse Training, 20 dB AWGN SNR*

Figure 6.1: *SVM Detector Performance in High AWGN SNR*

The GLRT requires the estimation a covariance matrix Σ. The operations required for the Σ estimate have a cost $O(N^2)$[11]. In the case of the multiple CF tests, the complexity scales linearly as an $O(N^2)$ test statistic must be calculated for each CF of interest. The SVM detector evaluated uses two test statistic computations as features, this equates the SVMs computational cost to that of the GLRT with two CFs; two $O(N^2)$ operations are required.

In evaluating the SVM performance, the 1500 Hz data set showed that the SVM was over-fit to the 300 Hz data. Figure 6.1b shows very poor performance in favorable AWGN SNR levels while Figure 6.1a shows satisfactory (but not ideal) performance in the same AWGN SNR.

Examining different observation window lengths, Figure 6.2a shows that a small window at low PRFs can provide asymptotic performance with the bulk of the successful detections occurring between the radar pulses. The high PRF results of Figure 6.2b demonstrate the advantage of long integration periods when it is impossible to perform signal analysis in between pulses.

An ideal detector would achieve a balance of high refresh rate and high probability of detection when subjected to radar signals. Using the discussed results, a two-step detector is recommended. Incoming samples from the receiver would first go through a single-cycle GLRT detector with a short observation window length (e.g. 10 T_U). Using a 2-of-3 criterion and a 10% CFAR threshold, the P_d and P_{fa} become:

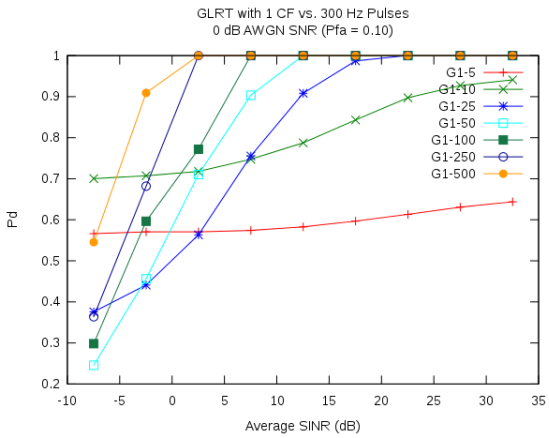

(a) *GLRT 1 CF vs. 300Hz Pulses with 10% False Alarm Rate, 0 dB AWGN SNR*

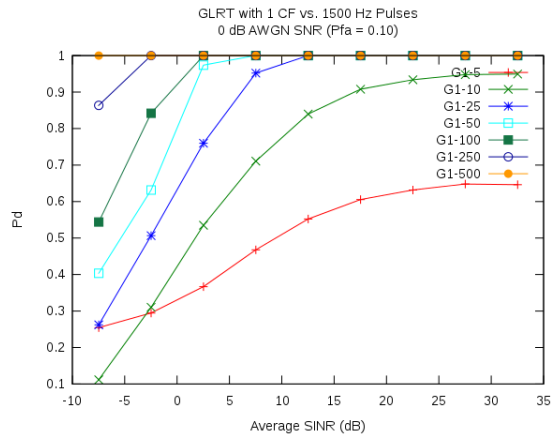

(b) *GLRT 1 CF vs. 1500Hz Pulses with 10% False Alarm Rate, 0 dB AWGN SNR*

$$P' = 3P^2 - 2P^3 \tag{6.1}$$

This will yield a 2.8% CFAR. In the case of 0dB AWGN SNR in the presense of 300 Hz pulses, this will result in an asymptotic P_d of 78.4%. The second level of this detector should be user (or cognitive engine) selectable. If the system is in an area where WiMAX systems are known to exist (or if the radar system is operating with a high PRF), then the second detector should perform an evaluation on samples when the first detector's algorithm results in "No Detection."

A multi-cycle detector should be used for this second level. The number of cycles and observation period should be tuned to the systems computational capabilities and desired refresh rate. Calculating a 4-cycle statistic on an observation window size of >500 T_U is much more costly than a 2-cycle statistic on a 250 T_U window.

6.2 Future Work

The library of C++ code created to support this work implemented the formal definition of all algorithms. Significant performance gains will be realized with a refactoring of the code and implementation of FFT techniques for CAF calculation and test statistic computations[25]. After refactoring and implementation of more efficient calculation methods, testing can be performed on the proposed two-step detector. The proposed SVM classifier shows promise; in the case of the data presented in this thesis, the features or kernels selected were insufficient to provide for robust classification. For each set of possible features, the entire analysis routine is required: kernel evaluation, parameter optimization, and evaluation. Once more

appropriate features are identified, the SVM can be trained as a multi-class classifier with other similar signals (such as LTE, DVB-T, etc.) to perform joint detection and classification.

Beyond optimizing the existing algorithms, additional tests are required to ensure robustness of the final detection algorithm. There will be some PRF threshold where the initial small observation window detector yields insufficient probability of detection to justify its use. The data presented here focused on in-channel interference from a radar system. Additionally the radar was limited to 5MHz of bandwidth, slightly less than the WiMAX system bandwidth. Other combination of system bandwidths, in-channel, and adjacent-channel bandwidths should be evaluated. The WiMAX test signal utilized the WirelessMAN-OFDMA specification. The AAI interface was not evaluated. Because the AAI introduces additional preambles, some gains are expected on the 3-cycle and 4-cycle GLRT detectors. The performance of the detector with the AAI should be evaluated and compared to that of the WirelessMAN-OFDMA.

Another aspect not considered in this thesis is the susceptibility of the detector to spoofing. Because the primary detection methods rely upon the cyclic-prefix induced cyclostationarity, other systems which have useful symbol durations close to that of WiMAX can cause false alarms within the detector. Depending upon the operational goals of the detector, rejection of these false positives may be desired. If rejection of false positives and spoofing is required, then the system should use more identifying features of WiMAX to filter the false positives. Some of these features may include pilot tone sequences or other standardized structures within the signal.

Bibliography

[1] "Ieee standard for air interface for broadband wireless access systems," *IEEE Std 802.16-2012 (Revision of IEEE Std 802.16-2009)*, pp. 1–2542, 2012.

[2] W. A. Gardner, *Statistical Spectral Analysis: A Nonprobabilistic Theory*. Prentice Hall, 1988.

[3] A. Dandawate and G. Giannakis, "Statistical tests for presence of cyclostationarity," *Signal Processing, IEEE Transactions on*, vol. 42, no. 9, pp. 2355–2369, 1994.

[4] J. Lunden, V. Koivunen, A. Huttunen, and H. Poor, "Spectrum sensing in cognitive radios based on multiple cyclic frequencies," in *Cognitive Radio Oriented Wireless Networks and Communications, 2007. CrownCom 2007. 2nd International Conference on*, pp. 37–43, 2007.

[5] F.-X. Socheleau, P. Ciblat, and S. Houcke, "Ofdm system identification for cognitive radio based on pilot-induced cyclostationarity," in *Wireless Communications and Networking Conference, 2009. WCNC 2009. IEEE*, pp. 1–6, 2009.

[6] A. Al-Habashna, O. Dobre, R. Venkatesan, and D. Popescu, "Wimax signal detection algorithm based on preamble-induced second-order cyclostationarity," in *Global Telecommunications Conference (GLOBECOM 2010), 2010 IEEE*, pp. 1–5, 2010.

[7] A. Tani and R. Fantacci, "A low-complexity cyclostationary-based spectrum sensing for uwb and wimax coexistence with noise uncertainty," *Vehicular Technology, IEEE Transactions on*, vol. 59, no. 6, pp. 2940–2950, 2010.

[8] T. Bogale and L. Vandendorpe, "Multi-cycle cyclostationary based spectrum sensing algorithm for ofdm signals with noise uncertainty in cognitive radio networks," in *MILITARY COMMUNICATIONS CONFERENCE, 2012 - MILCOM 2012*, pp. 1–6, 2012.

[9] A. Al-Habashna, O. Dobre, R. Venkatesan, and D. Popescu, "Joint signal detection and classification of mobile wimax and lte ofdm signals for cognitive radio," in *Signals, Systems and Computers (ASILOMAR), 2010 Conference Record of the Forty Fourth Asilomar Conference on*, pp. 160–164, 2010.

[10] A. Al-Habashna, O. Dobre, R. Venkatesan, and D. Popescu, "Joint cyclostationarity-based detection and classification of mobile wimax and lte ofdm signals," in *Communications (ICC), 2011 IEEE International Conference on*, pp. 1–6, 2011.

[11] A. Al-Habashna, "Joint detection and classification of the ofdm-based mobile wimax and lte signals for cognitive radio," 2010. Copyright - Copyright ProQuest, UMI Dissertations Publishing 2010; Last updated - 2012-07-05; First page - n/a; M3: M.Eng.

[12] S. Ahmadi, *Mobile WiMAX: A Systems Approach to Understanding IEEE 802.16m Radio Access Technology.* Academic Press, 2011.

[13] J. G. Andrews, A. Ghosh, and R. Muhamed, *Fundamentals of WiMAX: Understanding Broadband Wireless Networking.* Prentice Hall, 2007.

[14] S. G. Glisic, *Advanced Wireless Communications 2nd Ed.* John Wiley & Sons, 2007.

[15] S. G. Glisic, *Advanced Wireless Networks: 4G Technologies.* John Wiley & Sons, 2006.

[16] "Ieee standard for wirelessman-advanced air interface for broadband wireless access systems," *IEEE Std 802.16.1-2012*, pp. 1–1090, 2012.

[17] A. Lackpour, M. Luddy, and J. Winters, "Overview of interference mitigation techniques between wimax networks and ground based radar," in *Wireless and Optical Communications Conference (WOCC), 2011 20th Annual*, pp. 1–5, 2011.

[18] J. G. Proakis and M. Salehi, *Digital Communications.* McGraw-Hill, 2008.

[19] A.-E. M. Taha, H. S. Hassanein, and N. A. Ali, *LTE, LTE-Advanced and WiMAX: Towards IMT-Advanced Networks.* John Wiley & Sons, 2012.

[20] M. A. Richards, J. A. Scheer, and W. A. Holm, *Principles of Modern Radar: Basic Principles.* Scitech Publishing, 2010.

[21] N. Levanon and E. Mozeson, *Radar Signals.* John Wiley & Sons, 2004.

[22] D. Barber, *Bayesian Reasoning and Machine Learning.* Cambridge University Press, 2012.

[23] I. Steinwart and A. Christmann, *Support Vector Machines.* Springer Science and Business Media, LLC, 2008.

[24] V. Gal, F. Iglesias, H. Strathmann, S. Lisitsyn, and S. Sonnenbur, "Shogun svm toolbox." Multi-Language Library http://shogun-toolbox.org/.

[25] R. Roberts, W. Brown, and H. Loomis, "Computationally efficient algorithms for cyclic spectral analysis," *Signal Processing Magazine, IEEE*, vol. 8, no. 2, pp. 38–49, 1991.

Appendix A

Results

A.1 Cauchy Ratio Test

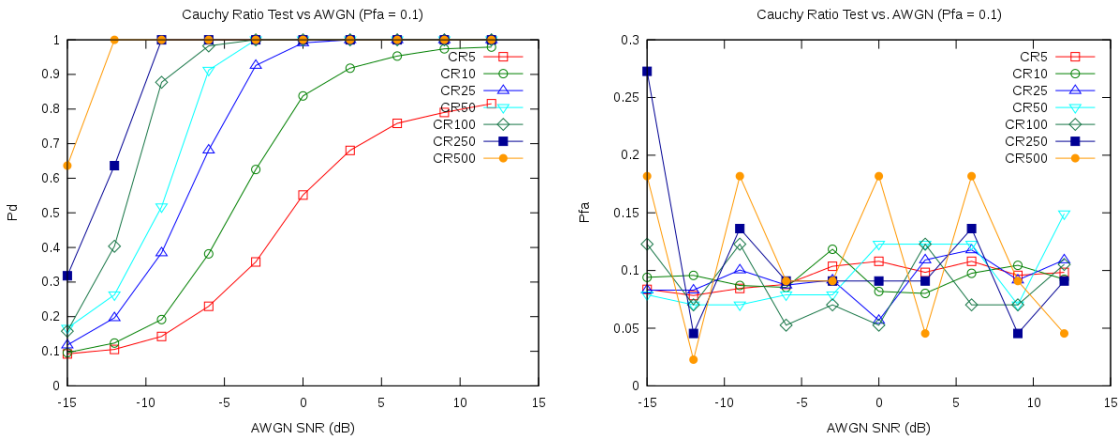

(a) P_d **(b)** P_{fa}

Figure A.1: *CRT vs. AWGN with 10% False Alarm Rate*

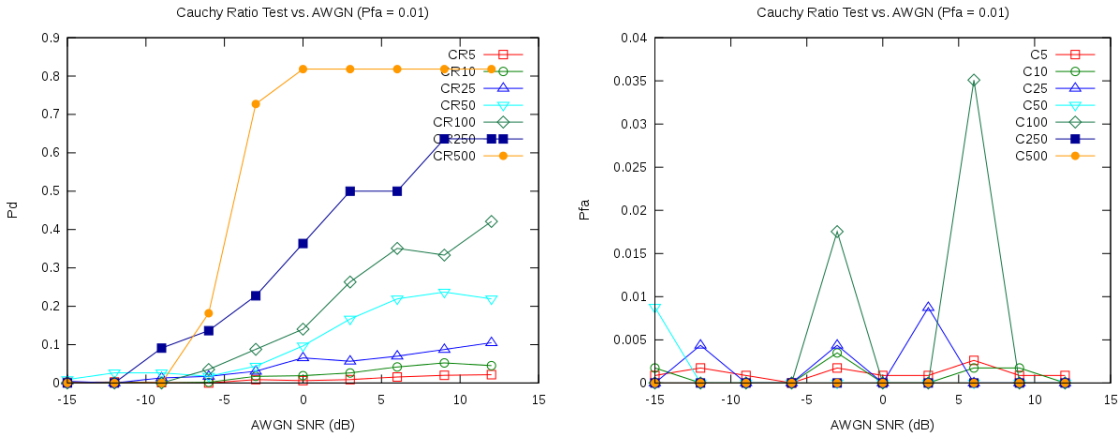

(a) P_d **(b)** P_{fa}

Figure A.2: *CRT vs. AWGN with 1% False Alarm Rate*

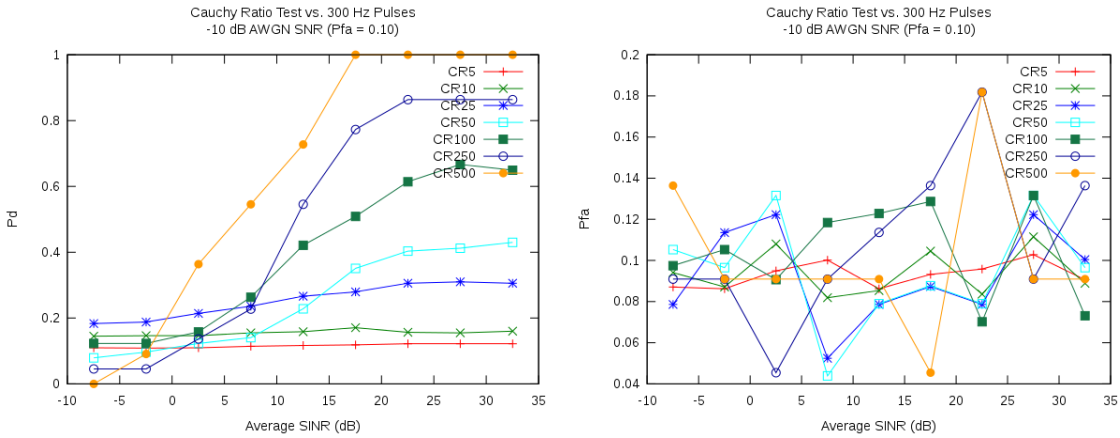

(a) P_d **(b)** P_{fa}

Figure A.3: *CRT vs. 300Hz Pulses with 10% False Alarm Rate, -10 dB AWGN SNR*

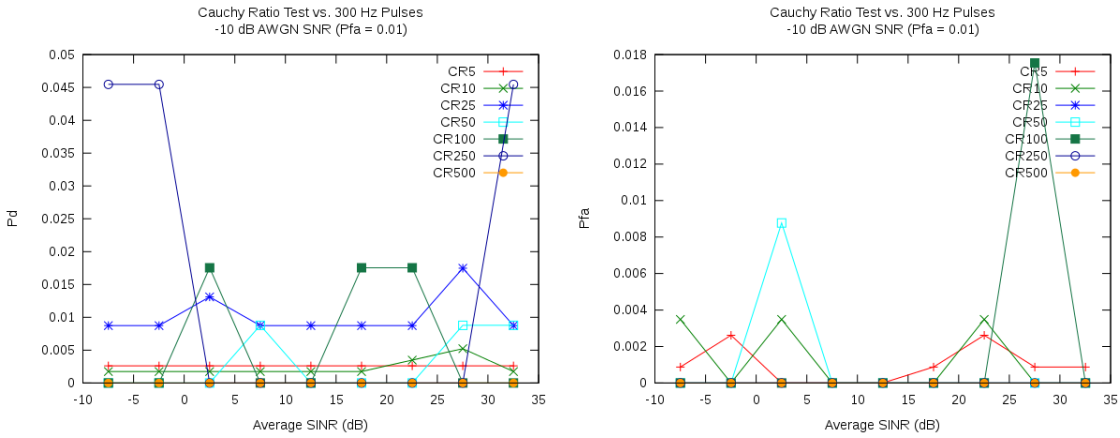

(a) P_d **(b)** P_{fa}

Figure A.4: *CRT vs. 300Hz Pulses with 1% False Alarm Rate, -10 dB AWGN SNR*

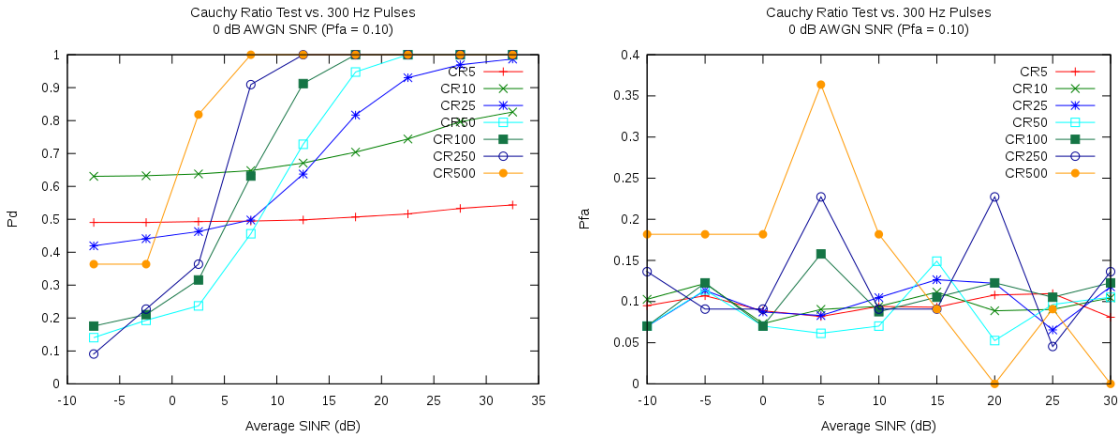

(a) P_d **(b)** P_{fa}

Figure A.5: *CRT vs. 300Hz Pulses with 10% False Alarm Rate, 0 dB AWGN SNR*

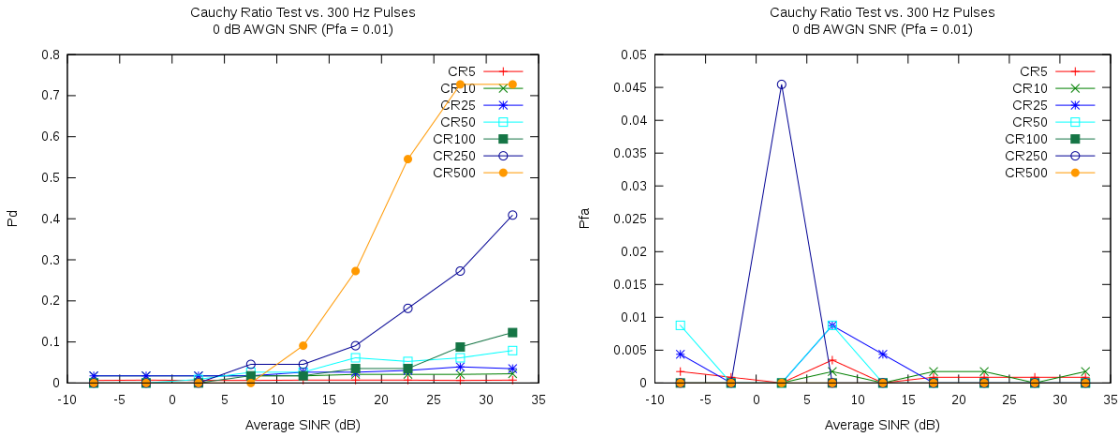

(a) P_d **(b)** P_{fa}

Figure A.6: *CRT vs. 300Hz Pulses with 1% False Alarm Rate, 0 dB AWGN SNR*

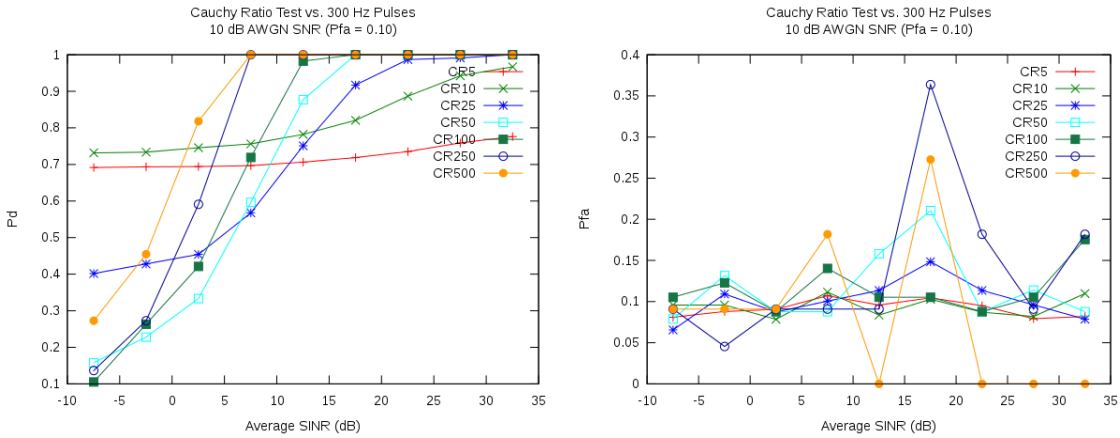

(a) P_d **(b)** P_{fa}

Figure A.7: *CRT vs. 300Hz Pulses with 10% False Alarm Rate, 10 dB AWGN SNR*

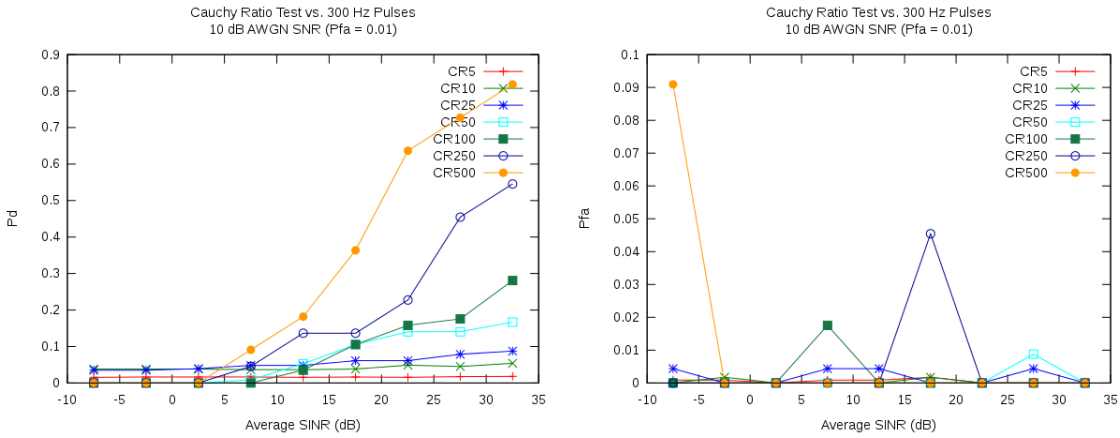

(a) P_d **(b)** P_{fa}

Figure A.8: *CRT vs. 300Hz Pulses with 1% False Alarm Rate, 10 dB AWGN SNR*

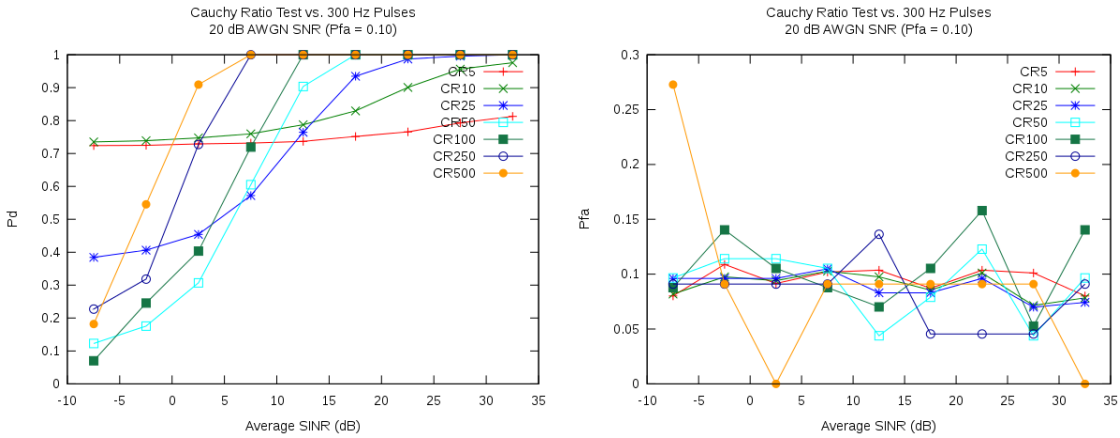

(a) P_d **(b)** P_{fa}

Figure A.9: *CRT vs. 300Hz Pulses with 10% False Alarm Rate, 20 dB AWGN SNR*

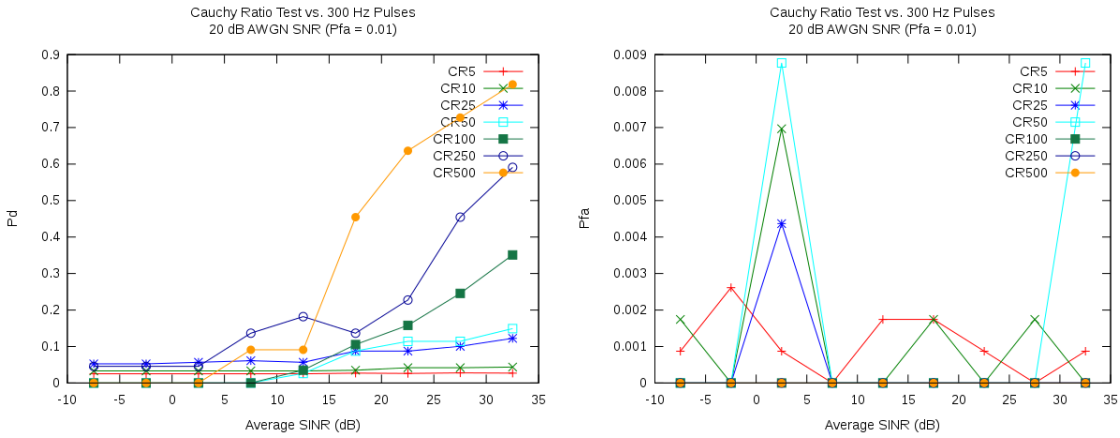

(a) P_d **(b)** P_{fa}

Figure A.10: *CRT vs. 300Hz Pulses with 1% False Alarm Rate, 20 dB AWGN SNR*

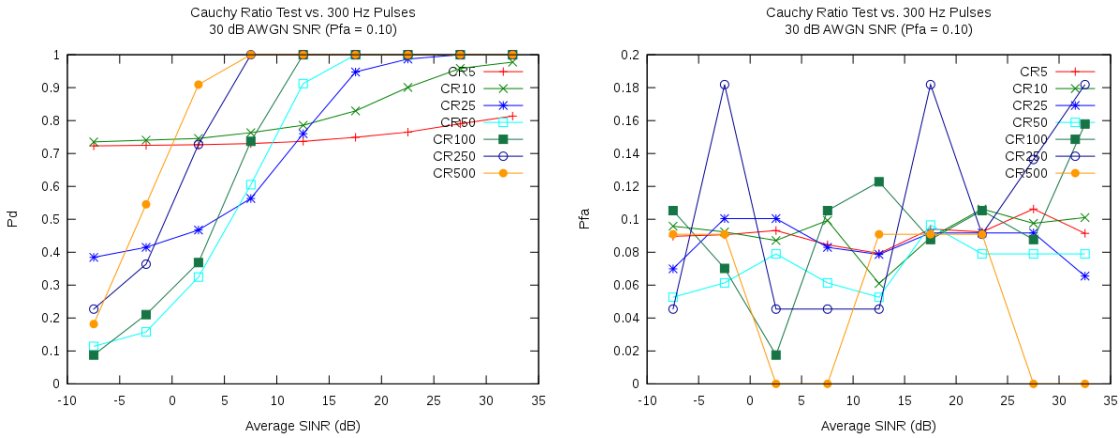

(a) P_d **(b)** P_{fa}

Figure A.11: *CRT vs. 300Hz Pulses with 10% False Alarm Rate, 30 dB AWGN SNR*

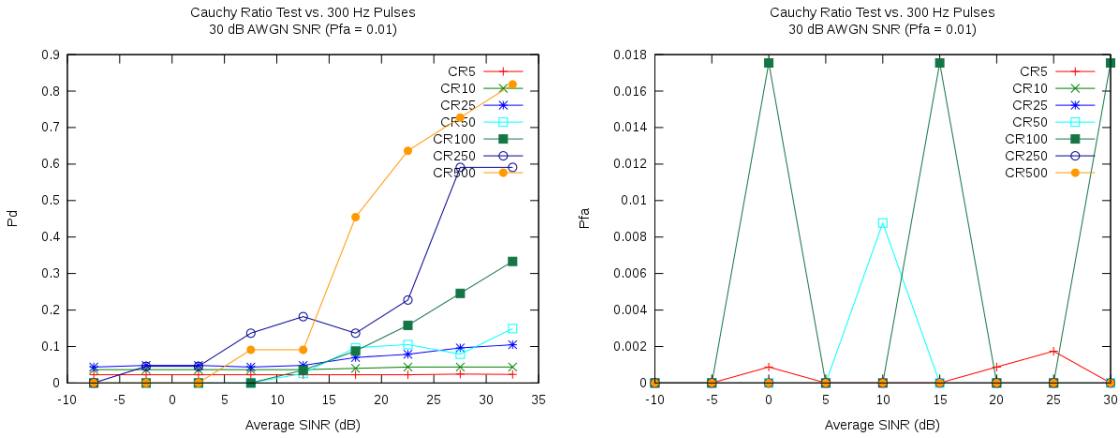

(a) P_d **(b)** P_{fa}

Figure A.12: *CRT vs. 300Hz Pulses with 1% False Alarm Rate, 30 dB AWGN SNR*

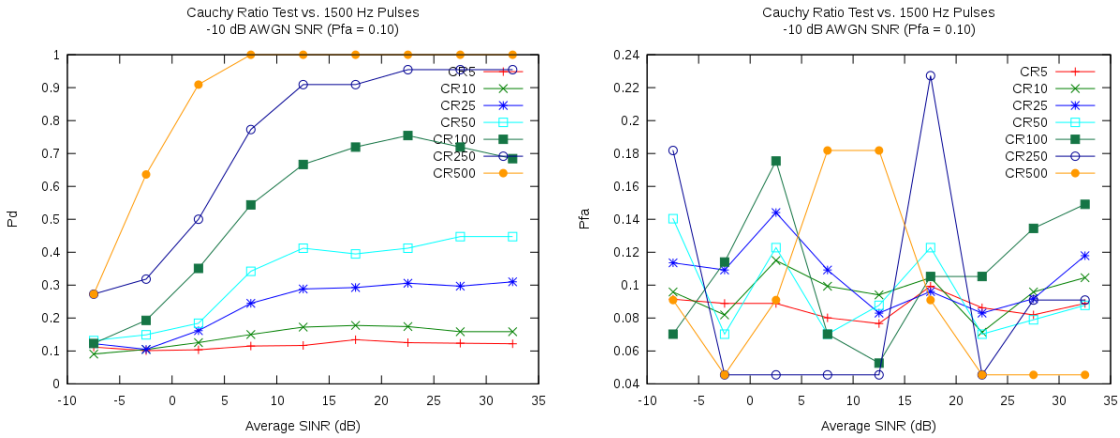

(a) P_d **(b)** P_{fa}

Figure A.13: *CRT vs. 1500Hz Pulses with 10% False Alarm Rate, -10 dB AWGN SNR*

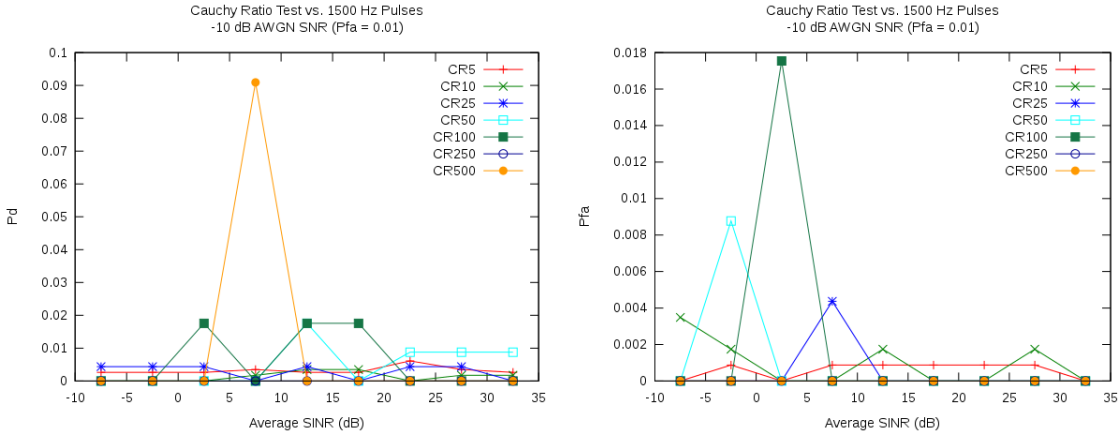

(a) P_d **(b)** P_{fa}

Figure A.14: *CRT vs. 1500Hz Pulses with 1% False Alarm Rate, -10 dB AWGN SNR*

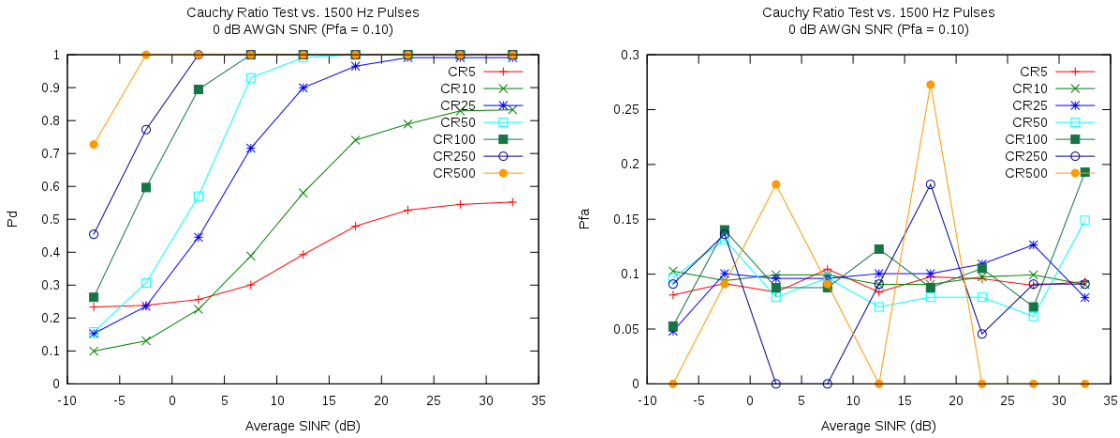

(a) P_d **(b)** P_{fa}

Figure A.15: *CRT vs. 1500Hz Pulses with 10% False Alarm Rate, 0 dB AWGN SNR*

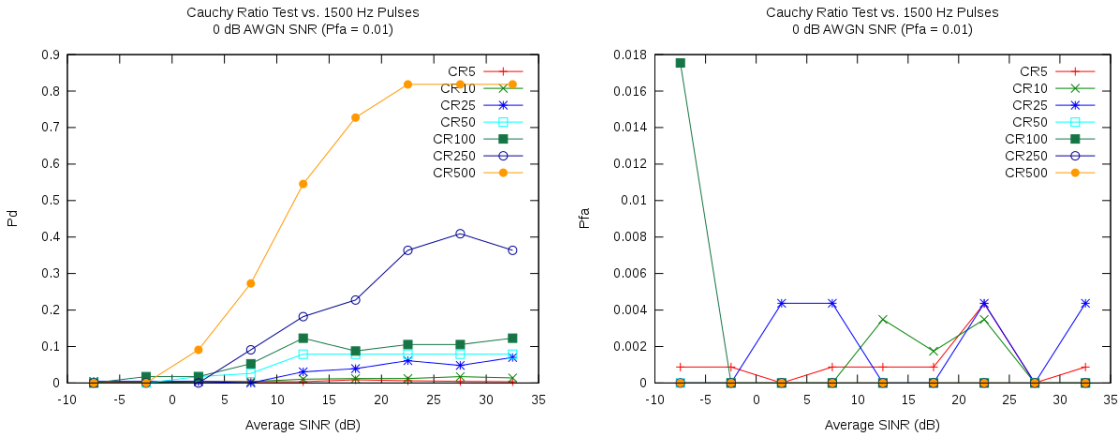

(a) P_d **(b)** P_{fa}

Figure A.16: *CRT vs. 1500Hz Pulses with 1% False Alarm Rate, 0 dB AWGN SNR*

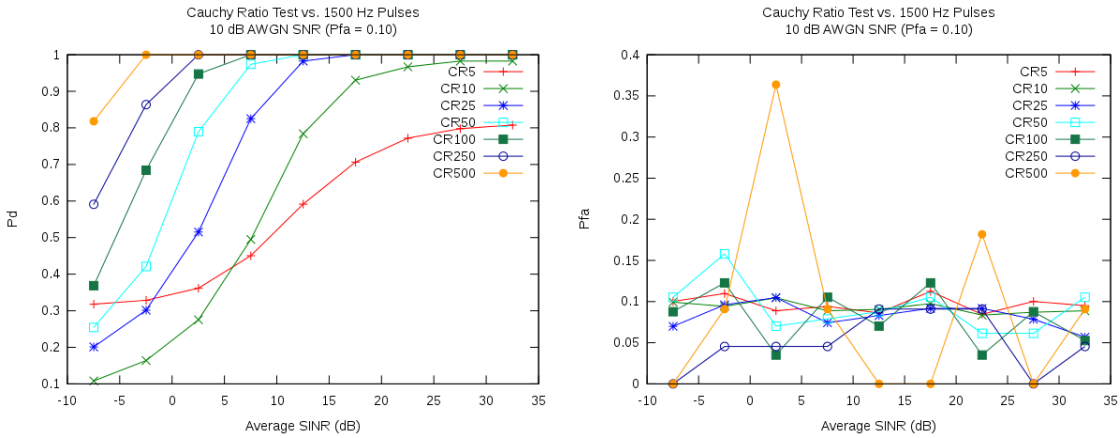

(a) P_d **(b)** P_{fa}

Figure A.17: *CRT vs. 1500Hz Pulses with 10% False Alarm Rate, 10 dB AWGN SNR*

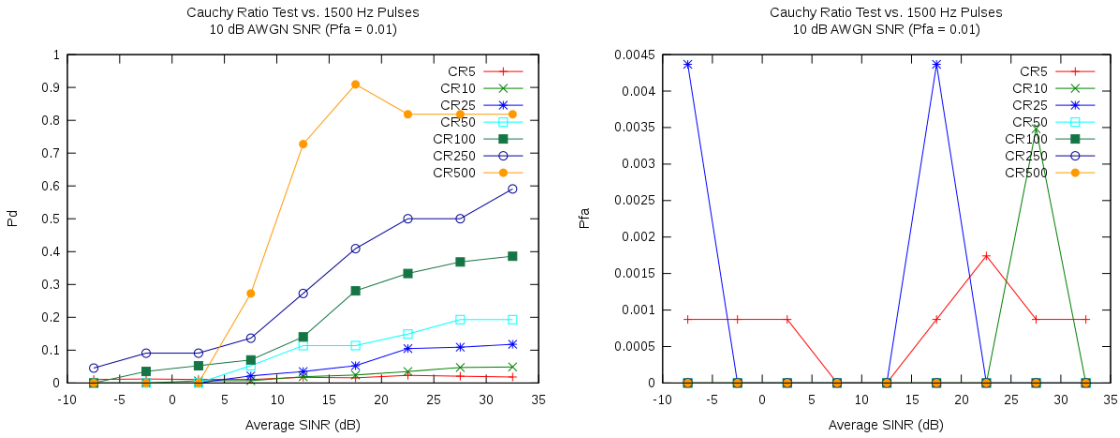

(a) P_d **(b)** P_{fa}

Figure A.18: *CRT vs. 1500Hz Pulses with 1% False Alarm Rate, 10 dB AWGN SNR*

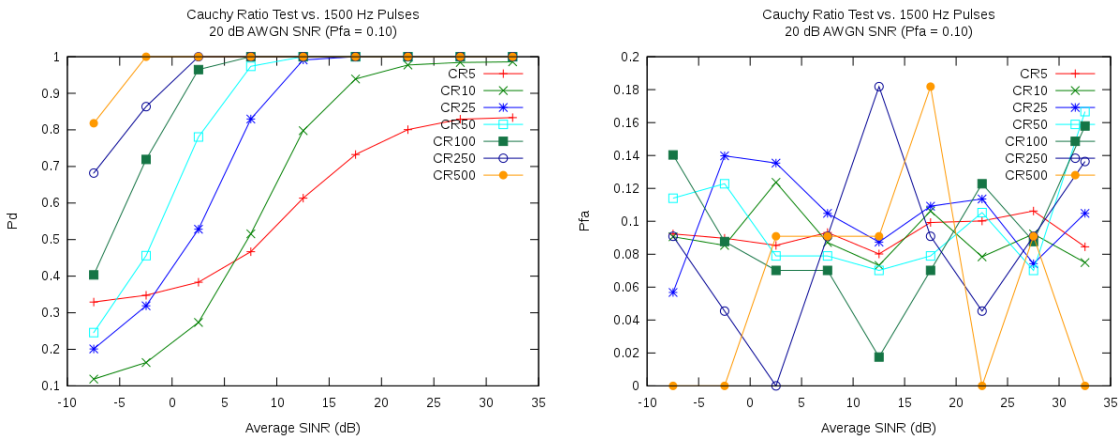

(a) P_d **(b)** P_{fa}

Figure A.19: *CRT vs. 1500Hz Pulses with 10% False Alarm Rate, 20 dB AWGN SNR*

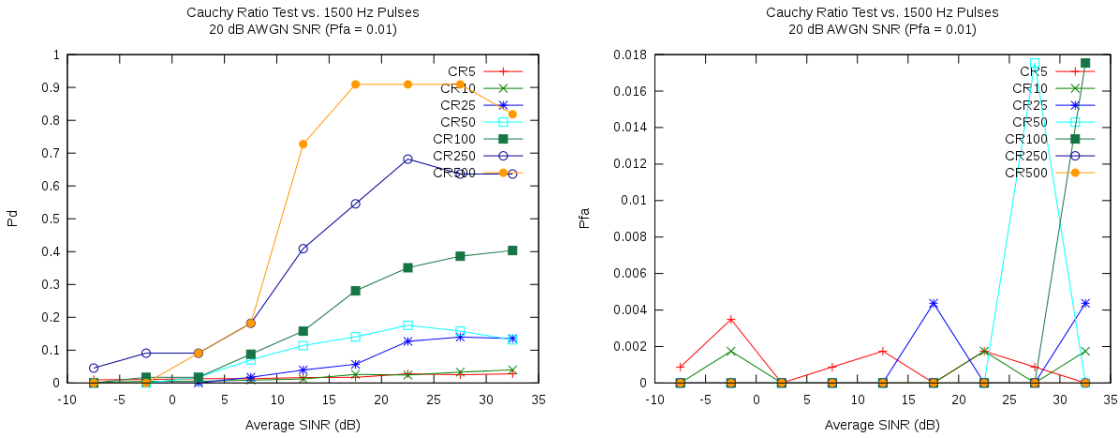

(a) P_d **(b)** P_{fa}

Figure A.20: *CRT vs. 1500Hz Pulses with 1% False Alarm Rate, 20 dB AWGN SNR*

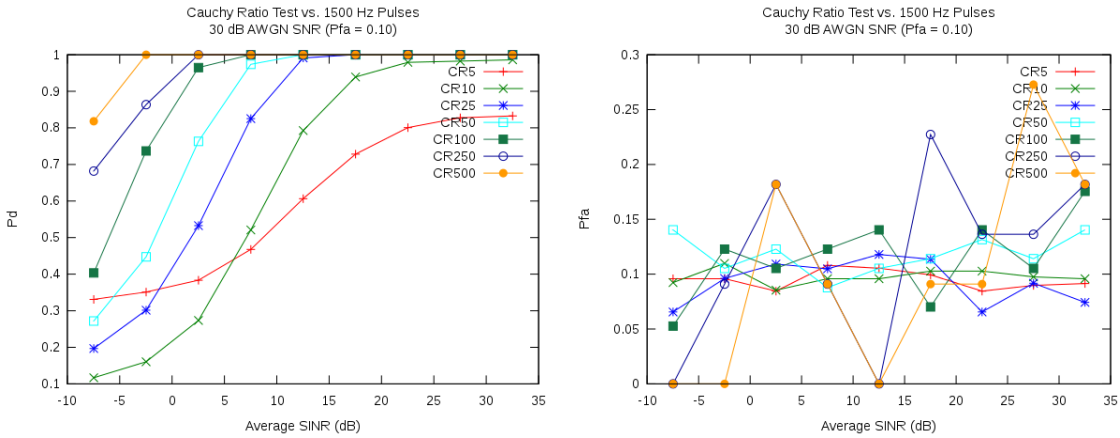

(a) P_d **(b)** P_{fa}

Figure A.21: *CRT vs. 1500Hz Pulses with 10% False Alarm Rate, 30 dB AWGN SNR*

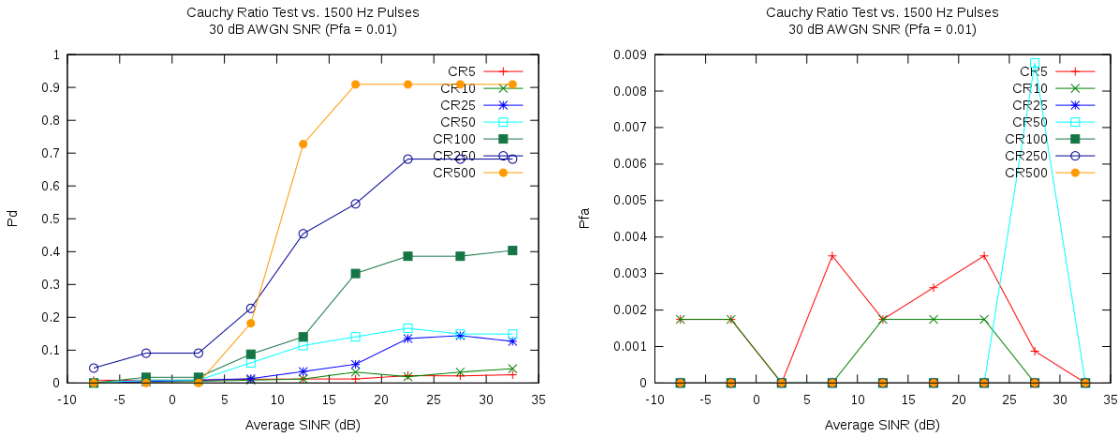

(a) P_d **(b)** P_{fa}

Figure A.22: *CRT vs. 1500Hz Pulses with 1% False Alarm Rate, 30 dB AWGN SNR*

A.2 General Likelihood Ratio Test - Single CF

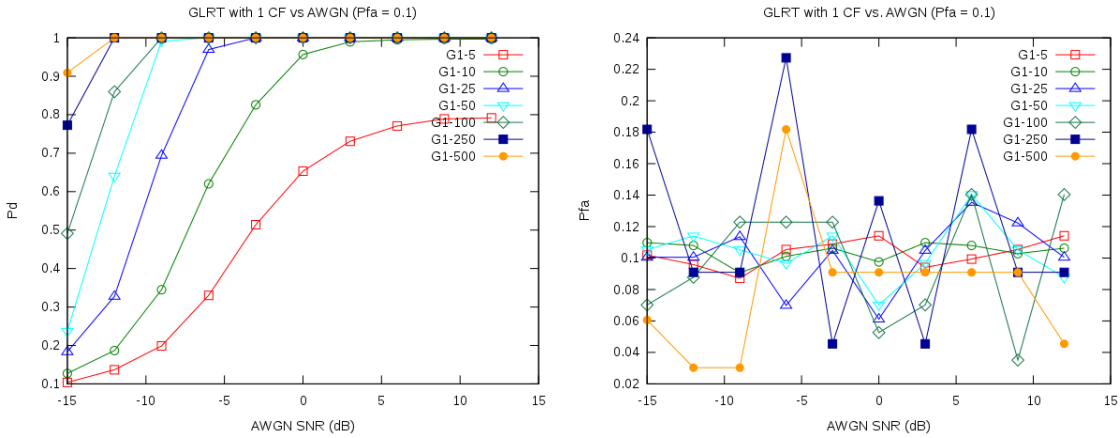

(a) P_d **(b)** P_{fa}

Figure A.23: *GLRT 1 CF vs. AWGN with 10% False Alarm Rate*

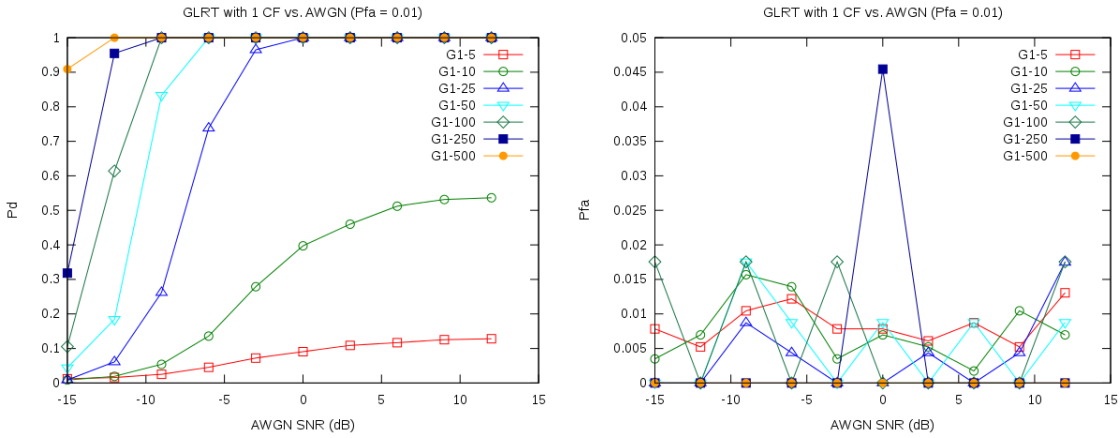

(a) P_d **(b)** P_{fa}

Figure A.24: *GLRT 1 CF vs. AWGN with 1% False Alarm Rate*

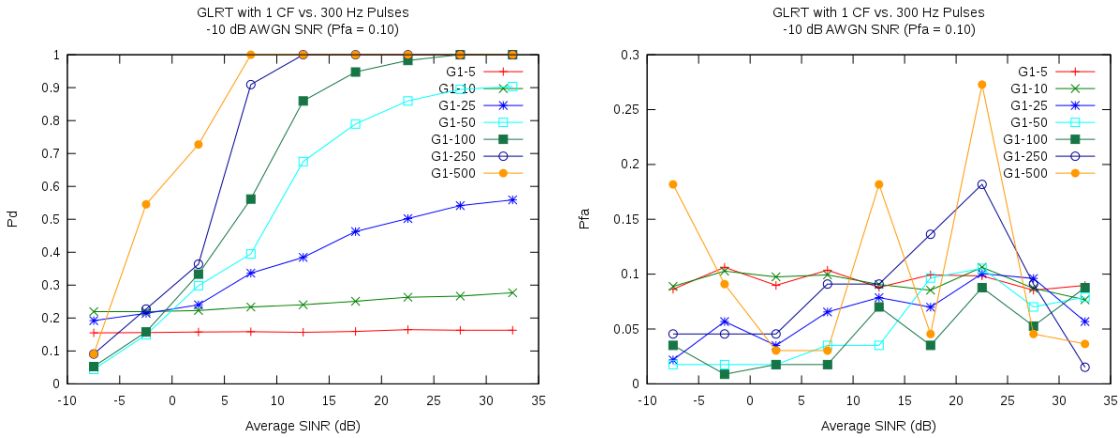

(a) P_d **(b)** P_{fa}

Figure A.25: *GLRT 1 CF vs. 300Hz Pulses with 10% False Alarm Rate, -10 dB AWGN SNR*

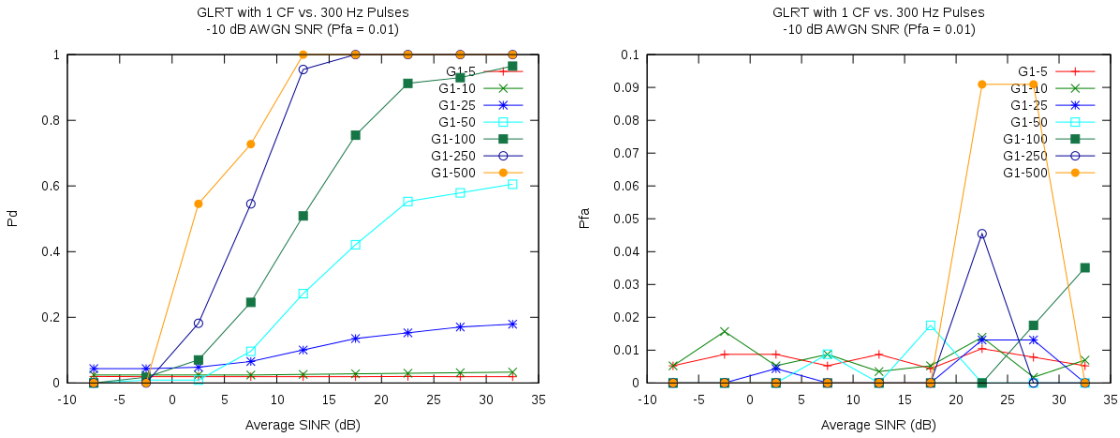

(a) P_d **(b)** P_{fa}

Figure A.26: *GLRT 1 CF vs. 300Hz Pulses with 1% False Alarm Rate, -10 dB AWGN SNR*

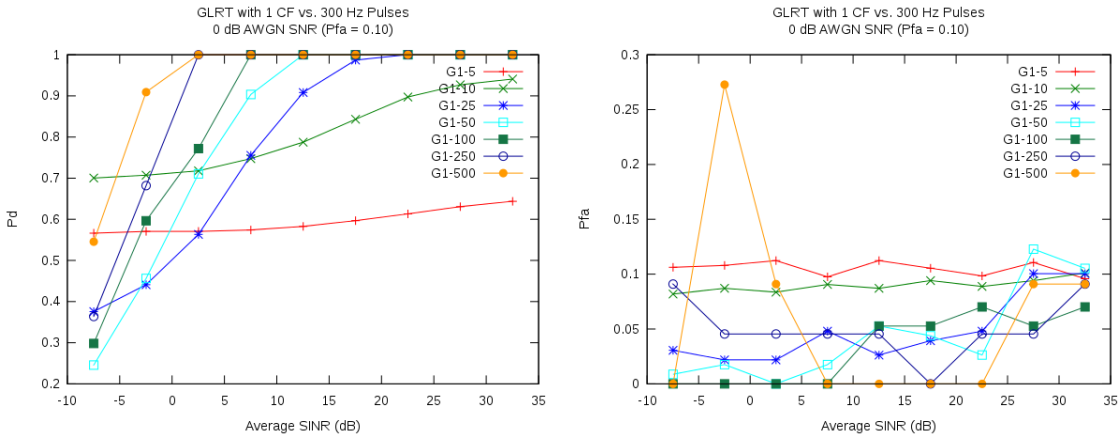

(a) P_d **(b)** P_{fa}

Figure A.27: *GLRT 1 CF vs. 300Hz Pulses with 10% False Alarm Rate, 0 dB AWGN SNR*

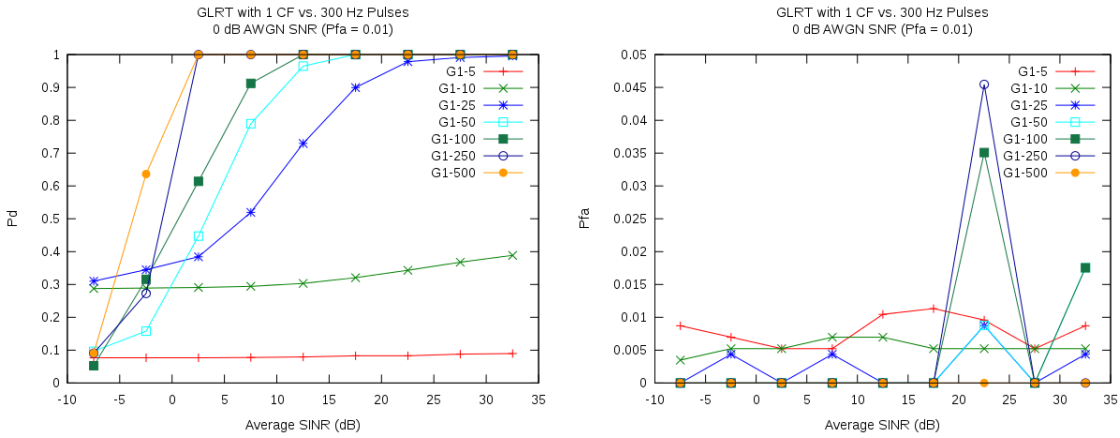

(a) P_d **(b)** P_{fa}

Figure A.28: *GLRT 1 CF vs. 300Hz Pulses with 1% False Alarm Rate, 0 dB AWGN SNR*

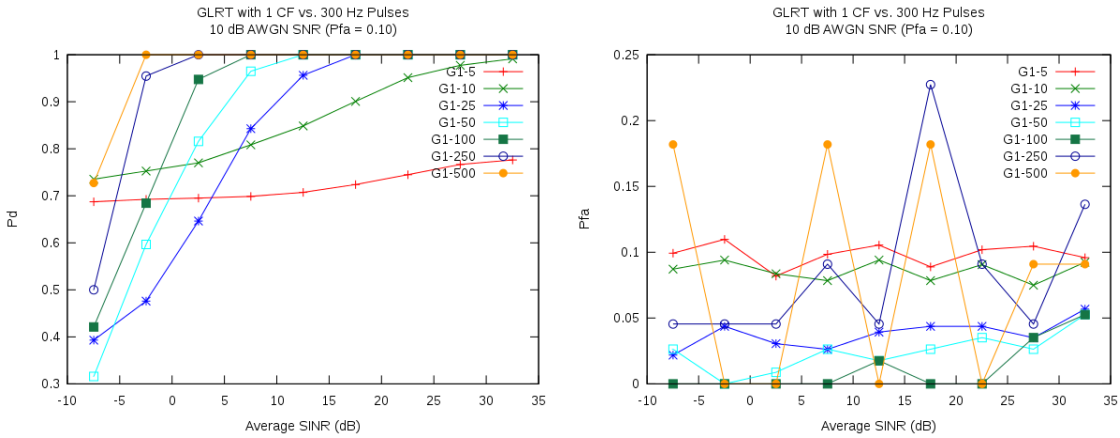

(a) P_d **(b)** P_{fa}

Figure A.29: *GLRT 1 CF vs. 300Hz Pulses with 10% False Alarm Rate, 10 dB AWGN SNR*

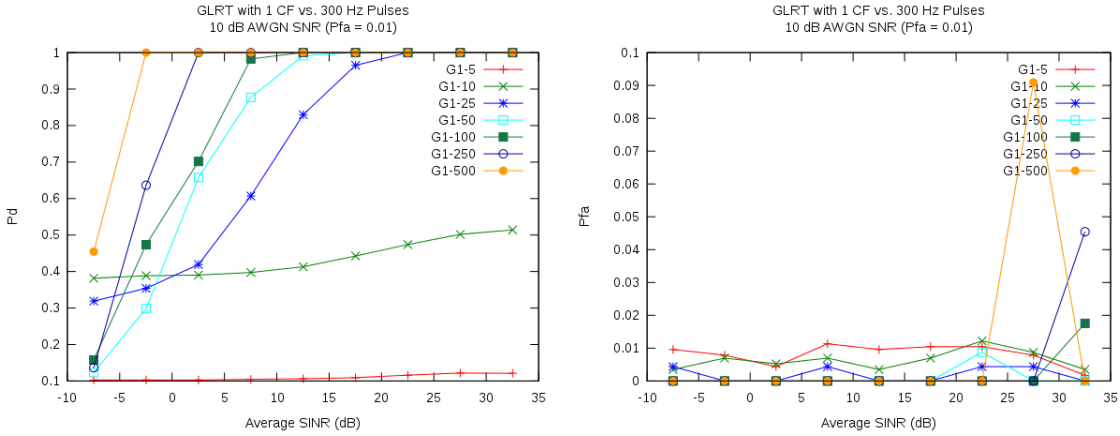

(a) P_d **(b)** P_{fa}

Figure A.30: *GLRT 1 CF vs. 300Hz Pulses with 1% False Alarm Rate, 10 dB AWGN SNR*

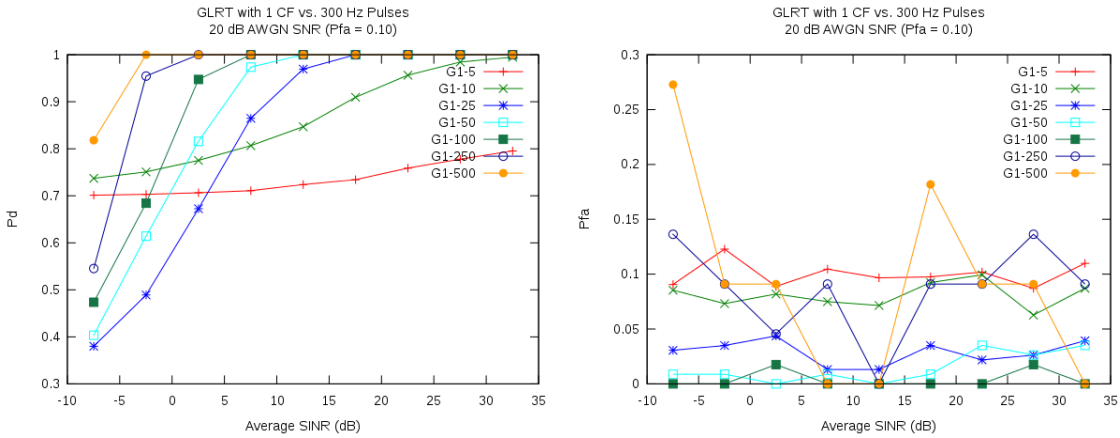

(a) P_d **(b)** P_{fa}

Figure A.31: *GLRT 1 CF vs. 300Hz Pulses with 10% False Alarm Rate, 20 dB AWGN SNR*

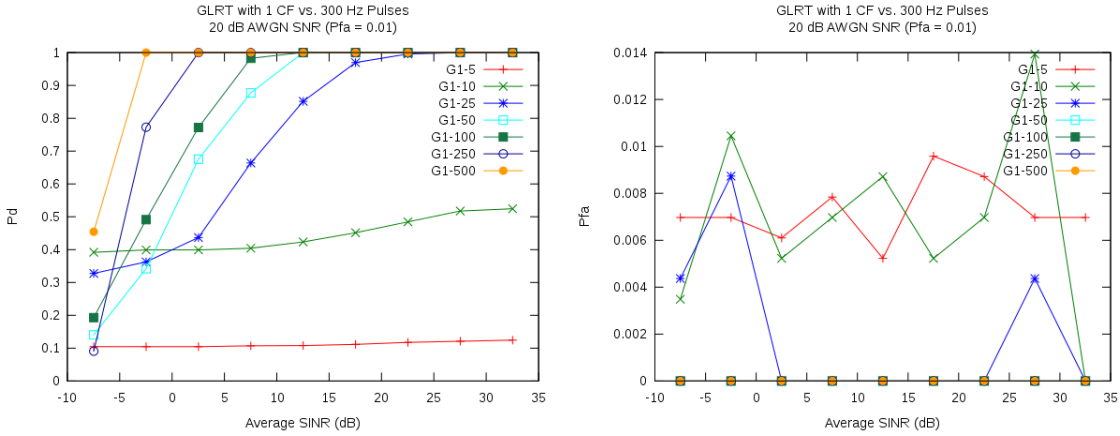

(a) P_d **(b)** P_{fa}

Figure A.32: *GLRT 1 CF vs. 300Hz Pulses with 1% False Alarm Rate, 20 dB AWGN SNR*

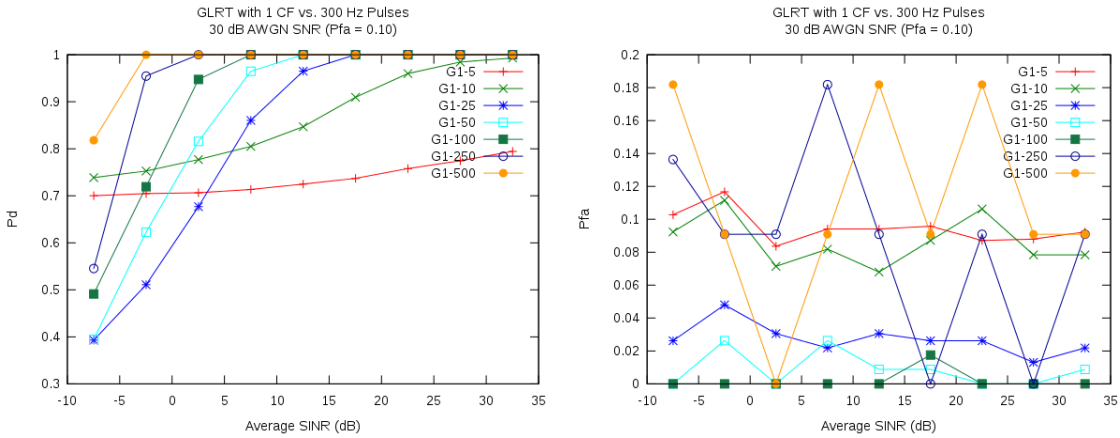

(a) P_d **(b)** P_{fa}

Figure A.33: *GLRT 1 CF vs. 300Hz Pulses with 10% False Alarm Rate, 30 dB AWGN SNR*

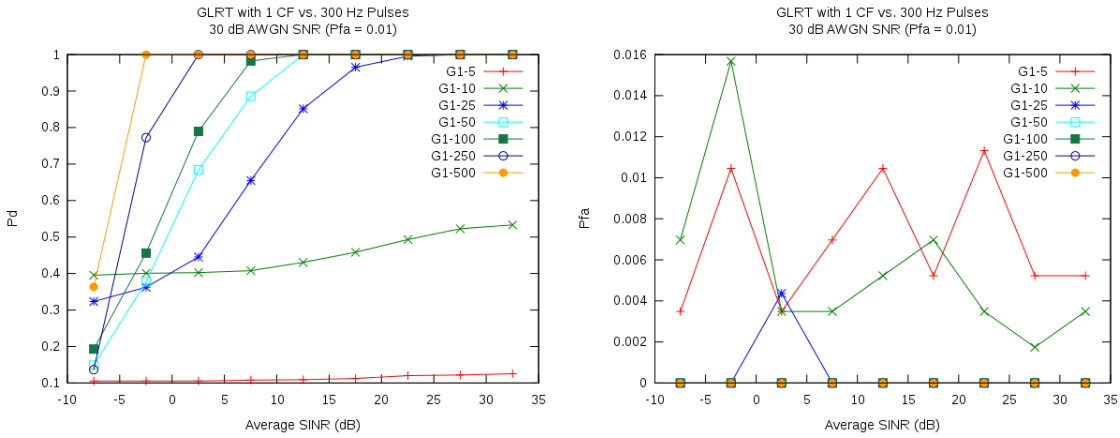

(a) P_d **(b)** P_{fa}

Figure A.34: *GLRT 1 CF vs. 300Hz Pulses with 1% False Alarm Rate, 30 dB AWGN SNR*

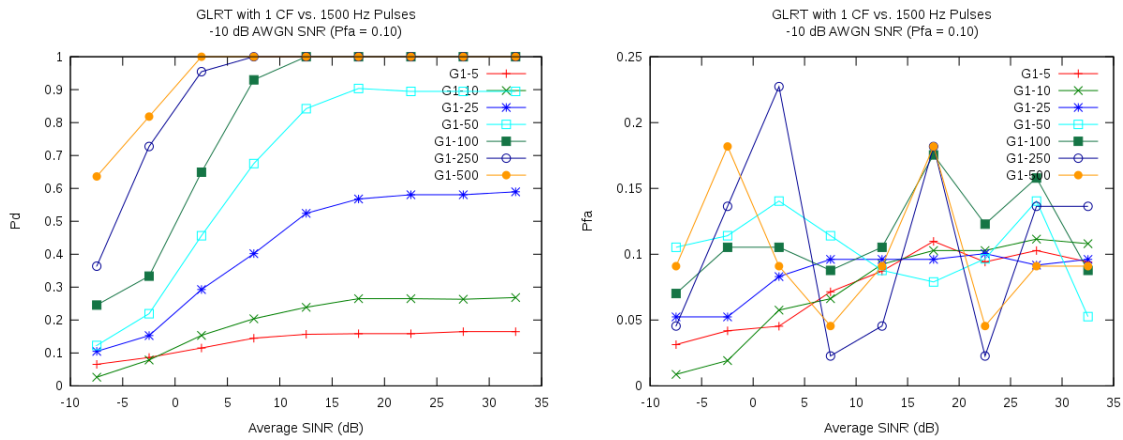

(a) P_d **(b)** P_{fa}

Figure A.35: *GLRT 1 CF vs. 1500Hz Pulses with 10% False Alarm Rate, -10 dB AWGN SNR*

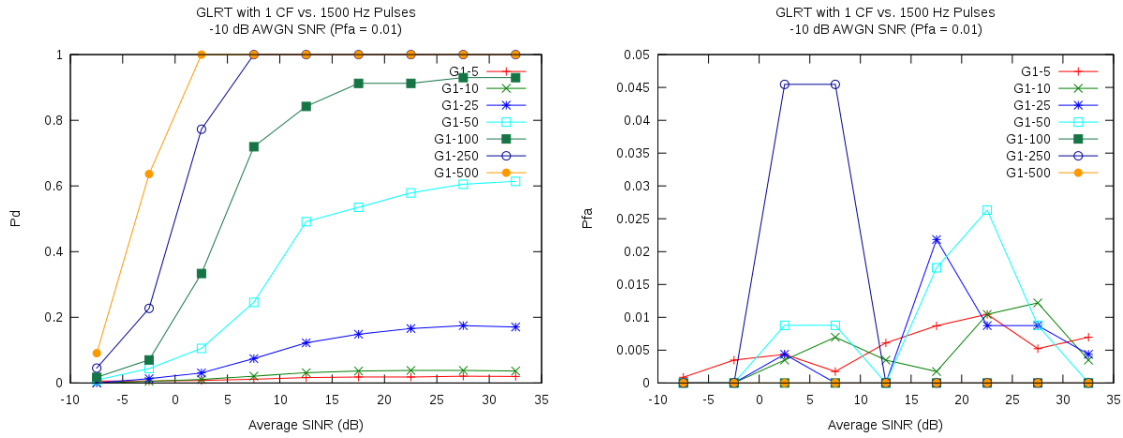

(a) P_d **(b)** P_{fa}

Figure A.36: *GLRT 1 CF vs. 1500Hz Pulses with 1% False Alarm Rate, -10 dB AWGN SNR*

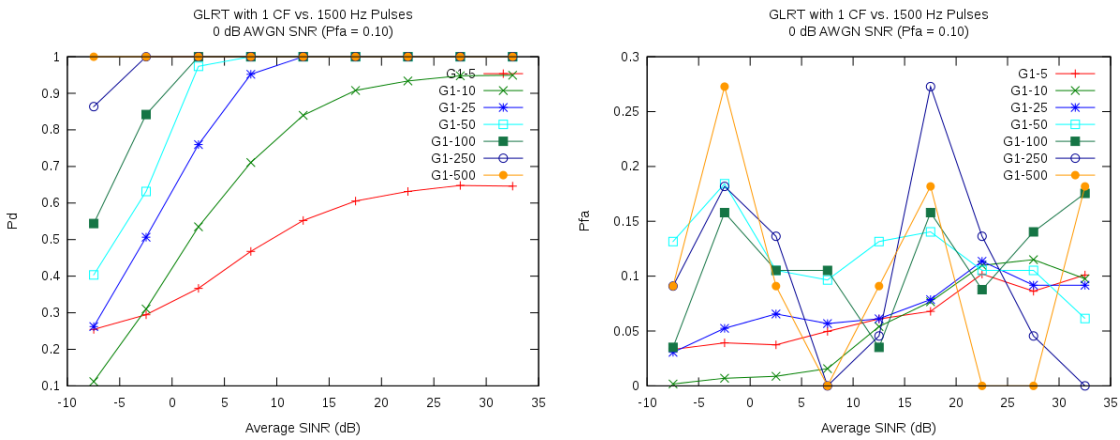

(a) P_d **(b)** P_{fa}

Figure A.37: *GLRT 1 CF vs. 1500Hz Pulses with 10% False Alarm Rate, 0 dB AWGN SNR*

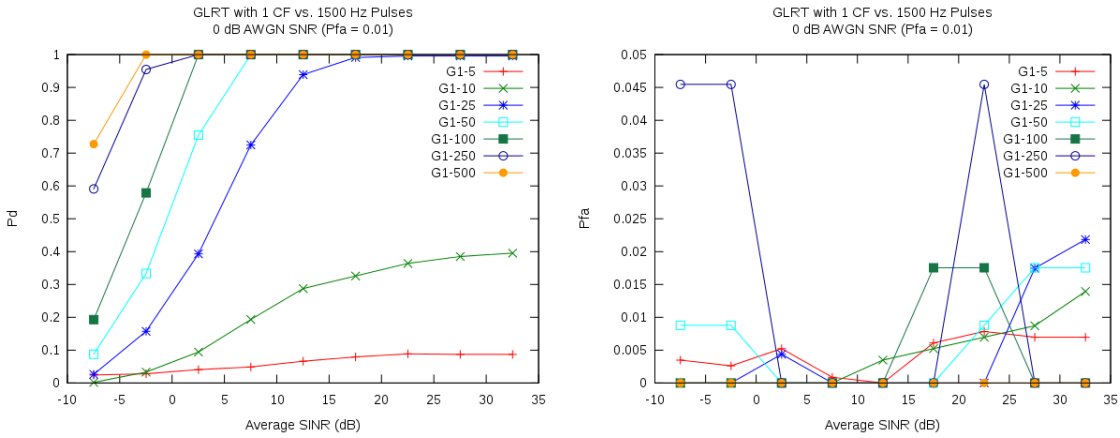

(a) P_d **(b)** P_{fa}

Figure A.38: *GLRT 1 CF vs. 1500Hz Pulses with 1% False Alarm Rate, 0 dB AWGN SNR*

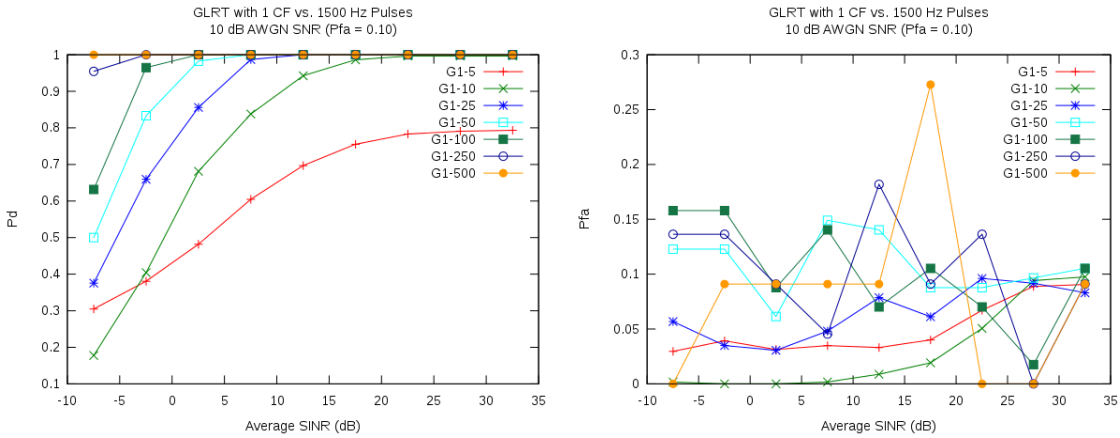

(a) P_d **(b)** P_{fa}

Figure A.39: *GLRT 1 CF vs. 1500Hz Pulses with 10% False Alarm Rate, 10 dB AWGN SNR*

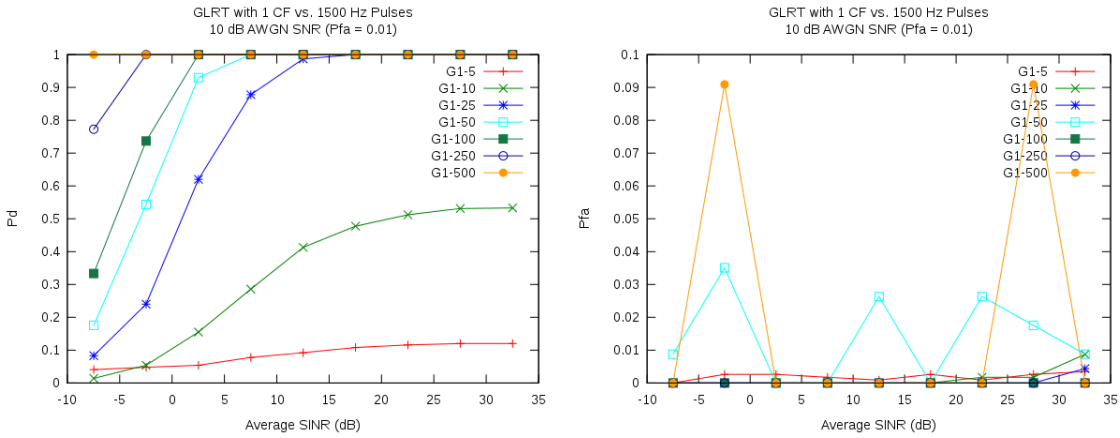

(a) P_d **(b)** P_{fa}

Figure A.40: *GLRT 1 CF vs. 1500Hz Pulses with 1% False Alarm Rate, 10 dB AWGN SNR*

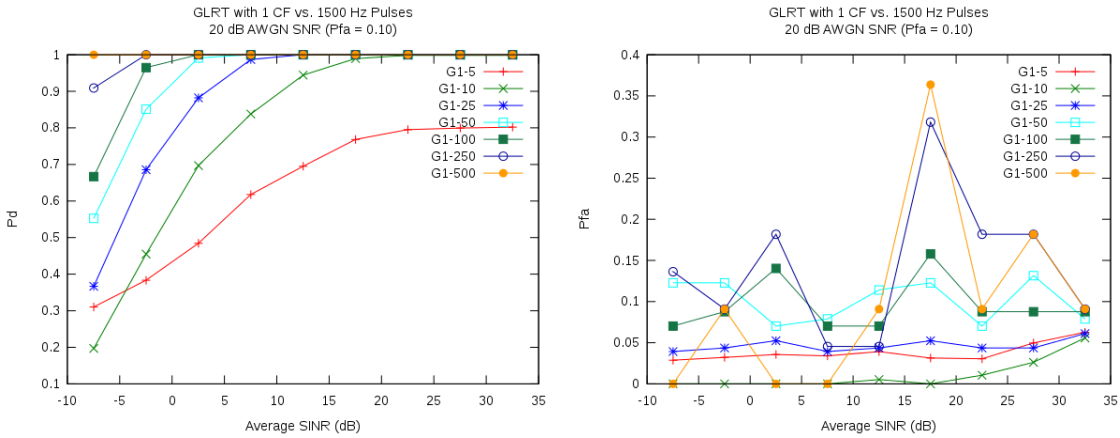

(a) P_d **(b)** P_{fa}

Figure A.41: *GLRT 1 CF vs. 1500Hz Pulses with 10% False Alarm Rate, 20 dB AWGN SNR*

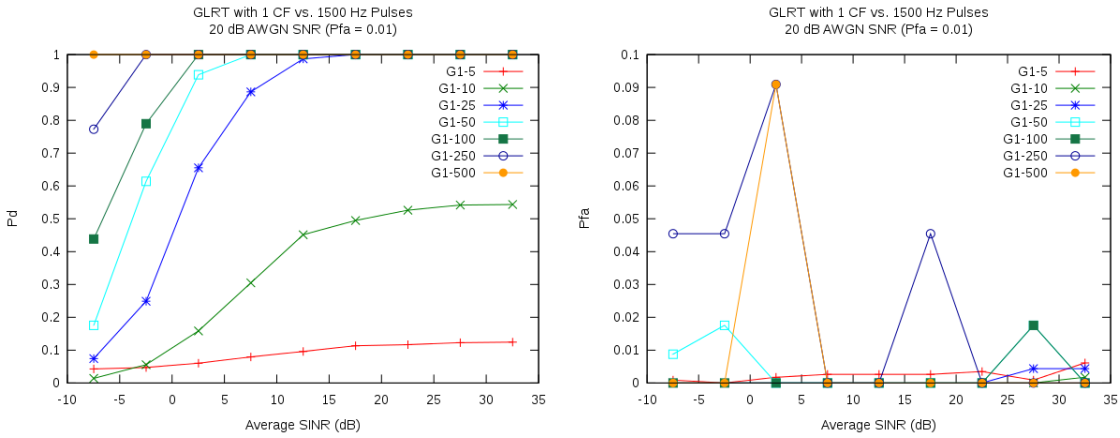

(a) P_d **(b)** P_{fa}

Figure A.42: *GLRT 1 CF vs. 1500Hz Pulses with 1% False Alarm Rate, 20 dB AWGN SNR*

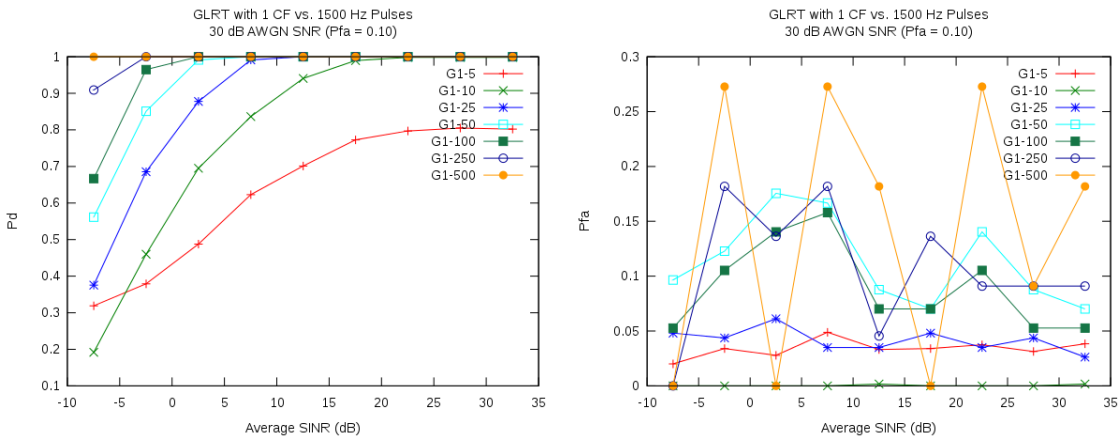

(a) P_d **(b)** P_{fa}

Figure A.43: *GLRT 1 CF vs. 1500Hz Pulses with 10% False Alarm Rate, 30 dB AWGN SNR*

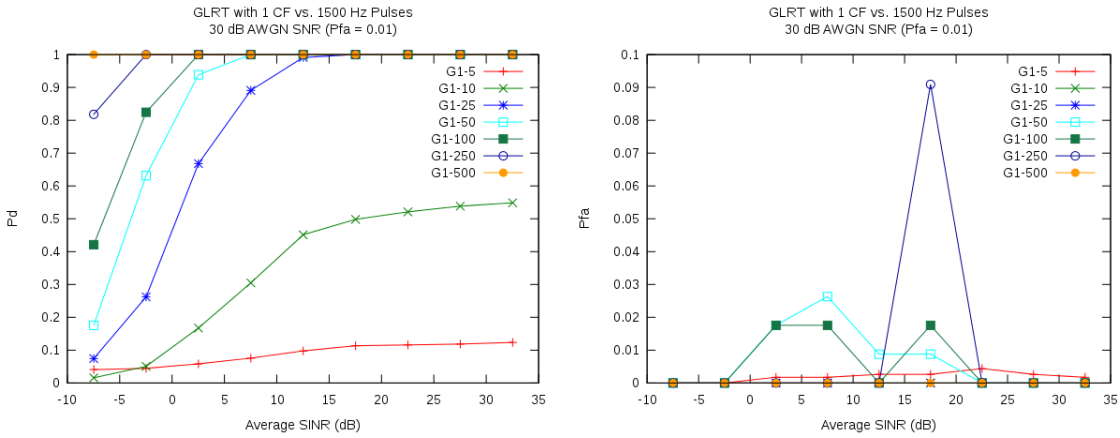

(a) P_d **(b)** P_{fa}

Figure A.44: *GLRT 1 CF vs. 1500Hz Pulses with 1% False Alarm Rate, 30 dB AWGN SNR*

A.3 General Likelihood Ratio Test - Two CFs

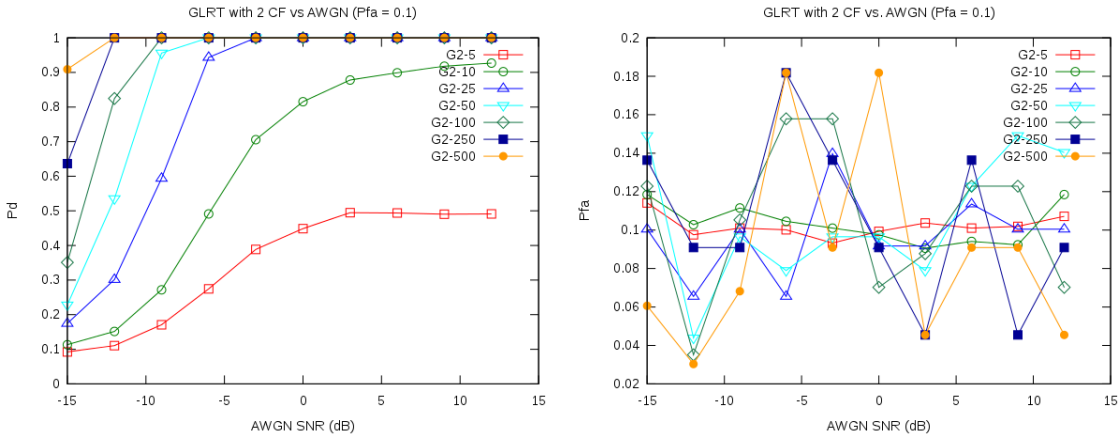

(a) P_d **(b)** P_{fa}

Figure A.45: *GLRT 2 CF vs. AWGN with 10% False Alarm Rate*

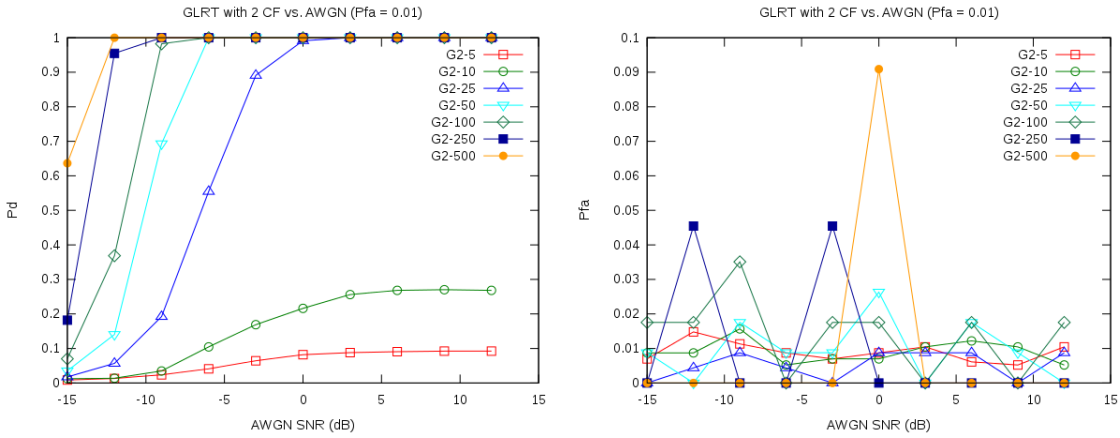

(a) P_d **(b)** P_{fa}

Figure A.46: *GLRT 2 CF vs. AWGN with 1% False Alarm Rate*

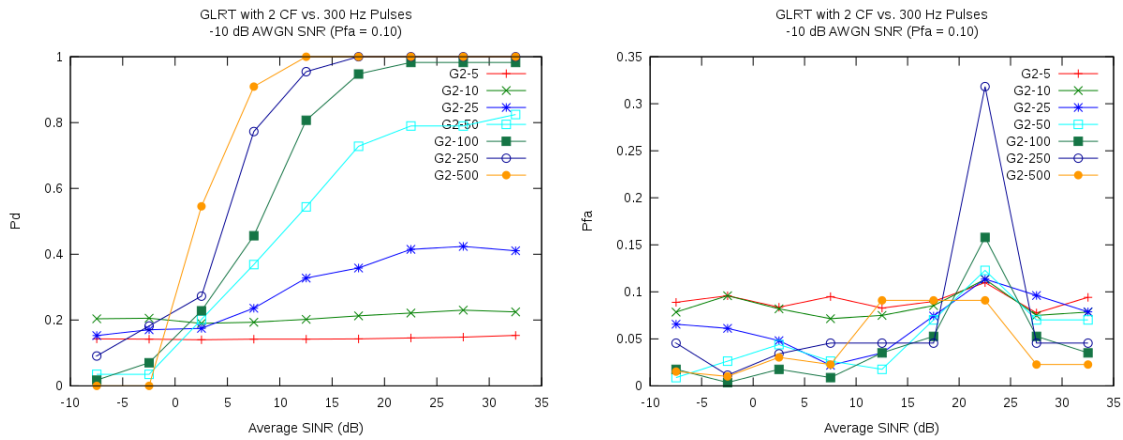

(a) P_d **(b)** P_{fa}

Figure A.47: *GLRT 2 CF vs. 300Hz Pulses with 10% False Alarm Rate, -10 dB AWGN SNR*

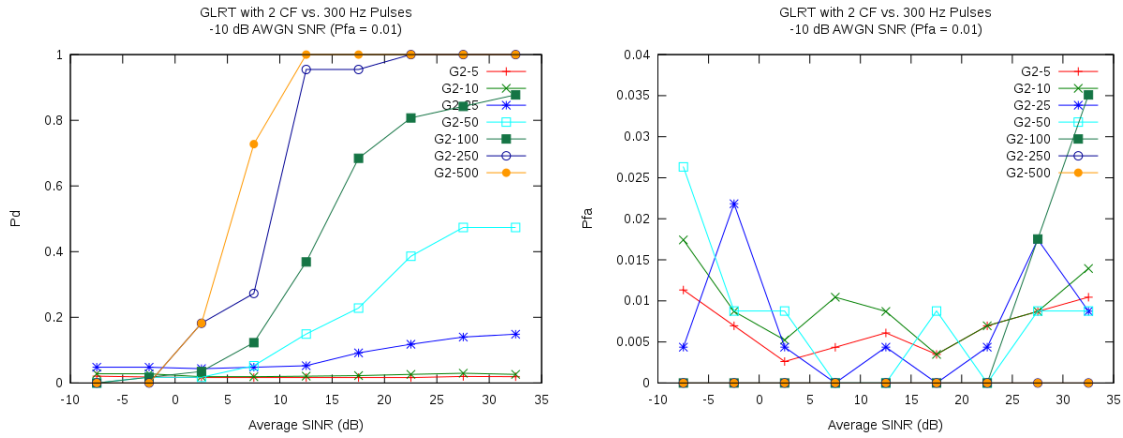

(a) P_d **(b)** P_{fa}

Figure A.48: *GLRT 2 CF vs. 300Hz Pulses with 1% False Alarm Rate, -10 dB AWGN SNR*

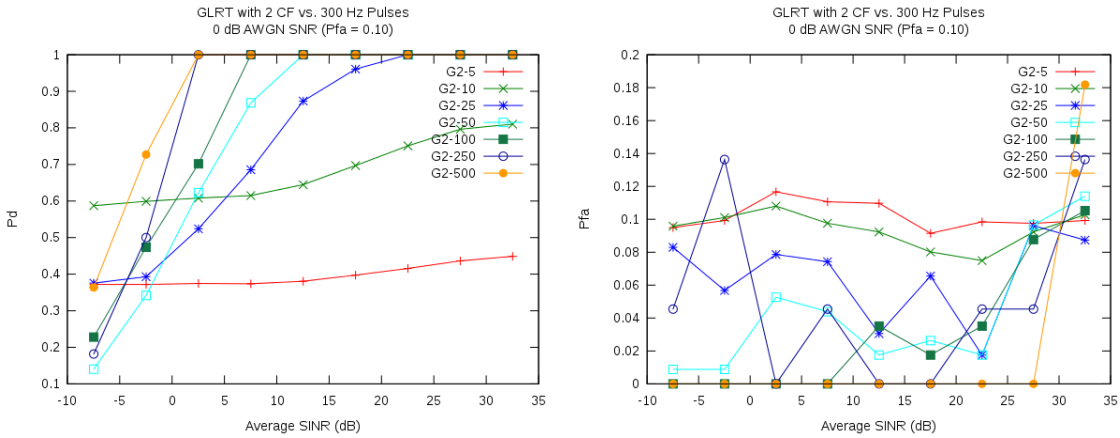

(a) P_d **(b)** P_{fa}

Figure A.49: *GLRT 2 CF vs. 300Hz Pulses with 10% False Alarm Rate, 0 dB AWGN SNR*

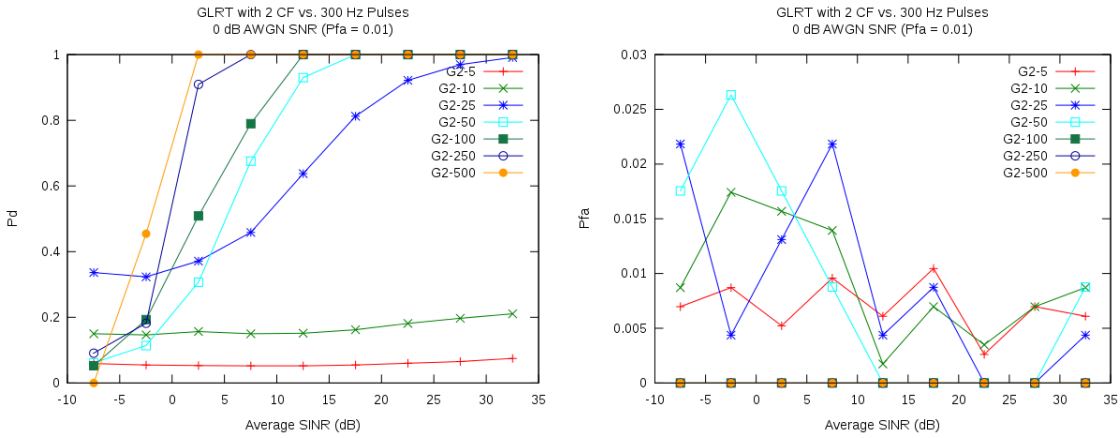

(a) P_d **(b)** P_{fa}

Figure A.50: *GLRT 2 CF vs. 300Hz Pulses with 1% False Alarm Rate, 0 dB AWGN SNR*

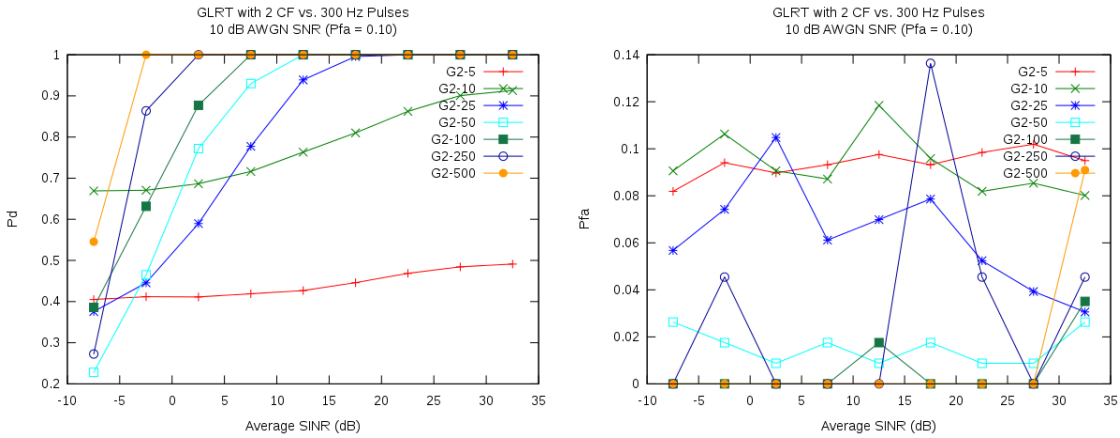

(a) P_d **(b)** P_{fa}

Figure A.51: *GLRT 2 CF vs. 300Hz Pulses with 10% False Alarm Rate, 10 dB AWGN SNR*

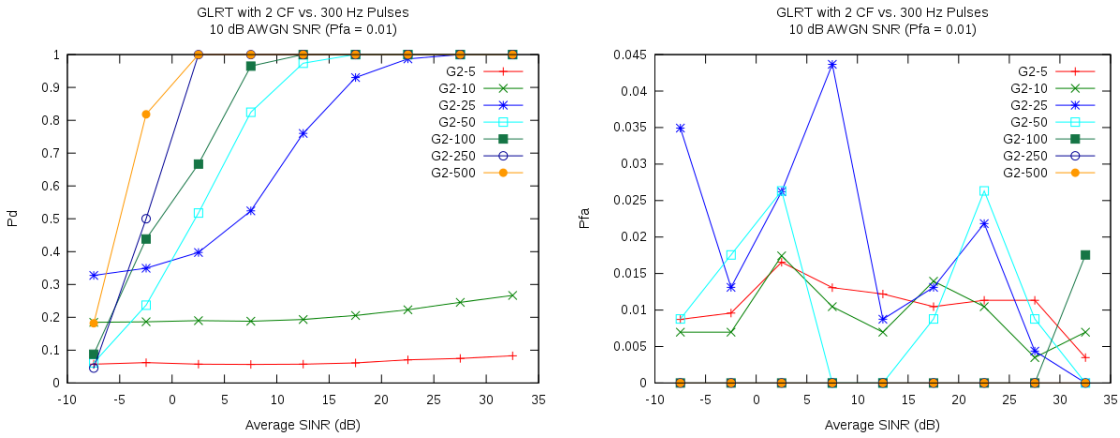

(a) P_d **(b)** P_{fa}

Figure A.52: *GLRT 2 CF vs. 300Hz Pulses with 1% False Alarm Rate, 10 dB AWGN SNR*

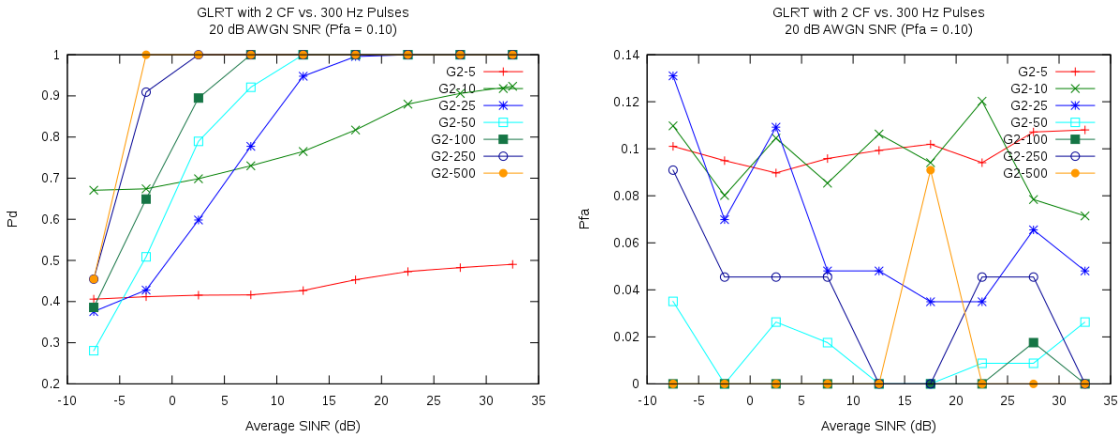

(a) P_d **(b)** P_{fa}

Figure A.53: *GLRT 2 CF vs. 300Hz Pulses with 10% False Alarm Rate, 20 dB AWGN SNR*

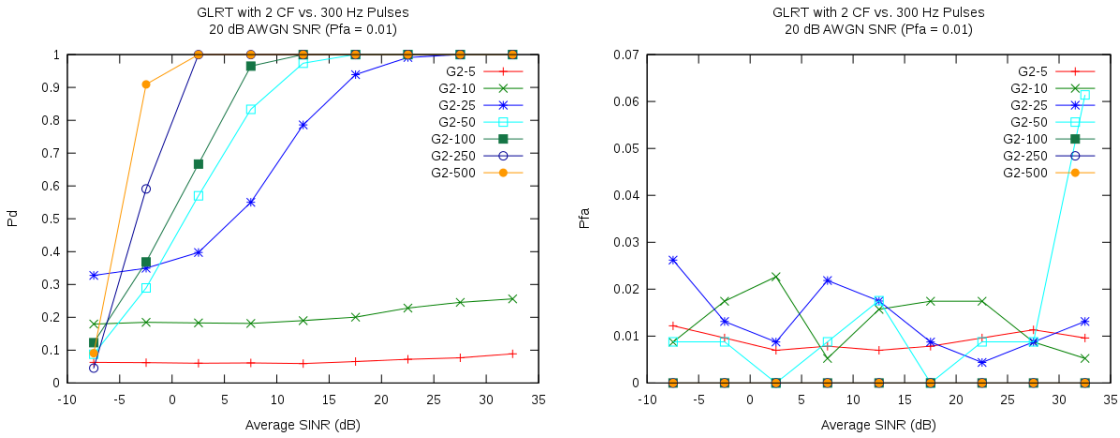

(a) P_d **(b)** P_{fa}

Figure A.54: *GLRT 2 CF vs. 300Hz Pulses with 1% False Alarm Rate, 20 dB AWGN SNR*

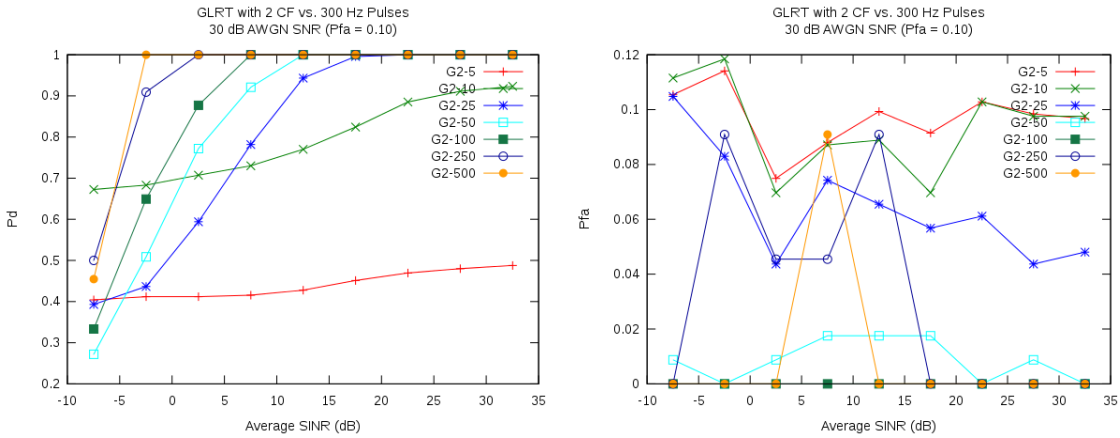

(a) P_d **(b)** P_{fa}

Figure A.55: *GLRT 2 CF vs. 300Hz Pulses with 10% False Alarm Rate, 30 dB AWGN SNR*

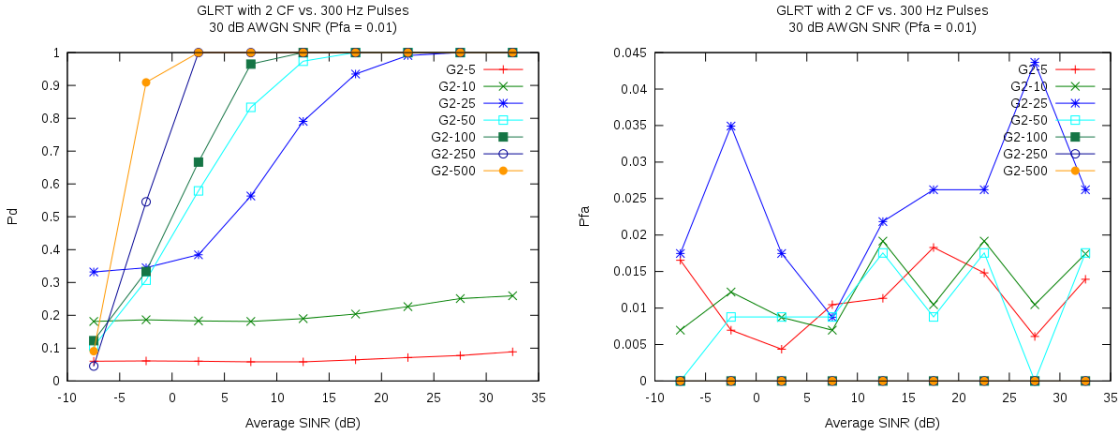

(a) P_d **(b)** P_{fa}

Figure A.56: *GLRT 2 CF vs. 300Hz Pulses with 1% False Alarm Rate, 30 dB AWGN SNR*

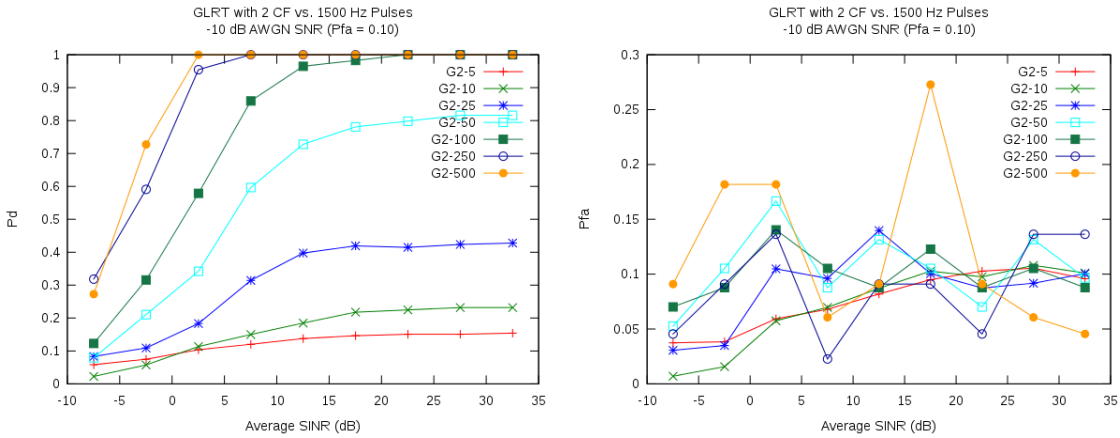

(a) P_d **(b)** P_{fa}

Figure A.57: *GLRT 2 CF vs. 1500Hz Pulses with 10% False Alarm Rate, -10 dB AWGN SNR*

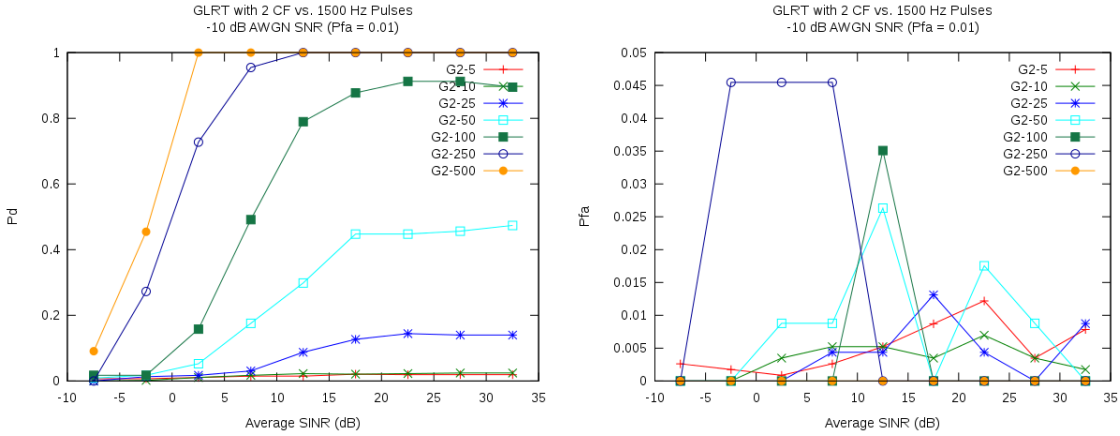

(a) P_d **(b)** P_{fa}

Figure A.58: *GLRT 2 CF vs. 1500Hz Pulses with 1% False Alarm Rate, -10 dB AWGN SNR*

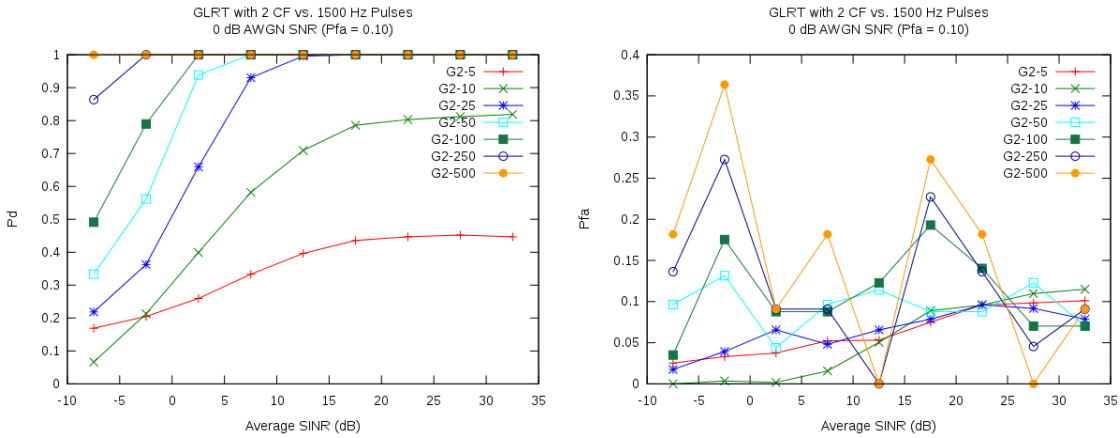

(a) P_d **(b)** P_{fa}

Figure A.59: *GLRT 2 CF vs. 1500Hz Pulses with 10% False Alarm Rate, 0 dB AWGN SNR*

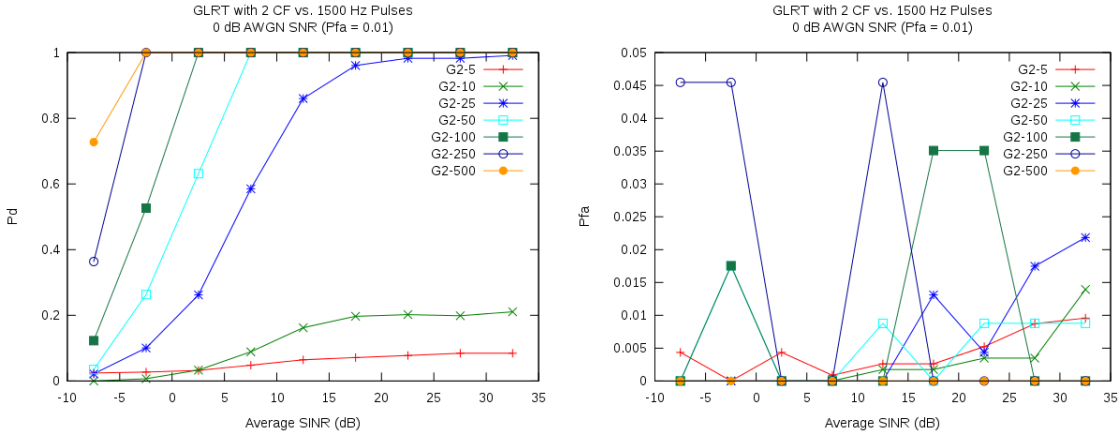

(a) P_d **(b)** P_{fa}

Figure A.60: *GLRT 2 CF vs. 1500Hz Pulses with 1% False Alarm Rate, 0 dB AWGN SNR*

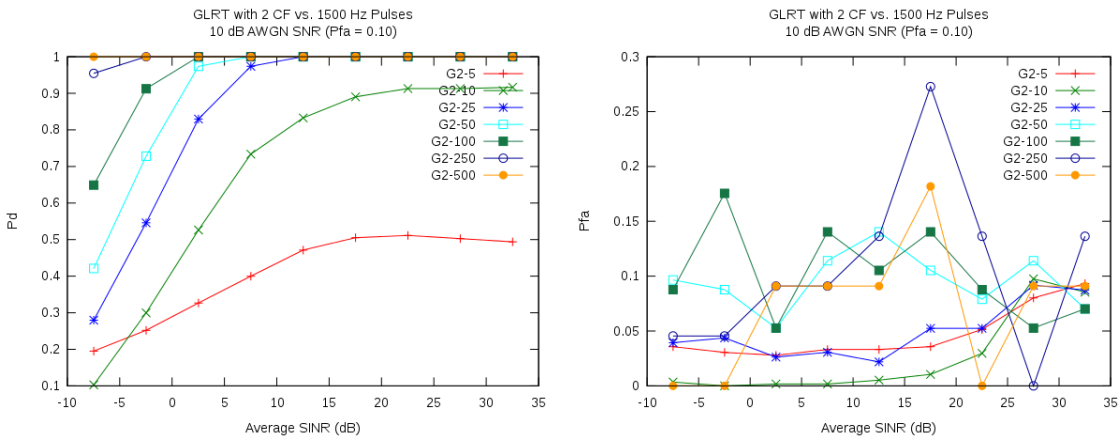

(a) P_d **(b)** P_{fa}

Figure A.61: *GLRT 2 CF vs. 1500Hz Pulses with 10% False Alarm Rate, 10 dB AWGN SNR*

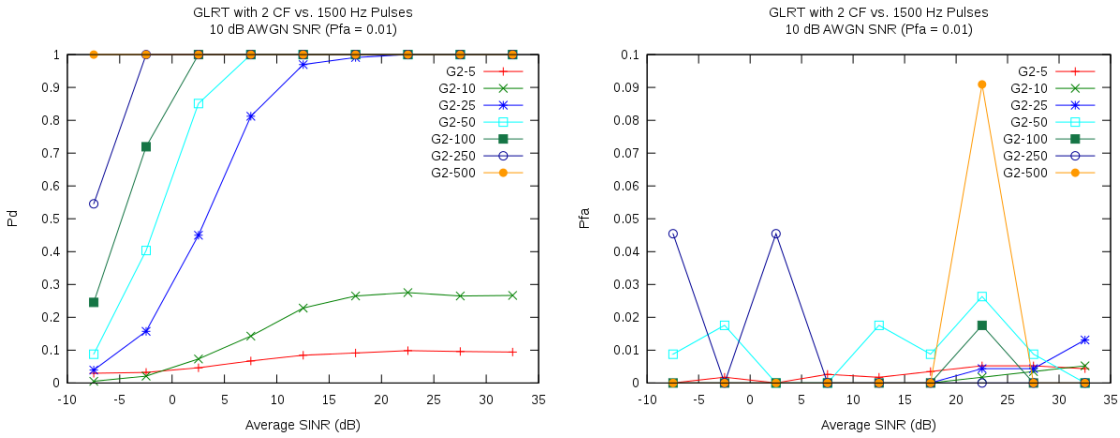

(a) P_d **(b)** P_{fa}

Figure A.62: *GLRT 2 CF vs. 1500Hz Pulses with 1% False Alarm Rate, 10 dB AWGN SNR*

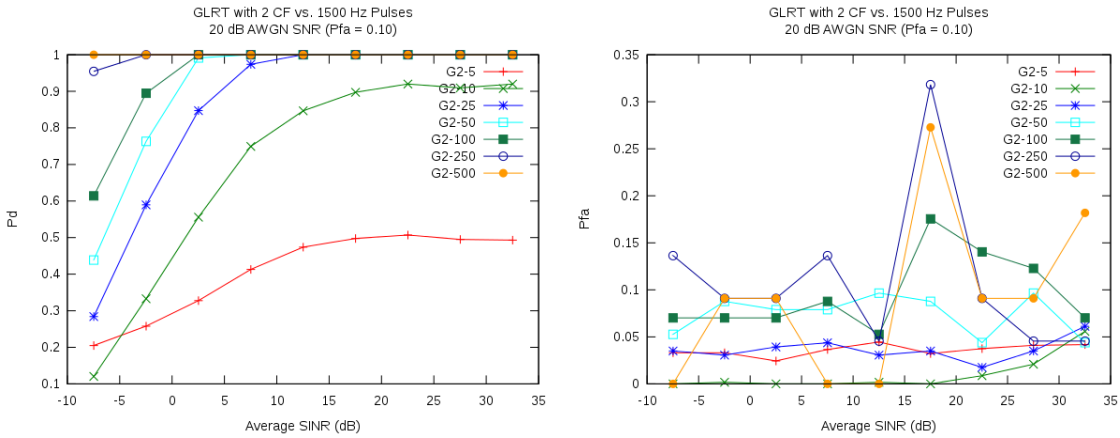

(a) P_d **(b)** P_{fa}

Figure A.63: *GLRT 2 CF vs. 1500Hz Pulses with 10% False Alarm Rate, 20 dB AWGN SNR*

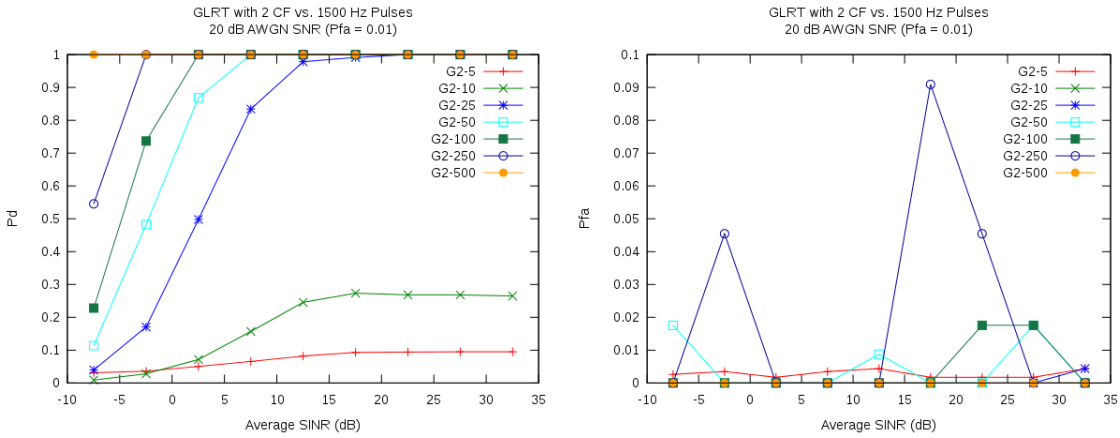

(a) P_d **(b)** P_{fa}

Figure A.64: *GLRT 2 CF vs. 1500Hz Pulses with 1% False Alarm Rate, 20 dB AWGN SNR*

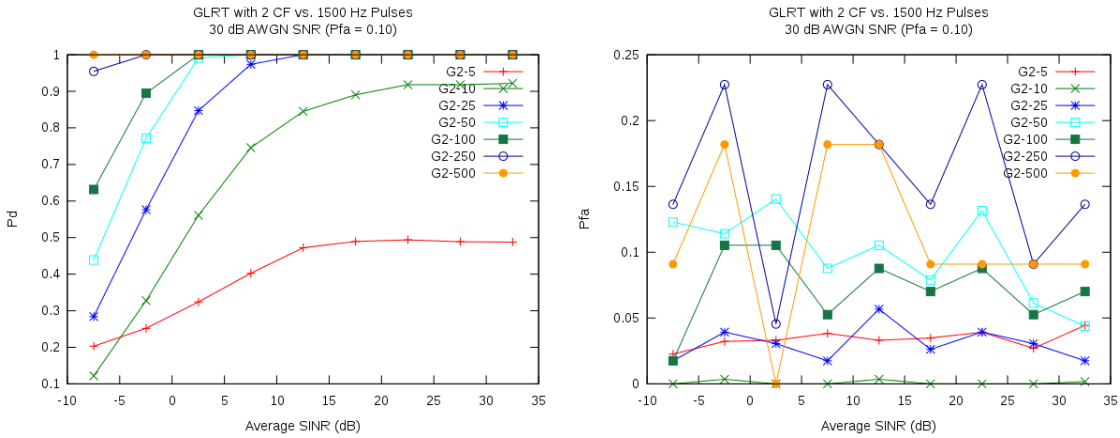

(a) P_d **(b)** P_{fa}

Figure A.65: *GLRT 2 CF vs. 1500Hz Pulses with 10% False Alarm Rate, 30 dB AWGN SNR*

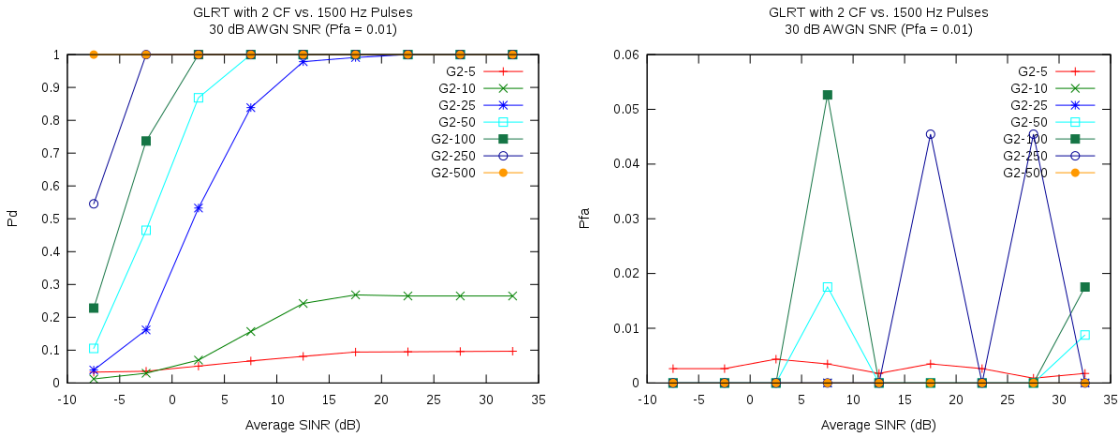

(a) P_d **(b)** P_{fa}

Figure A.66: *GLRT 2 CF vs. 1500Hz Pulses with 1% False Alarm Rate, 30 dB AWGN SNR*

A.4 General Likelihood Ratio Test - Three CFs

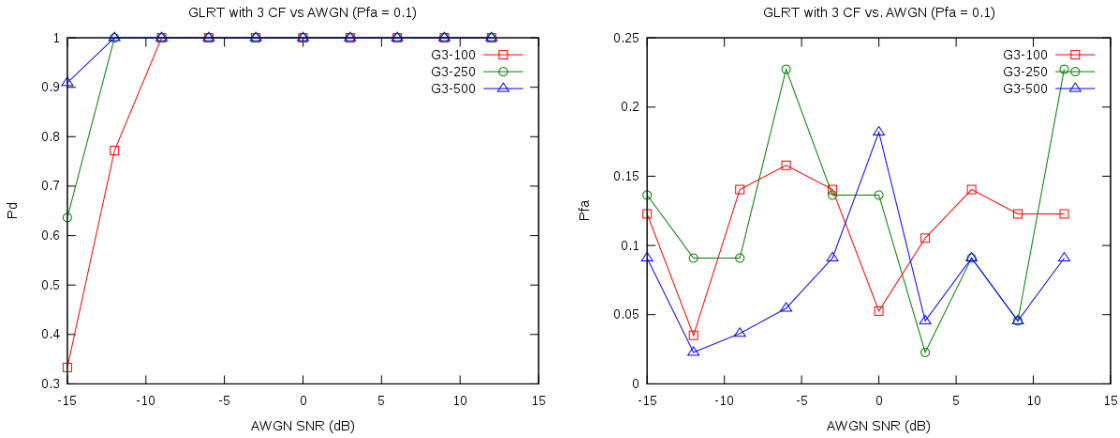

(a) P_d **(b)** P_{fa}

Figure A.67: *GLRT 3 CF vs. AWGN with 10% False Alarm Rate*

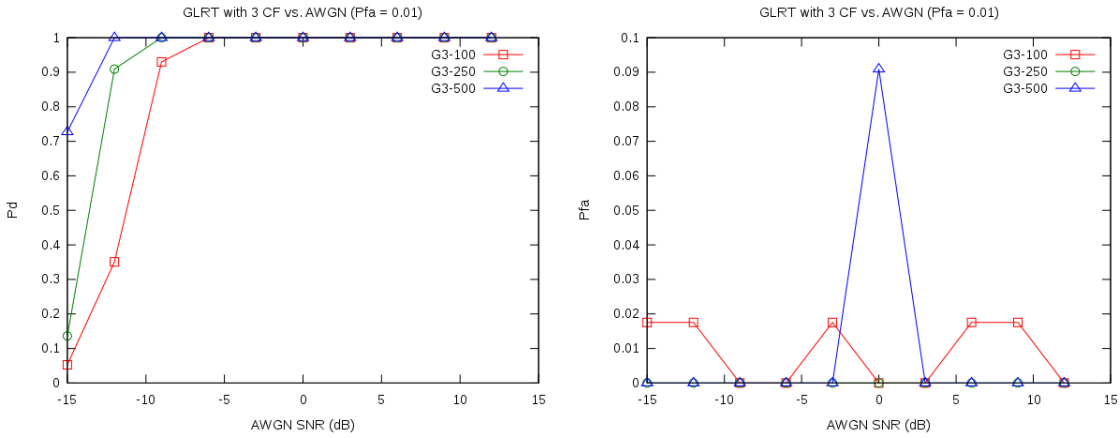

(a) P_d **(b)** P_{fa}

Figure A.68: *GLRT 3 CF vs. AWGN with 1% False Alarm Rate*

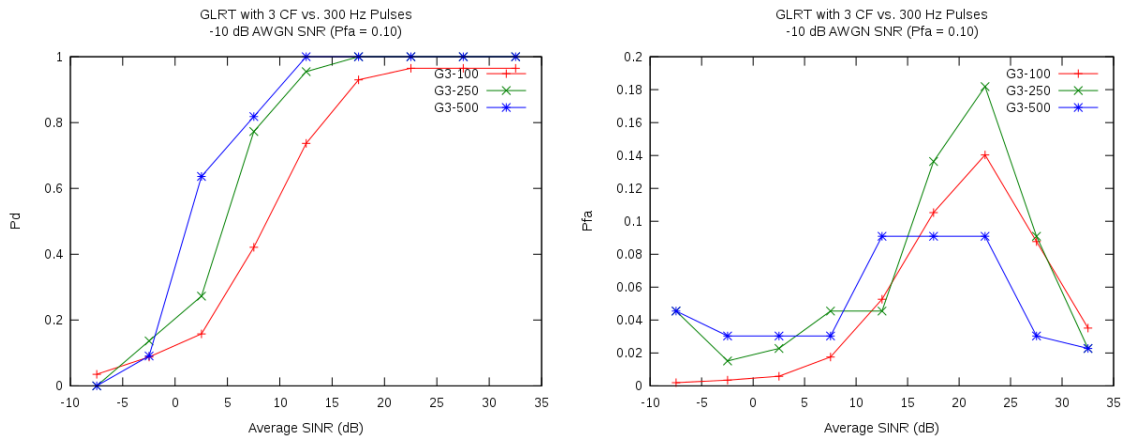

(a) P_d **(b)** P_{fa}

Figure A.69: *GLRT 3 CF vs. 300Hz Pulses with 10% False Alarm Rate, -10 dB AWGN SNR*

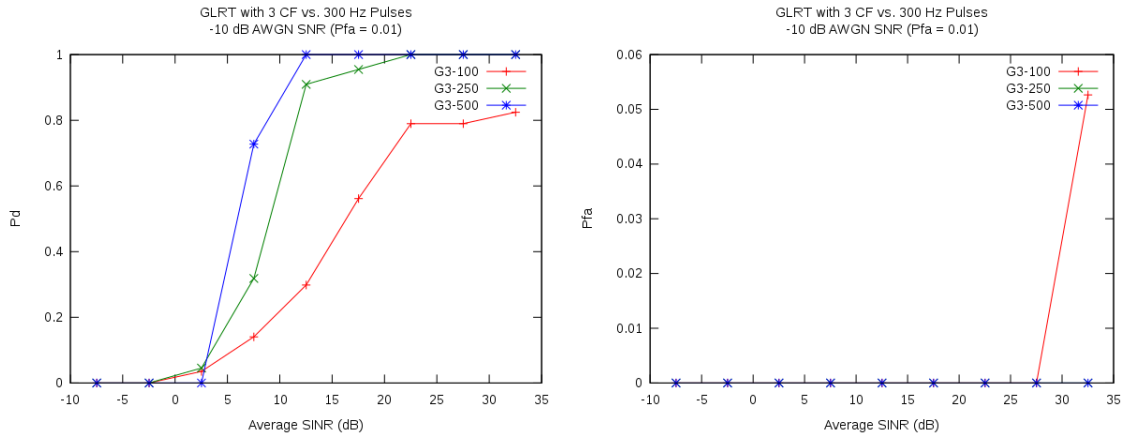

(a) P_d **(b)** P_{fa}

Figure A.70: *GLRT 3 CF vs. 300Hz Pulses with 1% False Alarm Rate, -10 dB AWGN SNR*

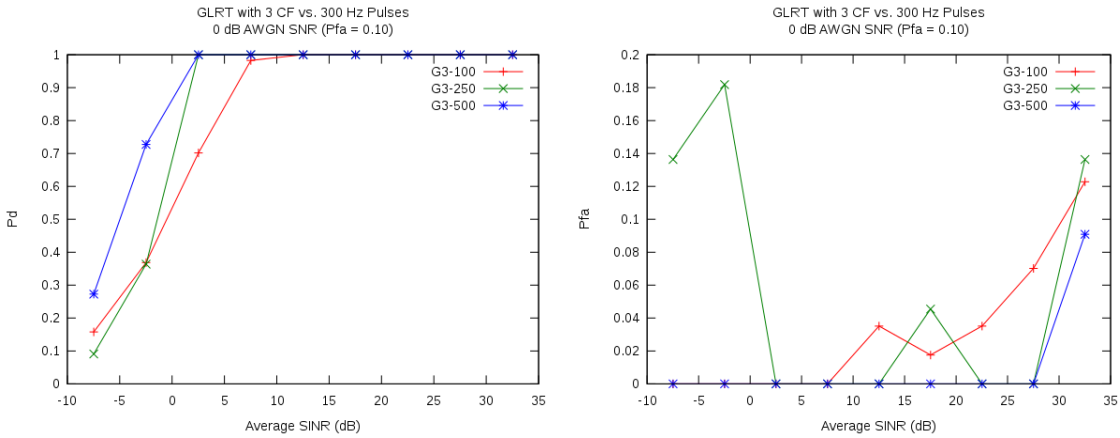

(a) P_d **(b)** P_{fa}

Figure A.71: *GLRT 3 CF vs. 300Hz Pulses with 10% False Alarm Rate, 0 dB AWGN SNR*

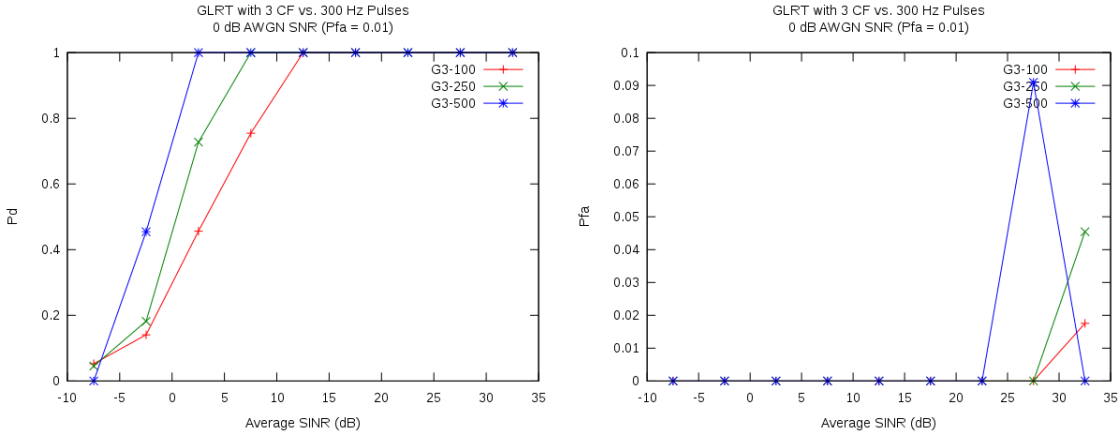

(a) P_d **(b)** P_{fa}

Figure A.72: *GLRT 3 CF vs. 300Hz Pulses with 1% False Alarm Rate, 0 dB AWGN SNR*

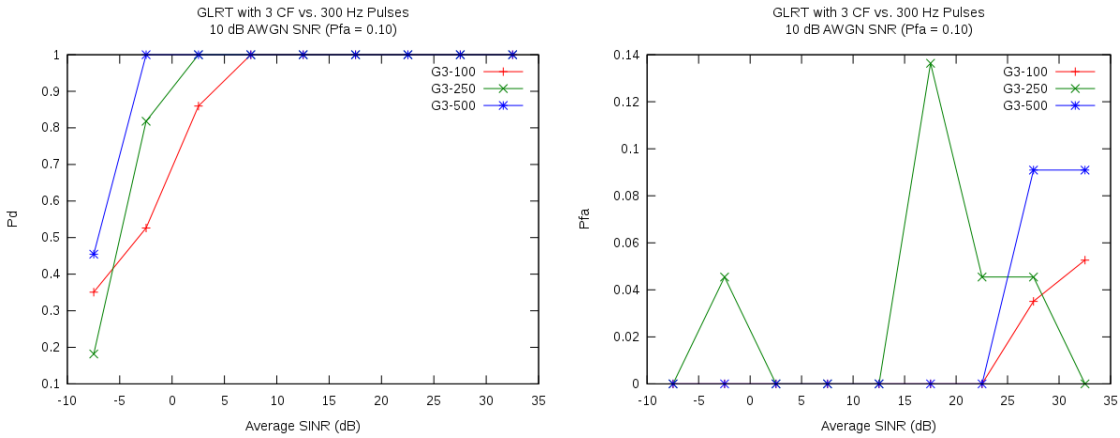

(a) P_d **(b)** P_{fa}

Figure A.73: *GLRT 3 CF vs. 300Hz Pulses with 10% False Alarm Rate, 10 dB AWGN SNR*

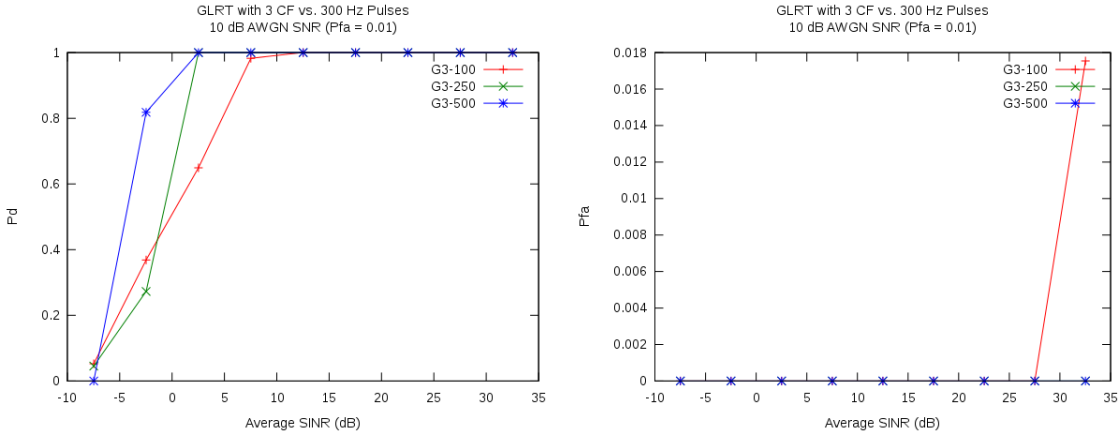

(a) P_d **(b)** P_{fa}

Figure A.74: *GLRT 3 CF vs. 300Hz Pulses with 1% False Alarm Rate, 10 dB AWGN SNR*

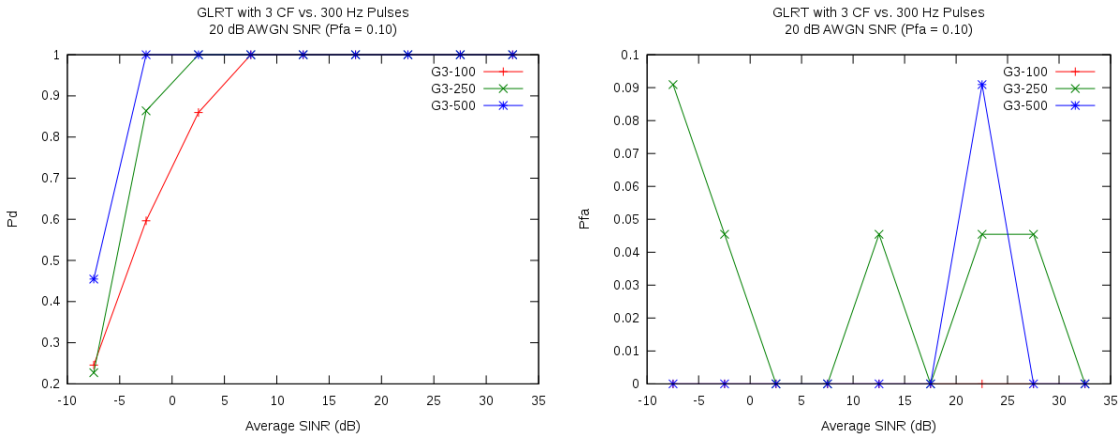

(a) P_d **(b)** P_{fa}

Figure A.75: *GLRT 3 CF vs. 300Hz Pulses with 10% False Alarm Rate, 20 dB AWGN SNR*

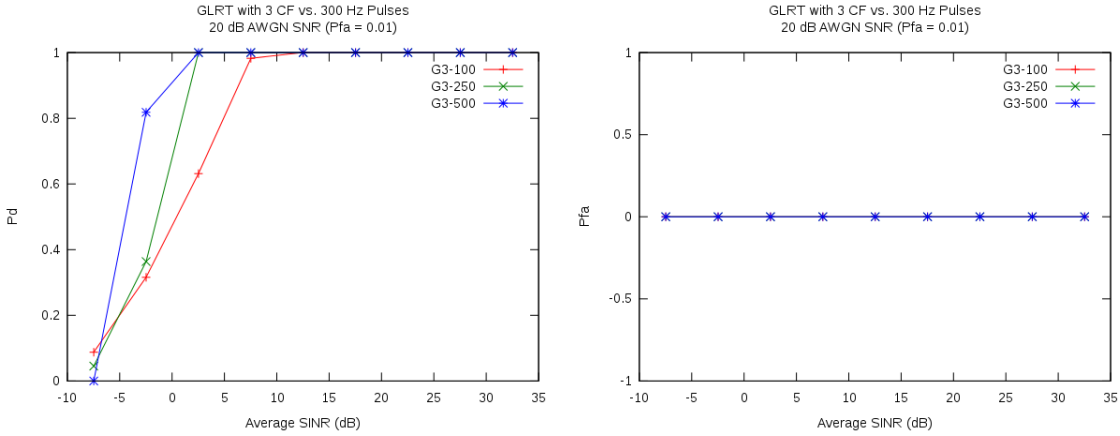

(a) P_d **(b)** P_{fa}

Figure A.76: *GLRT 3 CF vs. 300Hz Pulses with 1% False Alarm Rate, 20 dB AWGN SNR*

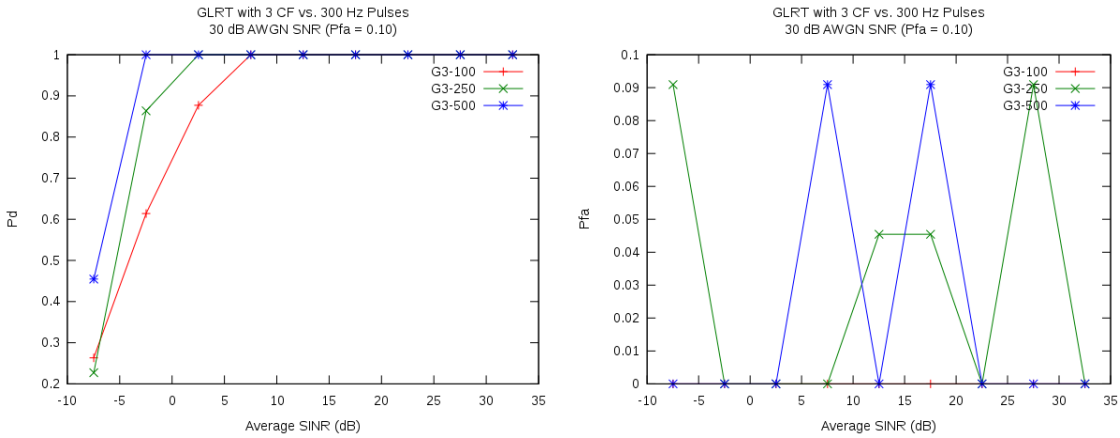

(a) P_d **(b)** P_{fa}

Figure A.77: *GLRT 3 CF vs. 300Hz Pulses with 10% False Alarm Rate, 30 dB AWGN SNR*

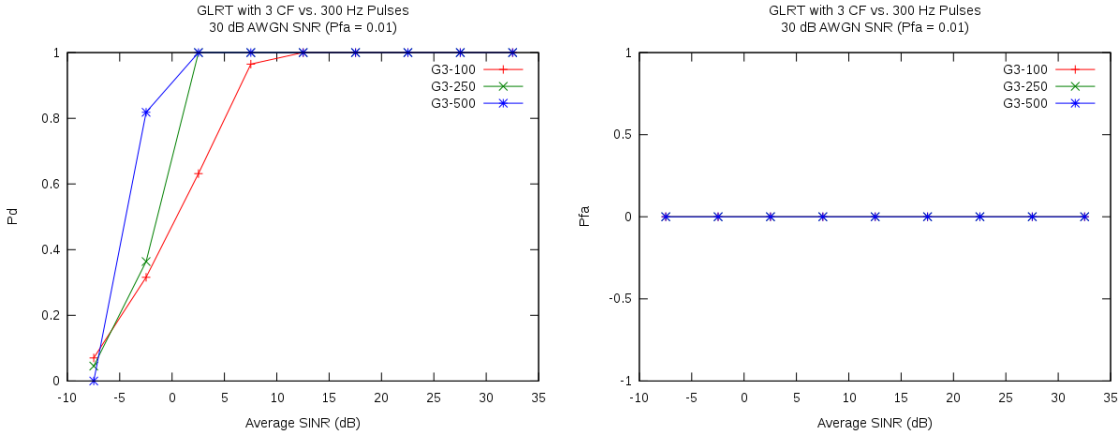

(a) P_d **(b)** P_{fa}

Figure A.78: *GLRT 3 CF vs. 300Hz Pulses with 1% False Alarm Rate, 30 dB AWGN SNR*

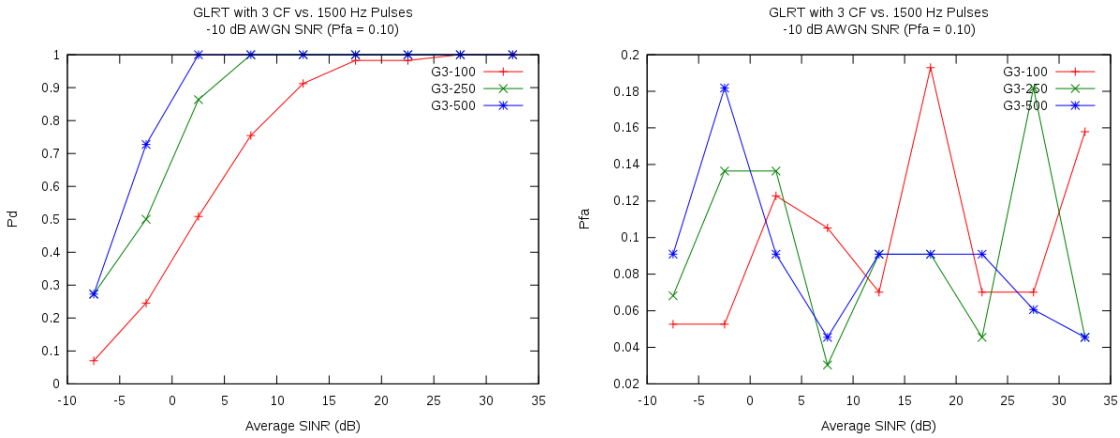

(a) P_d **(b)** P_{fa}

Figure A.79: *GLRT 3 CF vs. 1500Hz Pulses with 10% False Alarm Rate, -10 dB AWGN SNR*

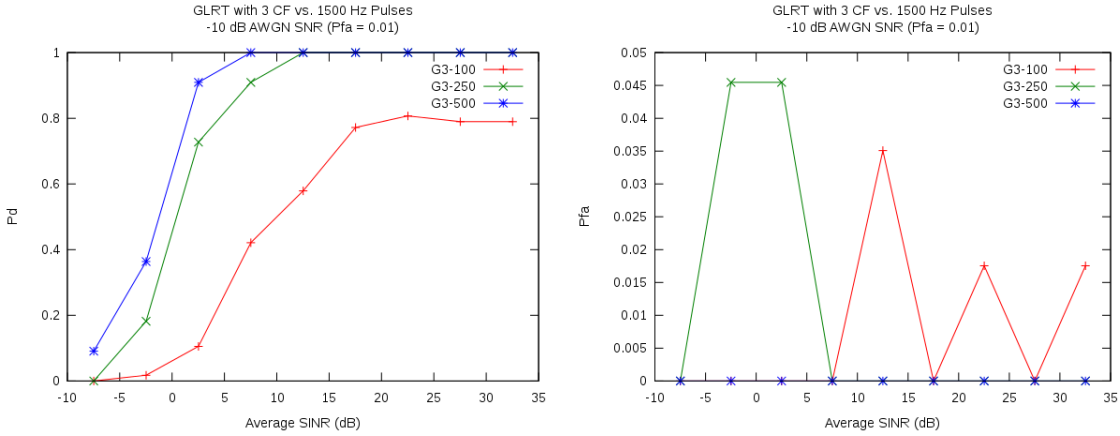

(a) P_d **(b)** P_{fa}

Figure A.80: *GLRT 3 CF vs. 1500Hz Pulses with 1% False Alarm Rate, -10 dB AWGN SNR*

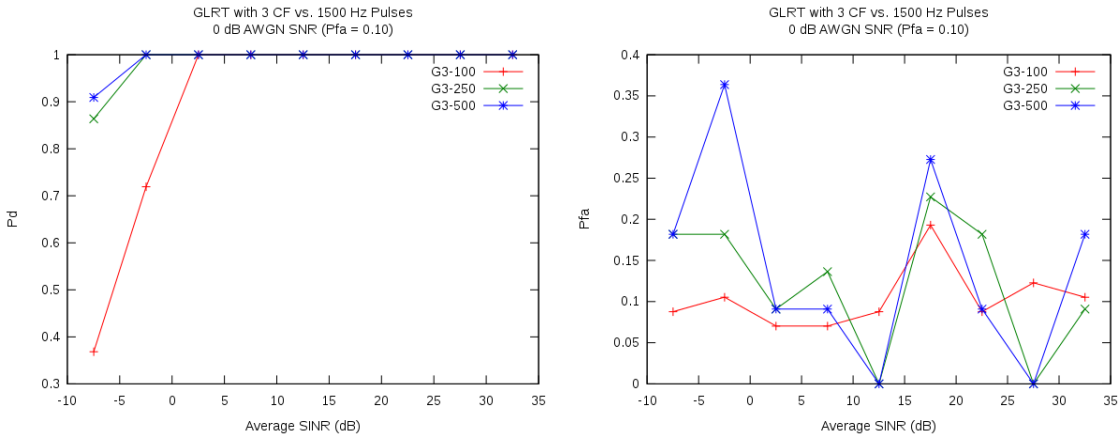

(a) P_d **(b)** P_{fa}

Figure A.81: *GLRT 3 CF vs. 1500Hz Pulses with 10% False Alarm Rate, 0 dB AWGN SNR*

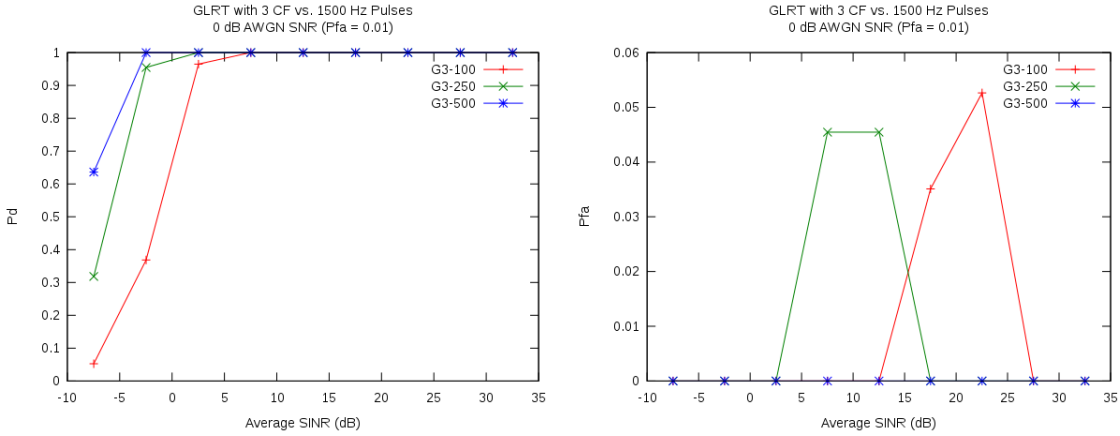

(a) P_d **(b)** P_{fa}

Figure A.82: *GLRT 3 CF vs. 1500Hz Pulses with 1% False Alarm Rate, 0 dB AWGN SNR*

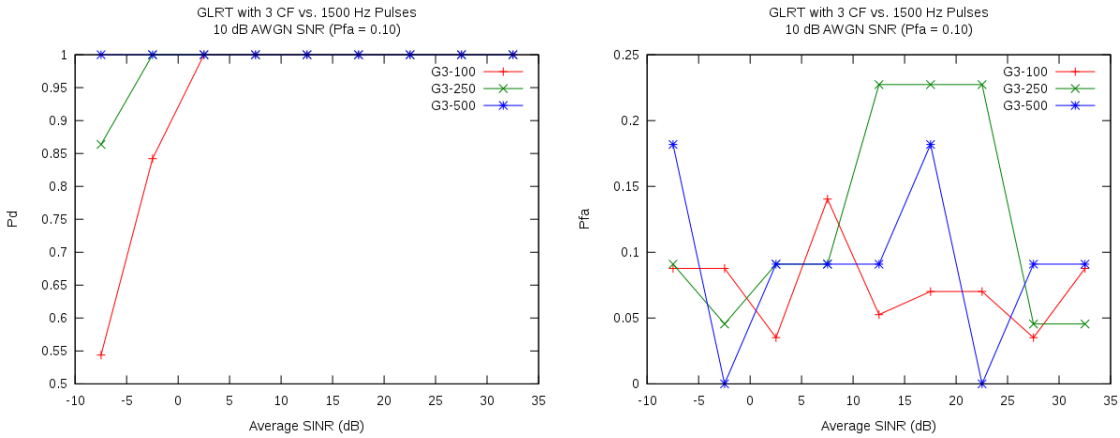

(a) P_d **(b)** P_{fa}

Figure A.83: *GLRT 3 CF vs. 1500Hz Pulses with 10% False Alarm Rate, 10 dB AWGN SNR*

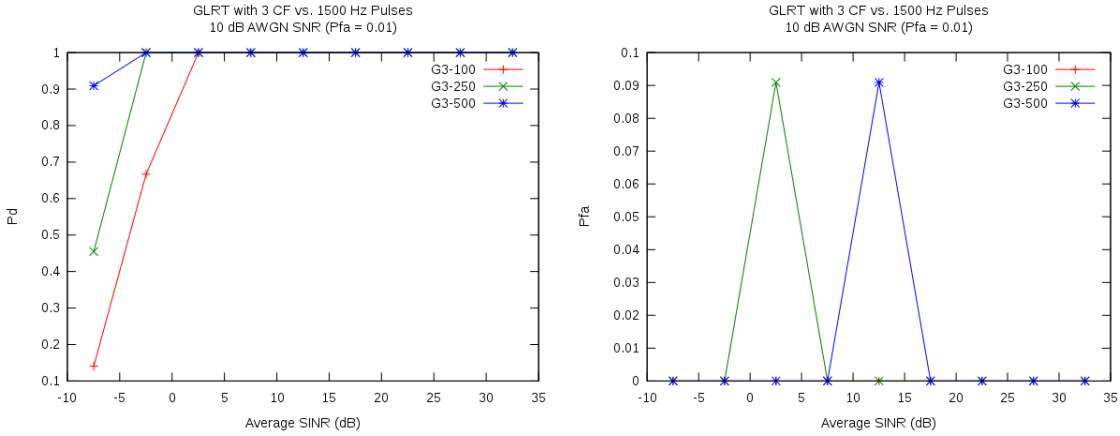

(a) P_d **(b)** P_{fa}

Figure A.84: *GLRT 3 CF vs. 1500Hz Pulses with 1% False Alarm Rate, 10 dB AWGN SNR*

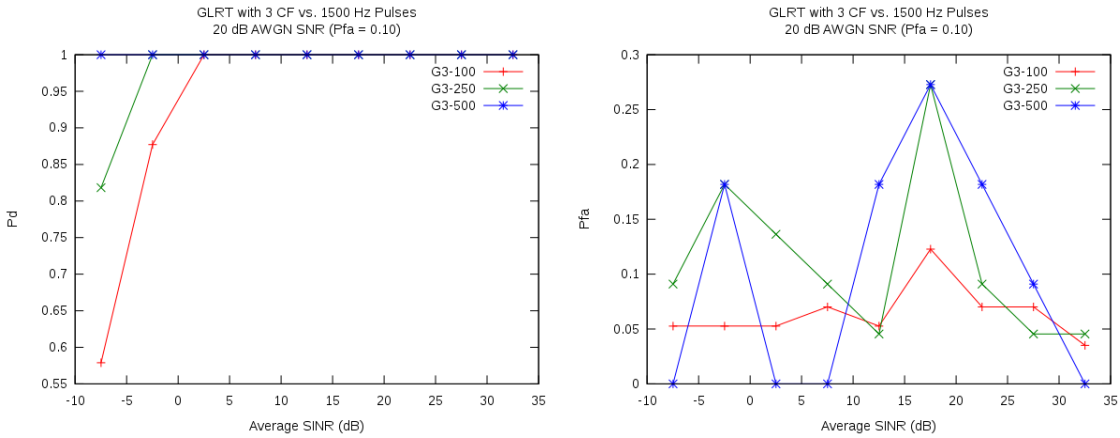

(a) P_d **(b)** P_{fa}

Figure A.85: *GLRT 3 CF vs. 1500Hz Pulses with 10% False Alarm Rate, 20 dB AWGN SNR*

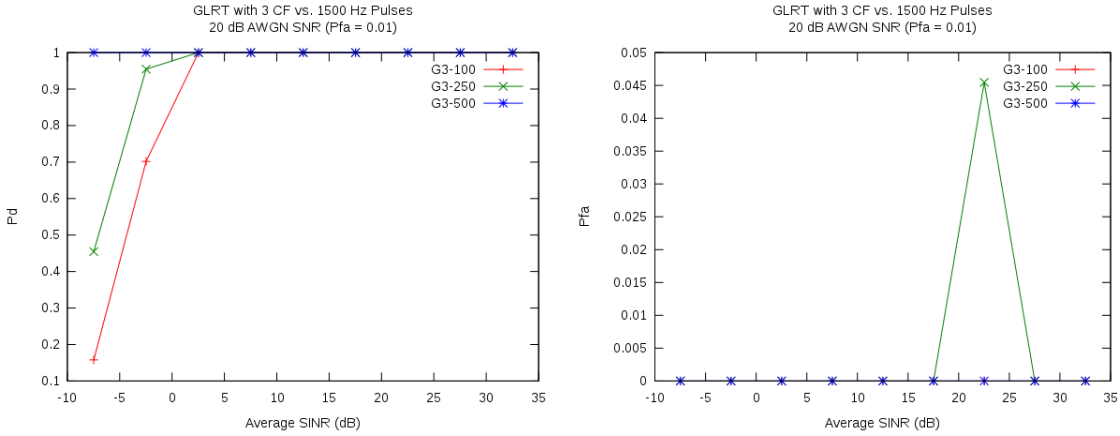

(a) P_d **(b)** P_{fa}

Figure A.86: *GLRT 3 CF vs. 1500Hz Pulses with 1% False Alarm Rate, 20 dB AWGN SNR*

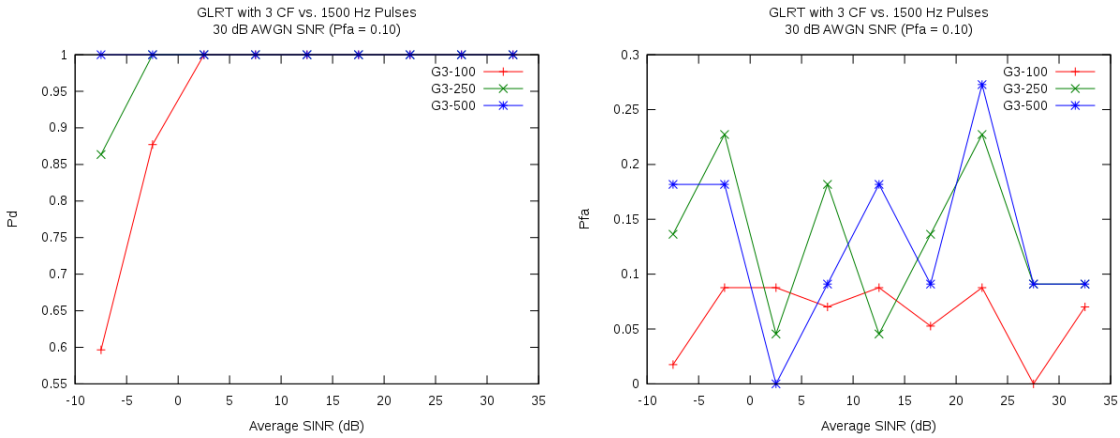

(a) P_d **(b)** P_{fa}

Figure A.87: *GLRT 3 CF vs. 1500Hz Pulses with 10% False Alarm Rate, 30 dB AWGN SNR*

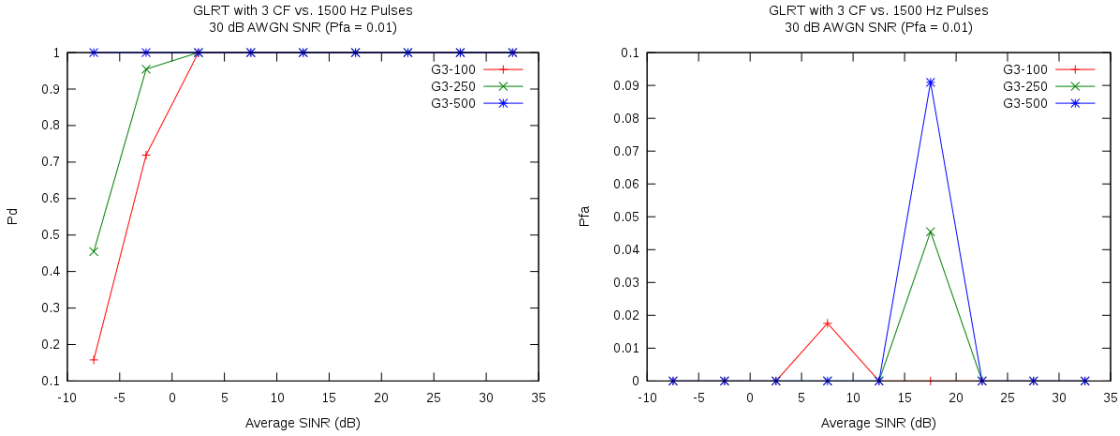

(a) P_d **(b)** P_{fa}

Figure A.88: *GLRT 3 CF vs. 1500Hz Pulses with 1% False Alarm Rate, 30 dB AWGN SNR*

A.5 General Likelihood Ratio Test - Four CFs

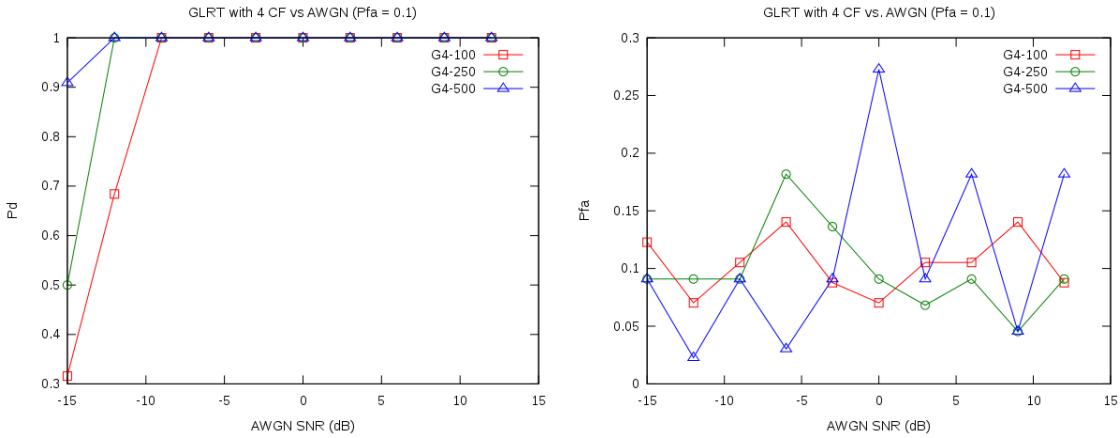

(a) P_d **(b)** P_{fa}

Figure A.89: *GLRT 4 CF vs. AWGN with 10% False Alarm Rate*

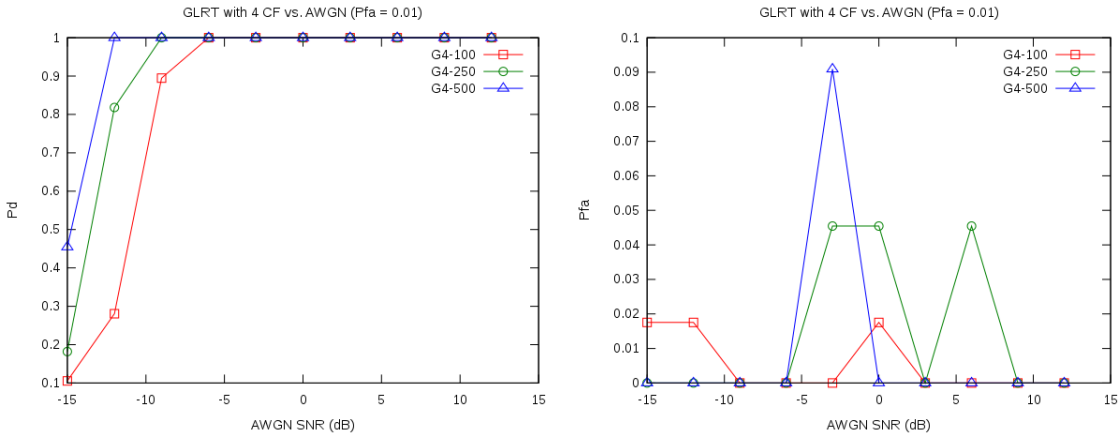

(a) P_d **(b)** P_{fa}

Figure A.90: *GLRT 4 CF vs. AWGN with 1% False Alarm Rate*

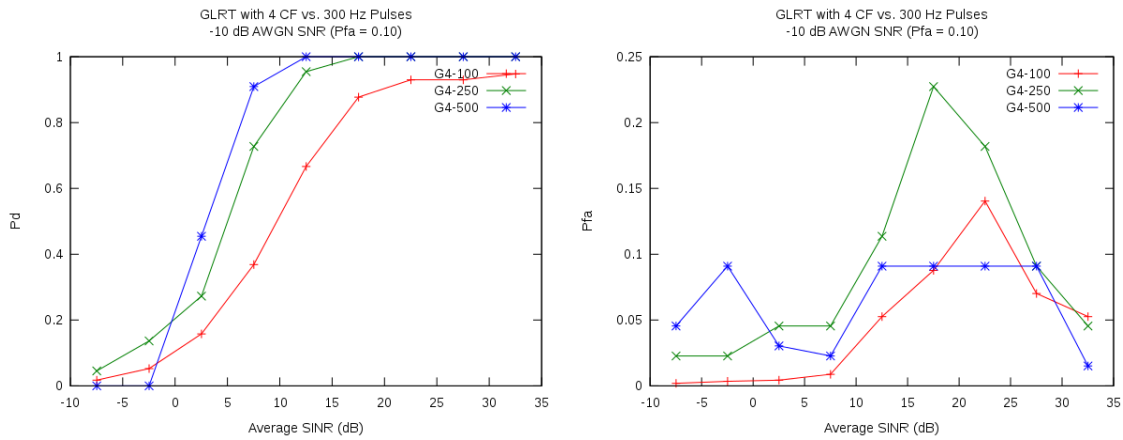

(a) P_d **(b)** P_{fa}

Figure A.91: *GLRT 4 CF vs. 300Hz Pulses with 10% False Alarm Rate, -10 dB AWGN SNR*

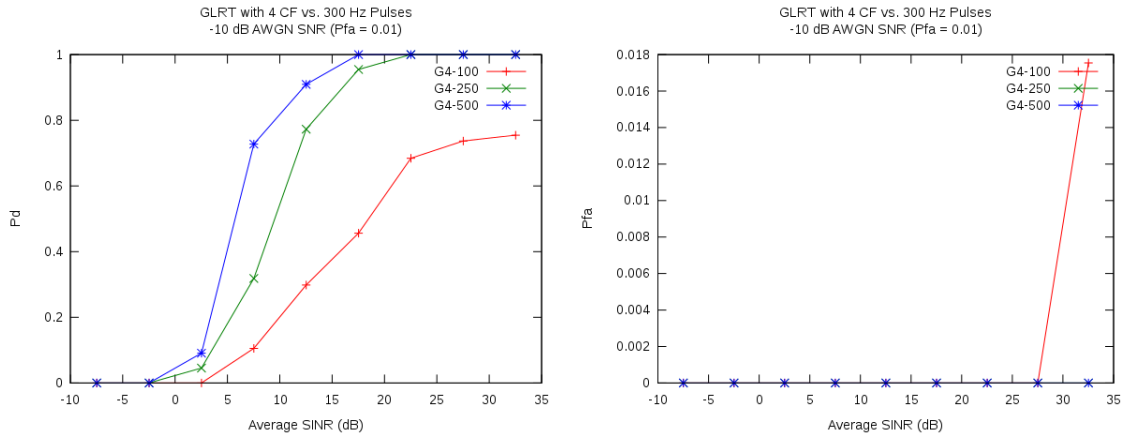

(a) P_d **(b)** P_{fa}

Figure A.92: *GLRT 4 CF vs. 300Hz Pulses with 1% False Alarm Rate, -10 dB AWGN SNR*

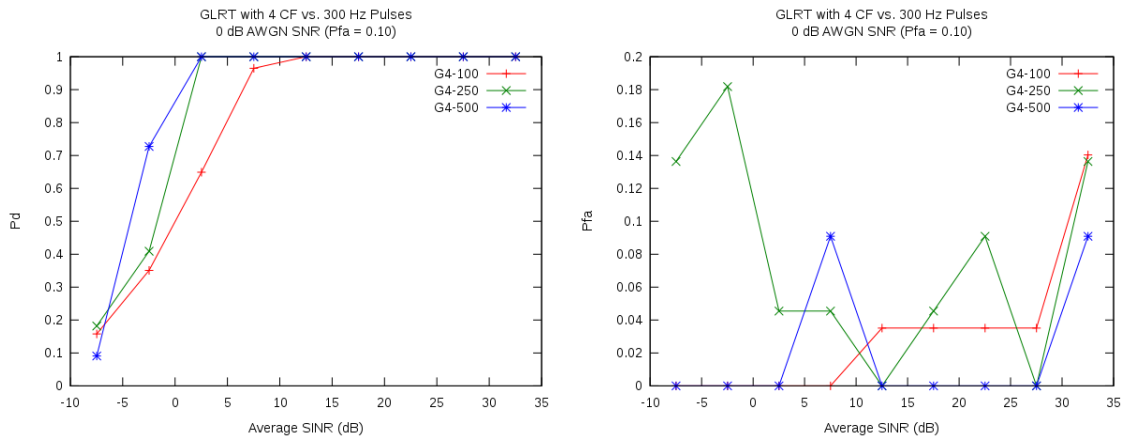

(a) P_d **(b)** P_{fa}

Figure A.93: *GLRT 4 CF vs. 300Hz Pulses with 10% False Alarm Rate, 0 dB AWGN SNR*

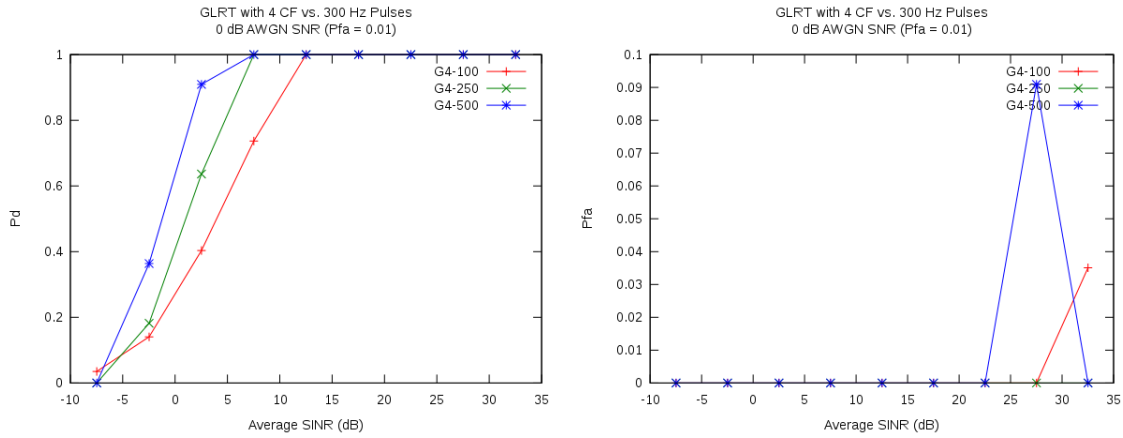

(a) P_d **(b)** P_{fa}

Figure A.94: *GLRT 4 CF vs. 300Hz Pulses with 1% False Alarm Rate, 0 dB AWGN SNR*

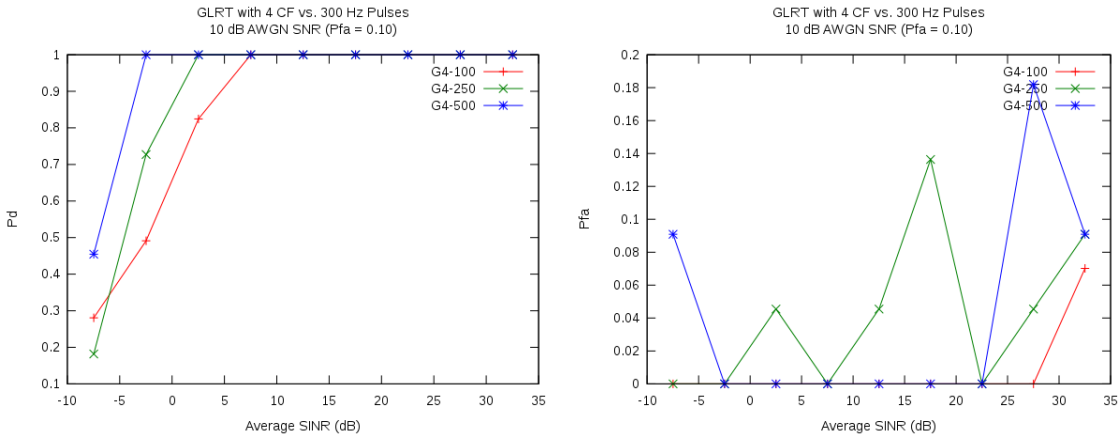

(a) P_d **(b)** P_{fa}

Figure A.95: *GLRT 4 CF vs. 300Hz Pulses with 10% False Alarm Rate, 10 dB AWGN SNR*

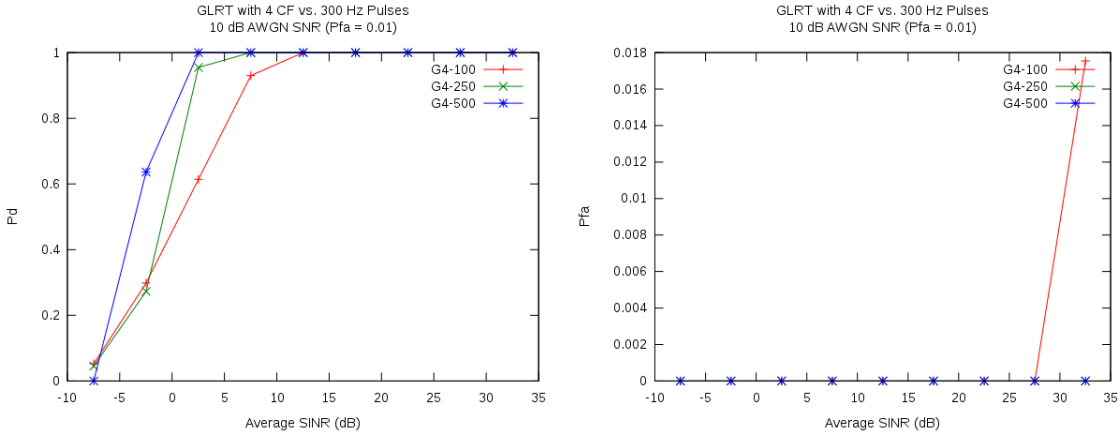

(a) P_d **(b)** P_{fa}

Figure A.96: *GLRT 4 CF vs. 300Hz Pulses with 1% False Alarm Rate, 10 dB AWGN SNR*

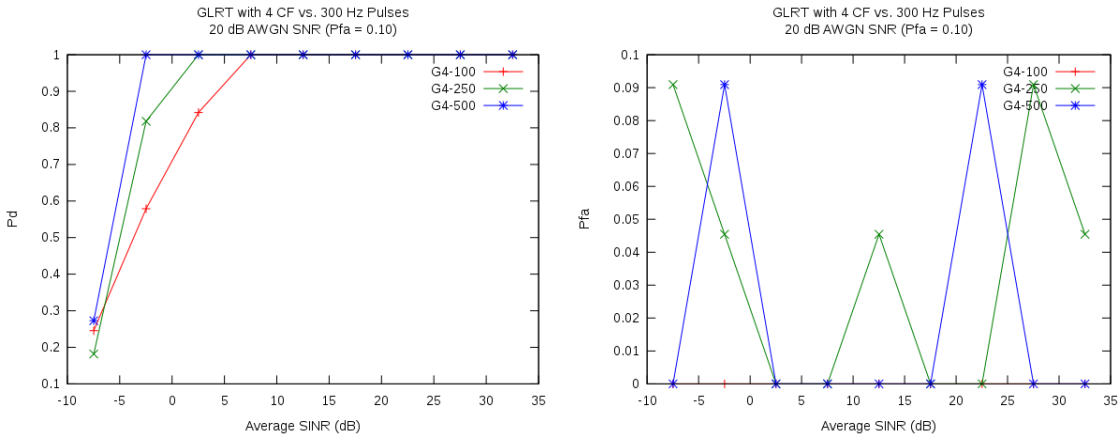

(a) P_d **(b)** P_{fa}

Figure A.97: *GLRT 4 CF vs. 300Hz Pulses with 10% False Alarm Rate, 20 dB AWGN SNR*

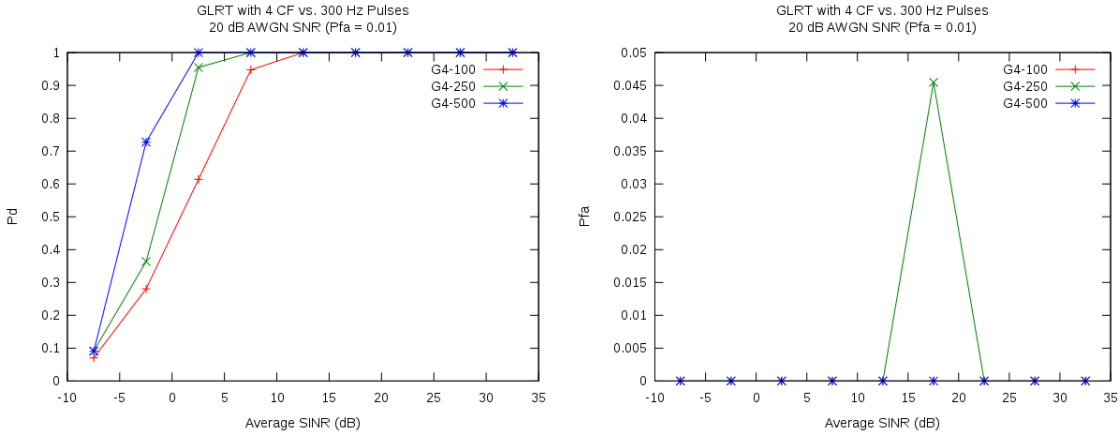

(a) P_d **(b)** P_{fa}

Figure A.98: *GLRT 4 CF vs. 300Hz Pulses with 1% False Alarm Rate, 20 dB AWGN SNR*

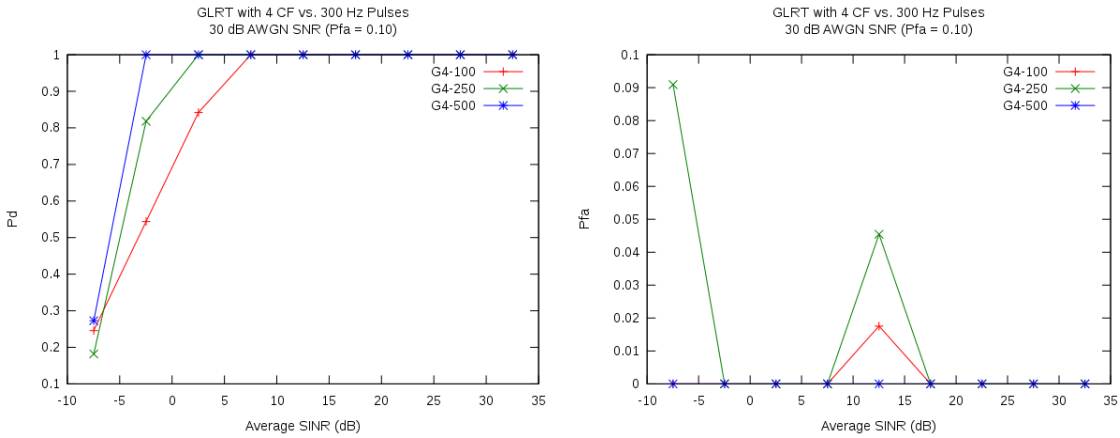

(a) P_d **(b)** P_{fa}

Figure A.99: *GLRT 4 CF vs. 300Hz Pulses with 10% False Alarm Rate, 30 dB AWGN SNR*

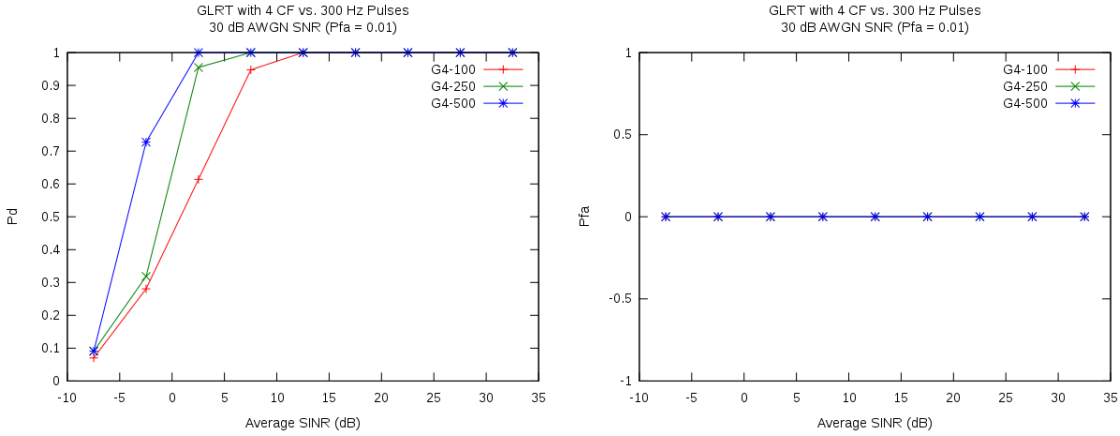

(a) P_d **(b)** P_{fa}

Figure A.100: *GLRT 4 CF vs. 300Hz Pulses with 1% False Alarm Rate, 30 dB AWGN SNR*

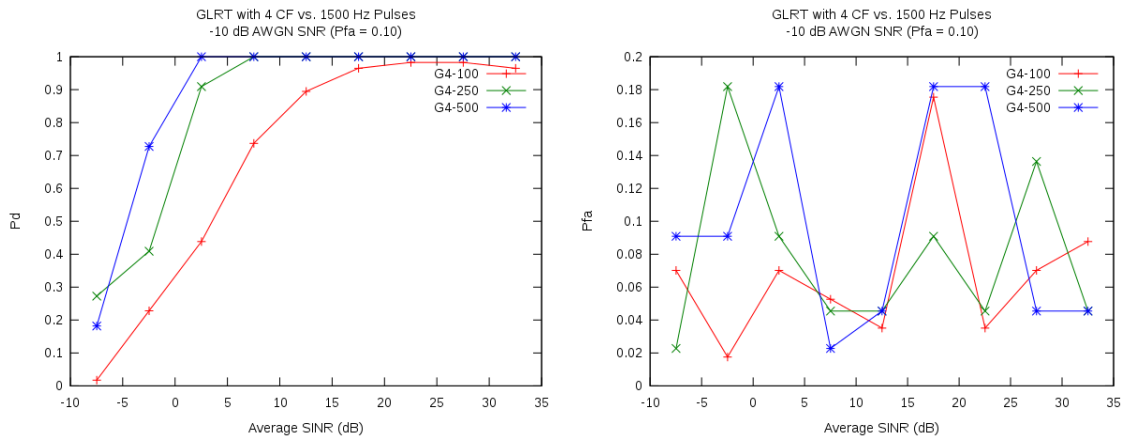

(a) P_d **(b)** P_{fa}

Figure A.101: *GLRT 4 CF vs. 1500Hz Pulses with 10% False Alarm Rate, -10 dB AWGN SNR*

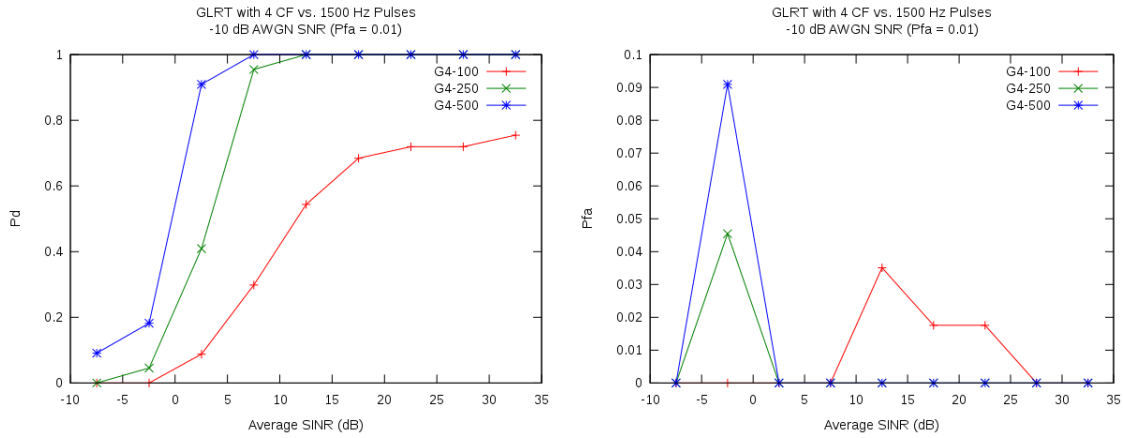

(a) P_d **(b)** P_{fa}

Figure A.102: *GLRT 4 CF vs. 1500Hz Pulses with 1% False Alarm Rate, -10 dB AWGN SNR*

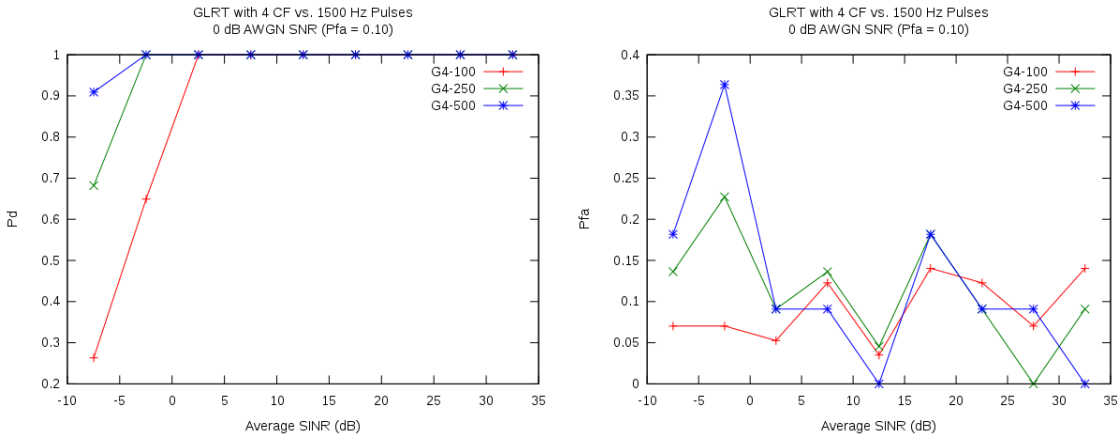

(a) P_d **(b)** P_{fa}

Figure A.103: *GLRT 4 CF vs. 1500Hz Pulses with 10% False Alarm Rate, 0 dB AWGN SNR*

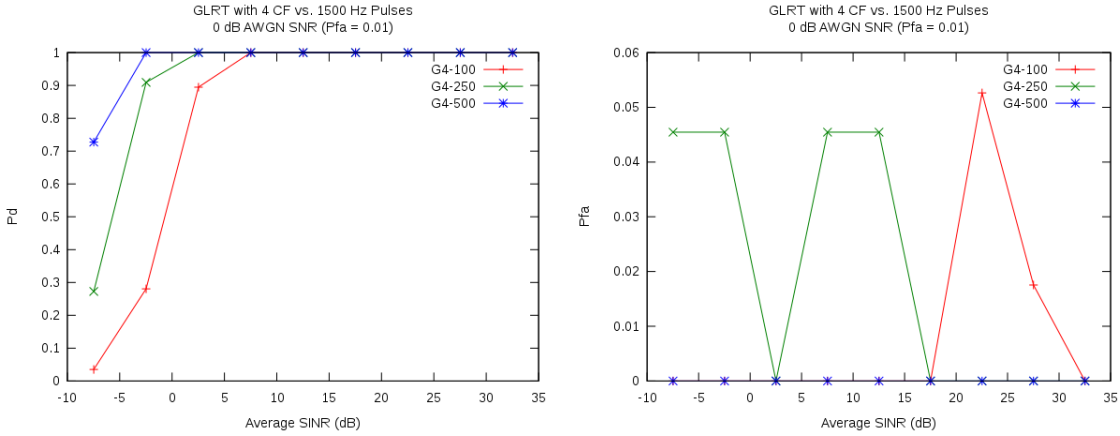

(a) P_d **(b)** P_{fa}

Figure A.104: *GLRT 4 CF vs. 1500Hz Pulses with 1% False Alarm Rate, 0 dB AWGN SNR*

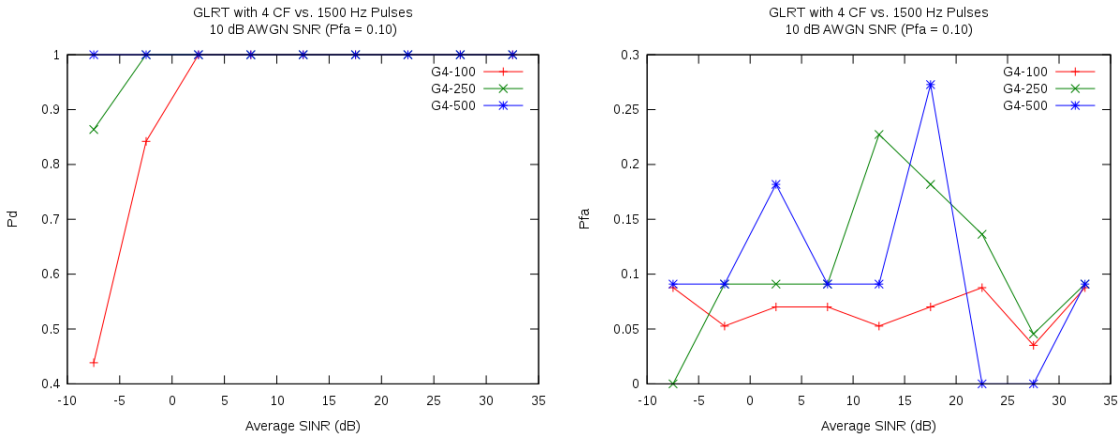

(a) P_d **(b)** P_{fa}

Figure A.105: *GLRT 4 CF vs. 1500Hz Pulses with 10% False Alarm Rate, 10 dB AWGN SNR*

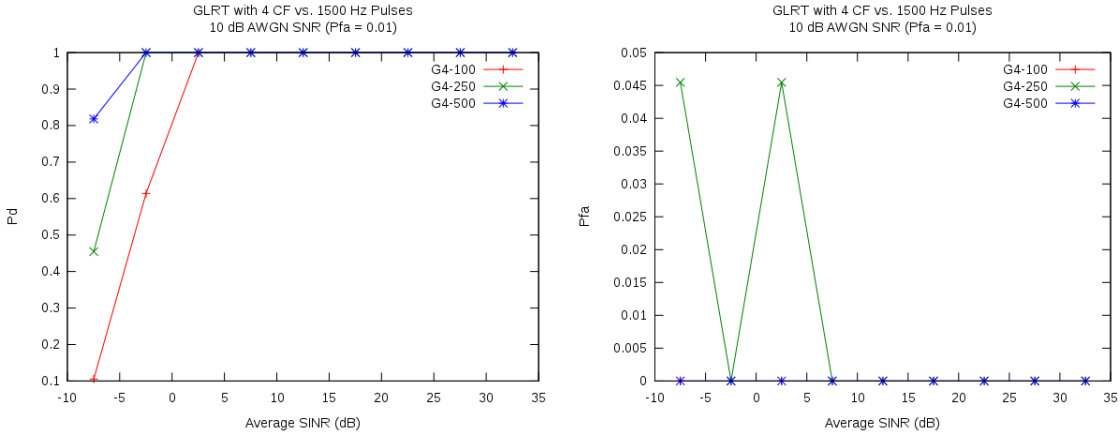

(a) P_d **(b)** P_{fa}

Figure A.106: *GLRT 4 CF vs. 1500Hz Pulses with 1% False Alarm Rate, 10 dB AWGN SNR*

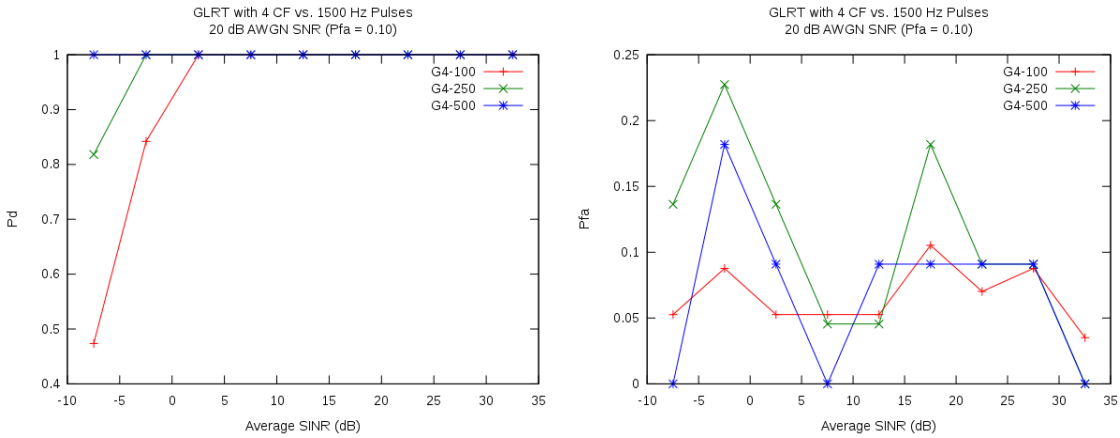

(a) P_d **(b)** P_{fa}

Figure A.107: *GLRT 4 CF vs. 1500Hz Pulses with 10% False Alarm Rate, 20 dB AWGN SNR*

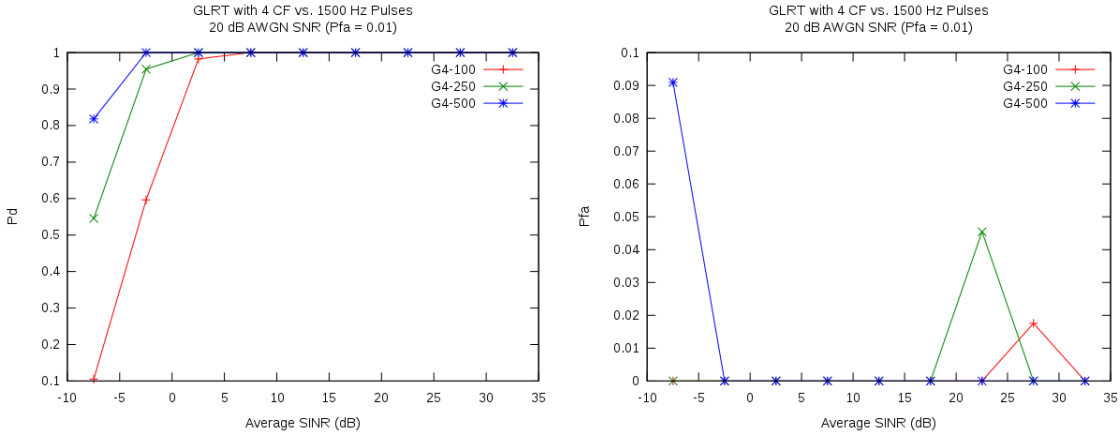

(a) P_d **(b)** P_{fa}

Figure A.108: *GLRT 4 CF vs. 1500Hz Pulses with 1% False Alarm Rate, 20 dB AWGN SNR*

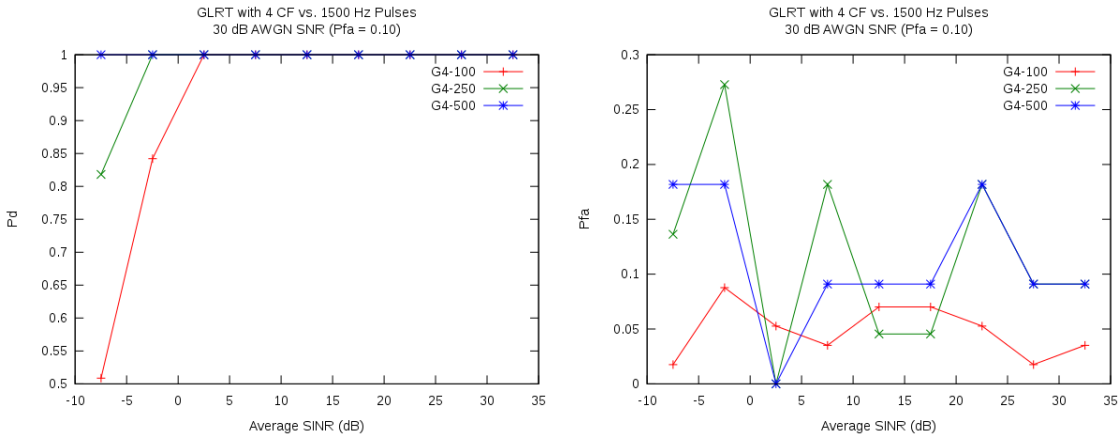

(a) P_d **(b)** P_{fa}

Figure A.109: *GLRT 4 CF vs. 1500Hz Pulses with 10% False Alarm Rate, 30 dB AWGN SNR*

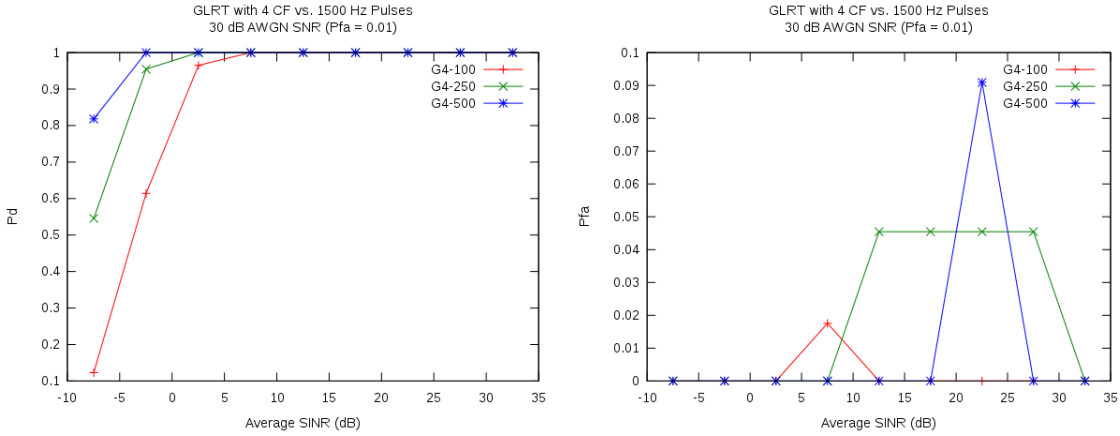

(a) P_d **(b)** P_{fa}

Figure A.110: *GLRT 4 CF vs. 1500Hz Pulses with 1% False Alarm Rate, 30 dB AWGN SNR*

A.6 Support Vector Machine - No Noise Training

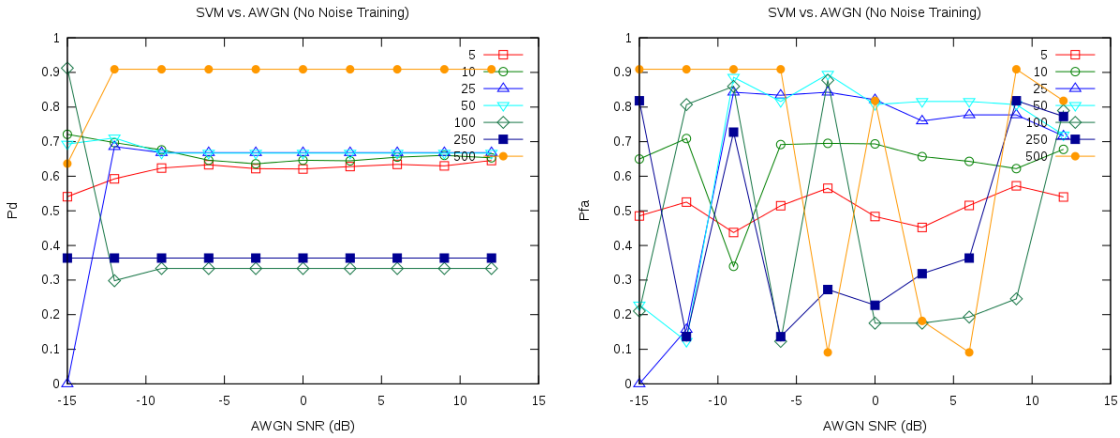

(a) P_d **(b)** P_{fa}

Figure A.111: *SVM Detector with No Noise Training vs. AWGN*

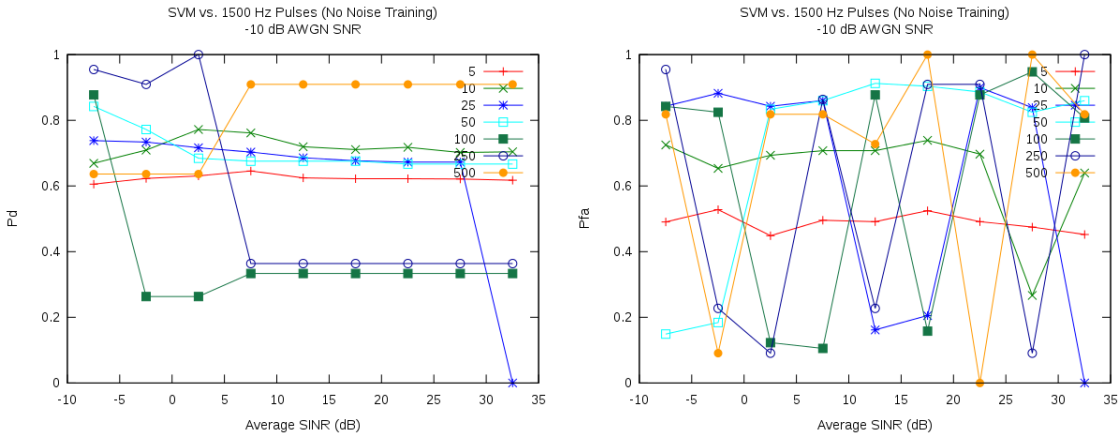

(a) P_d **(b)** P_{fa}

Figure A.112: *SVM Detector with No Noise Training vs. 1500Hz Pulses, -10 dB AWGN SNR*

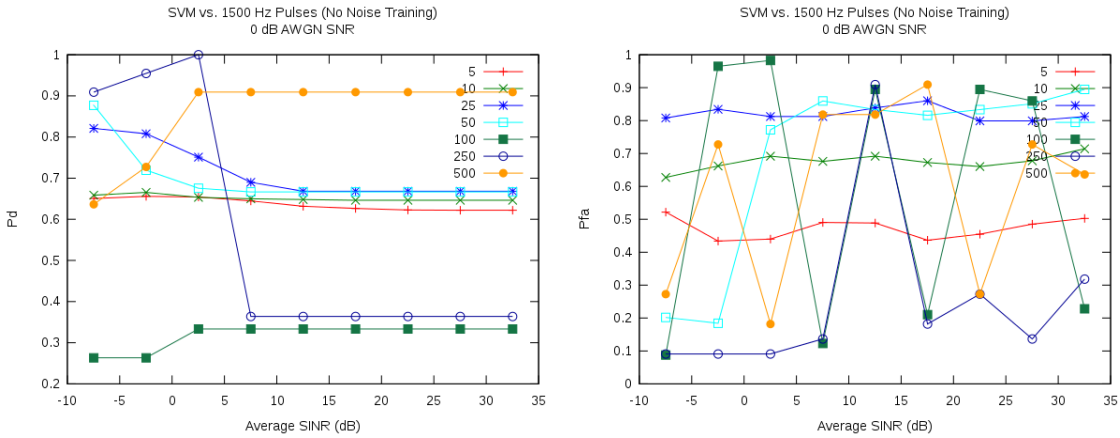

(a) P_d **(b)** P_{fa}

Figure A.113: *SVM Detector with No Noise Training vs. 1500Hz Pulses, 0 dB AWGN SNR*

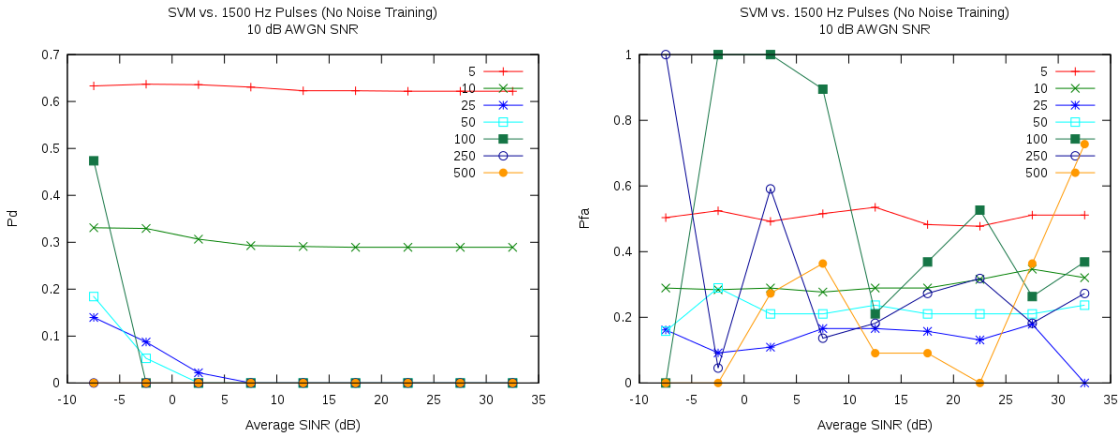

(a) P_d **(b)** P_{fa}

Figure A.114: *SVM Detector with No Noise Training vs. 1500Hz Pulses, 10 dB AWGN SNR*

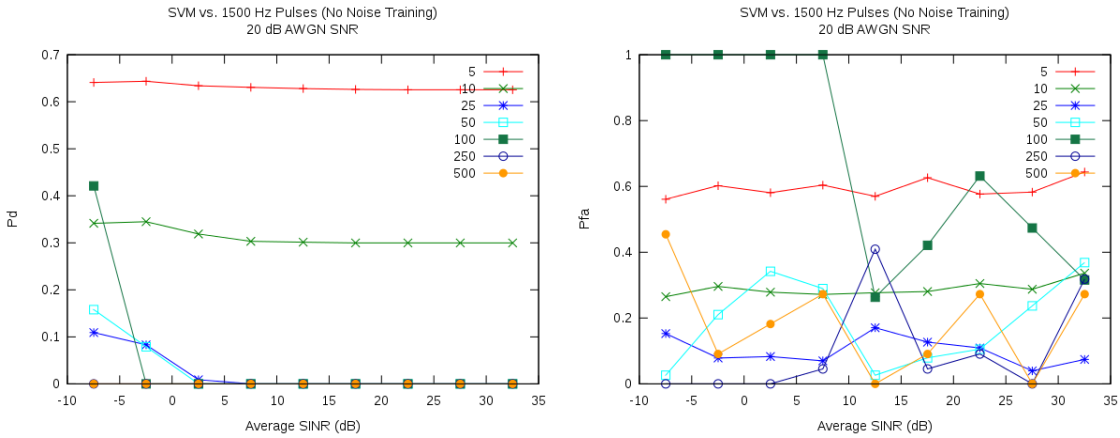

(a) P_d **(b)** P_{fa}

Figure A.115: *SVM Detector with No Noise Training vs. 1500Hz Pulses, 20 dB AWGN SNR*

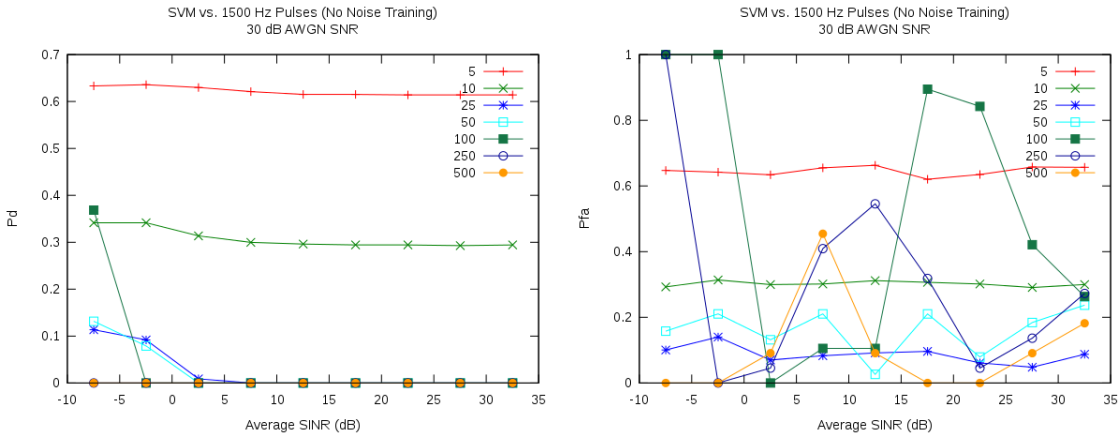

(a) P_d **(b)** P_{fa}

Figure A.116: *SVM Detector with No Noise Training vs. 1500Hz Pulses, 30 dB AWGN SNR*

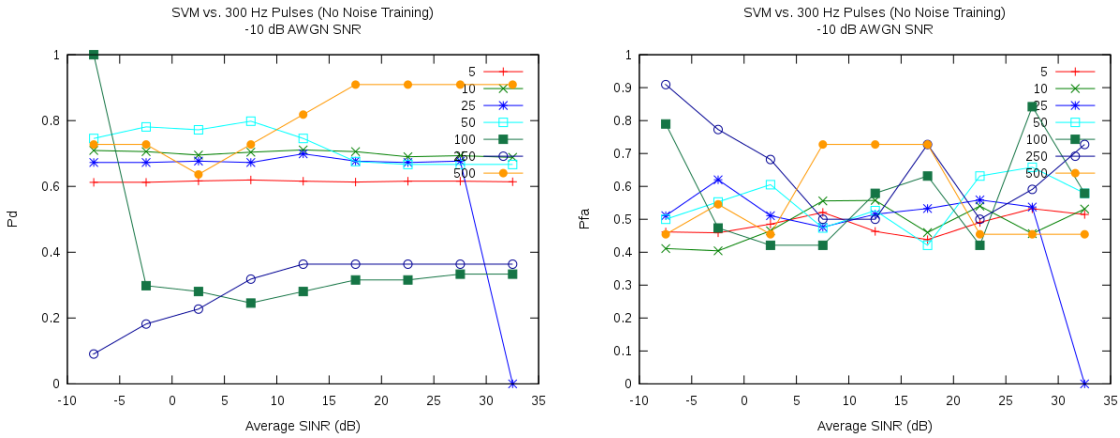

(a) P_d **(b)** P_{fa}

Figure A.117: *SVM Detector with No Noise Training vs. 300Hz Pulses, -10 dB AWGN SNR*

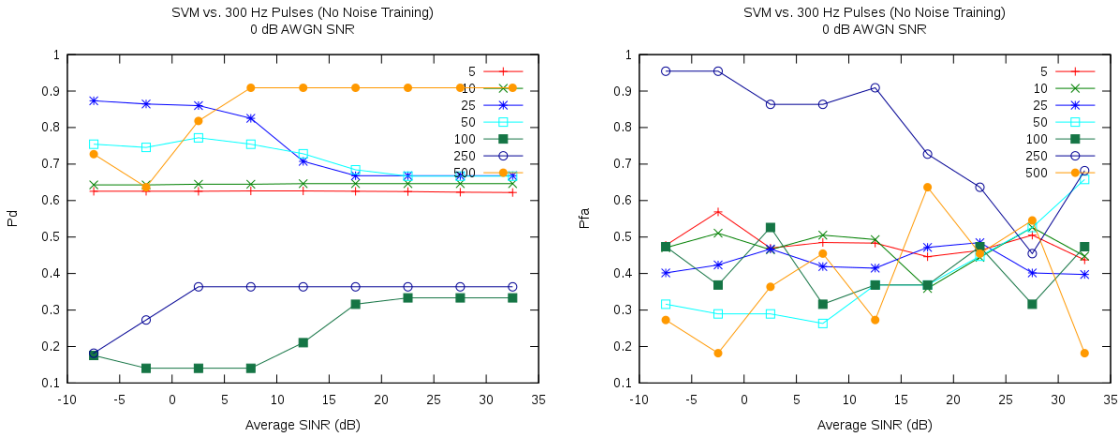

(a) P_d **(b)** P_{fa}

Figure A.118: *SVM Detector with No Noise Training vs. 300Hz Pulses, 0 dB AWGN SNR*

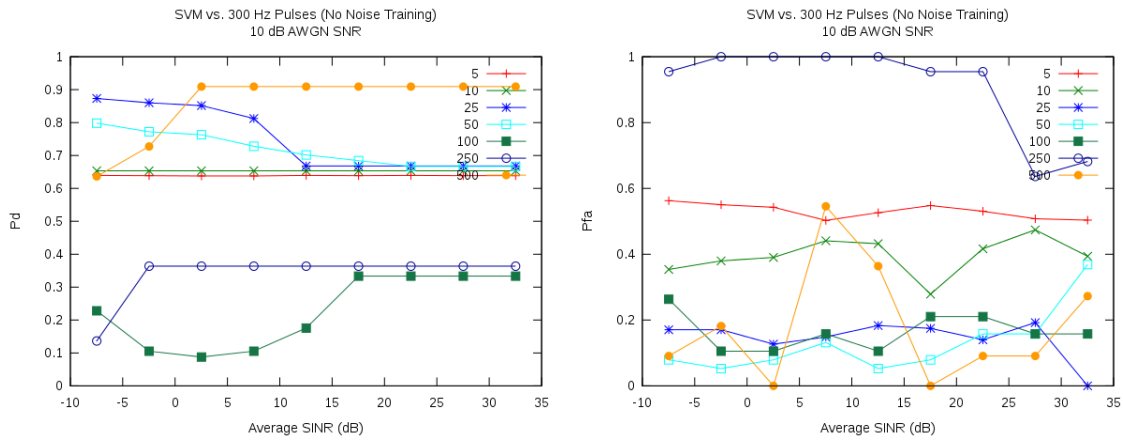

(a) P_d **(b)** P_{fa}

Figure A.119: *SVM Detector with No Noise Training vs. 300Hz Pulses, 10 dB AWGN SNR*

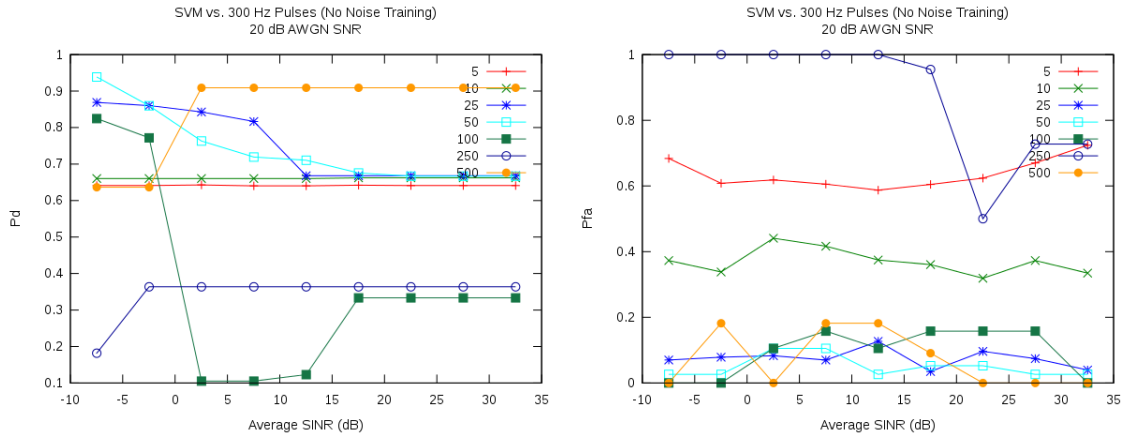

(a) P_d **(b)** P_{fa}

Figure A.120: *SVM Detector with No Noise Training vs. 300Hz Pulses, 20 dB AWGN SNR*

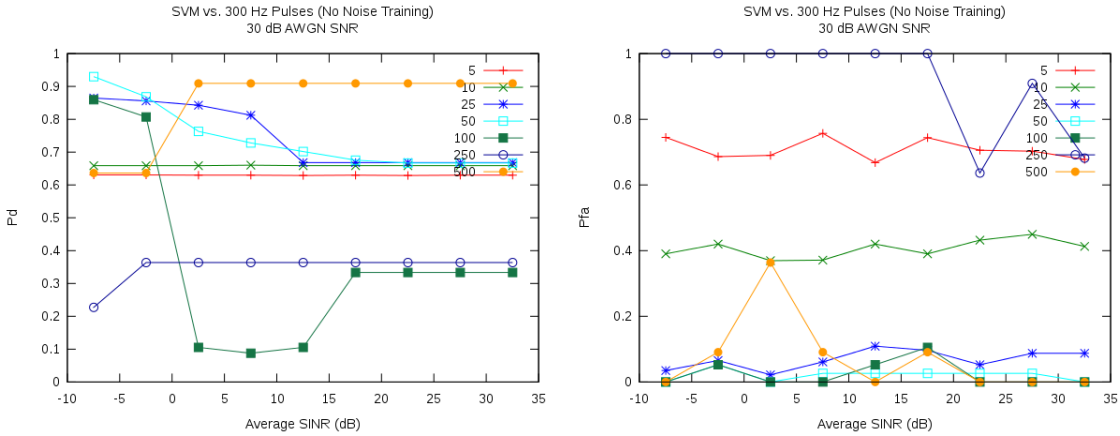

(a) P_d **(b)** P_{fa}

Figure A.121: *SVM Detector with No Noise Training vs. 300Hz Pulses, 30 dB AWGN SNR*

A.7 Support Vector Machine - 0dB AWGN Training

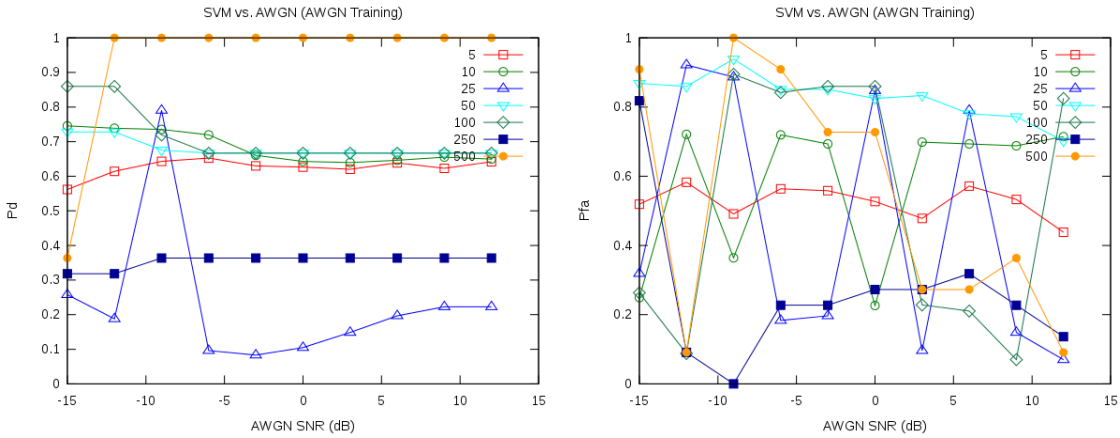

(a) P_d **(b)** P_{fa}

Figure A.122: *SVM Detector with 0dB AWGN Training vs. AWGN*

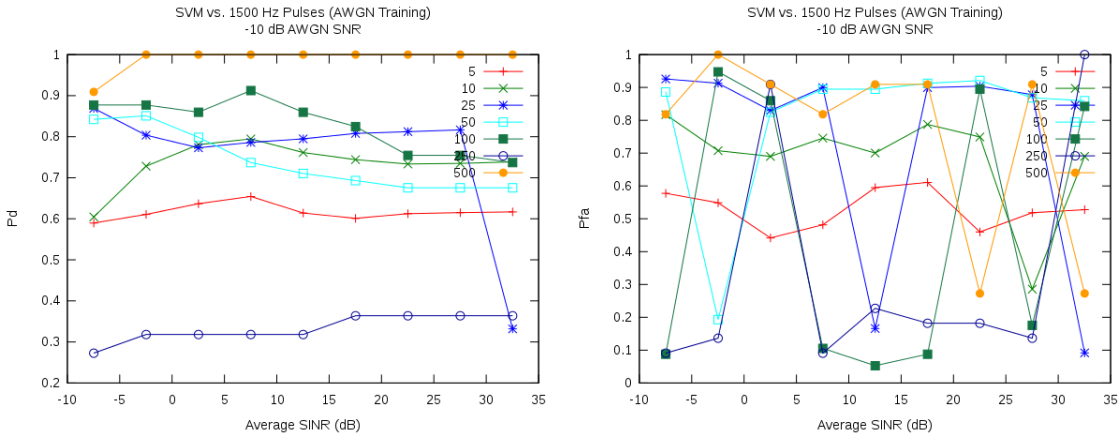

(a) P_d **(b)** P_{fa}

Figure A.123: *SVM Detector with 0dB AWGN Training vs. 1500Hz Pulses, -10 dB AWGN SNR*

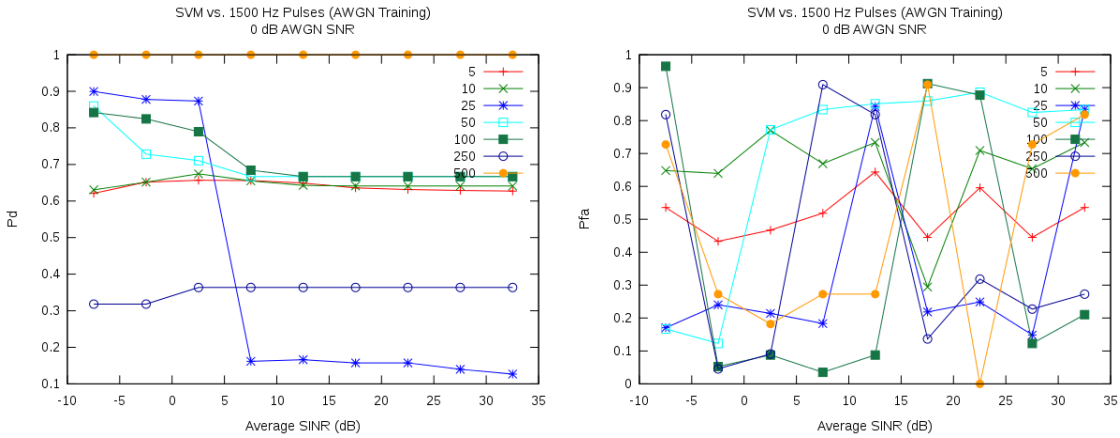

(a) P_d **(b)** P_{fa}

Figure A.124: *SVM Detector with 0dB AWGN Training vs. 1500Hz Pulses, 0 dB AWGN SNR*

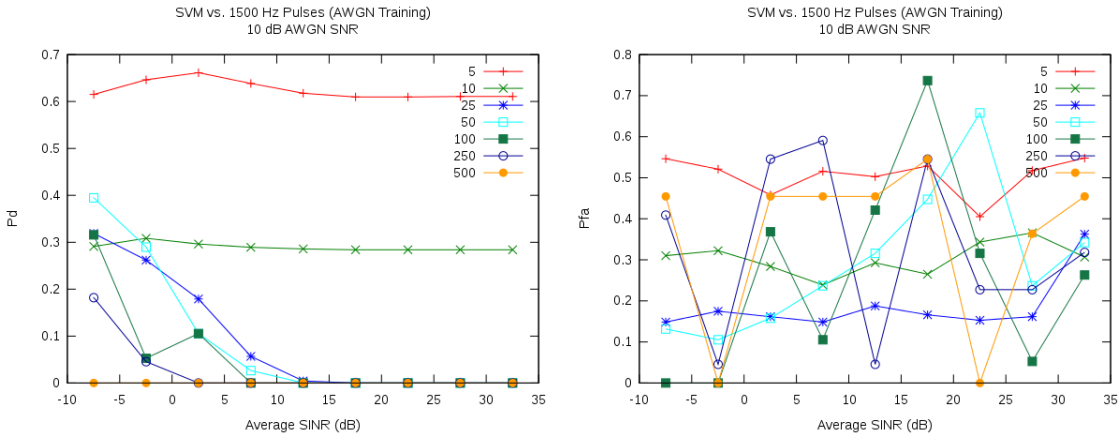

(a) P_d **(b)** P_{fa}

Figure A.125: *SVM Detector with 0dB AWGN Training vs. 1500Hz Pulses, 10 dB AWGN SNR*

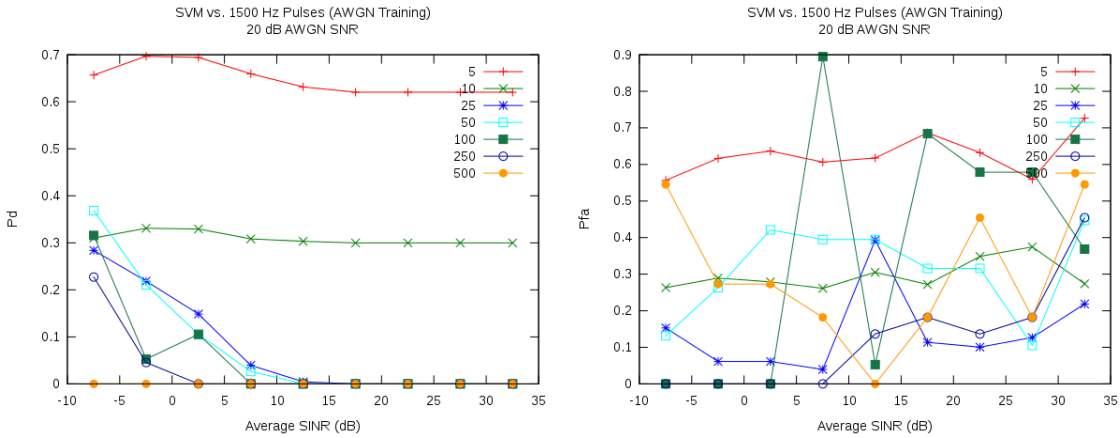

(a) P_d **(b)** P_{fa}

Figure A.126: *SVM Detector with 0dB AWGN Training vs. 1500Hz Pulses, 20 dB AWGN SNR*

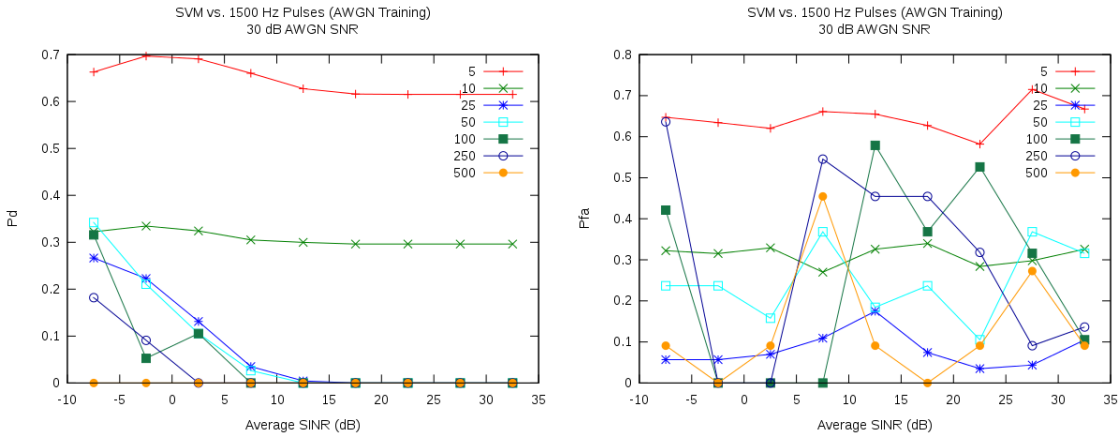

(a) P_d **(b)** P_{fa}

Figure A.127: *SVM Detector with 0dB AWGN Training vs. 1500Hz Pulses, 30 dB AWGN SNR*

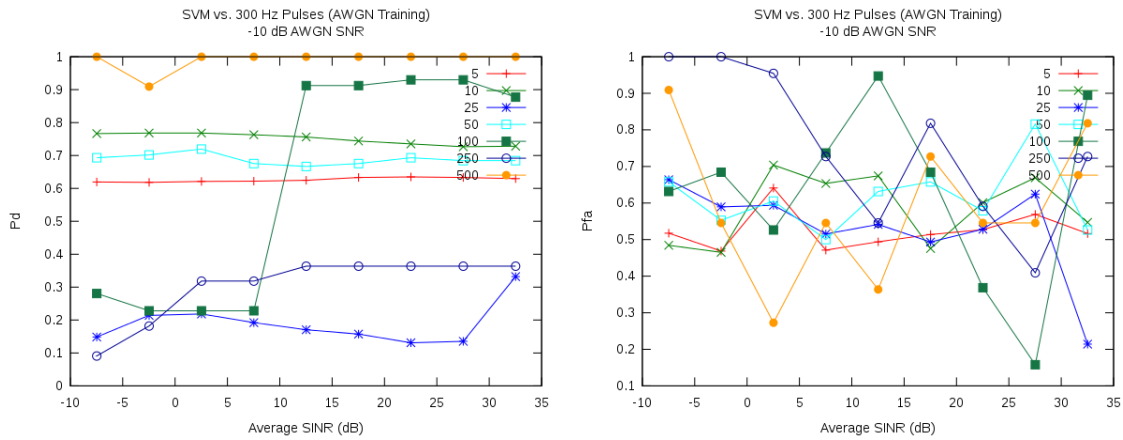

(a) P_d **(b)** P_{fa}

Figure A.128: *SVM Detector with 0dB AWGN Training vs. 300Hz Pulses, -10 dB AWGN SNR*

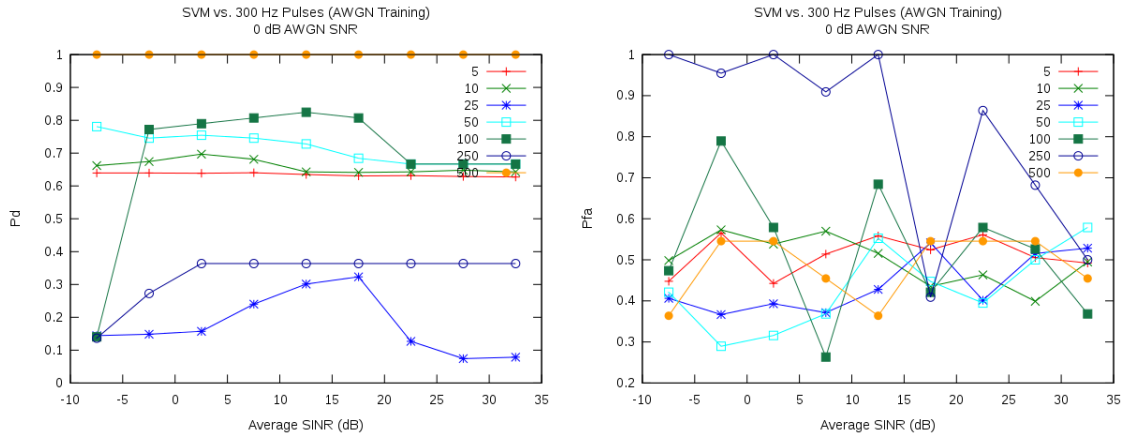

(a) P_d **(b)** P_{fa}

Figure A.129: *SVM Detector with 0dB AWGN Training vs. 300Hz Pulses, 0 dB AWGN SNR*

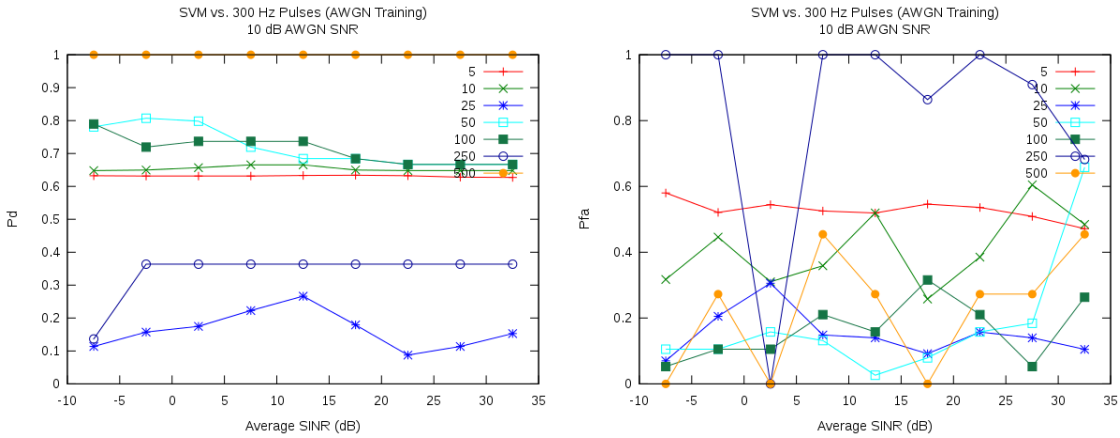

(a) P_d **(b)** P_{fa}

Figure A.130: *SVM Detector with 0dB AWGN Training vs. 300Hz Pulses, 10 dB AWGN SNR*

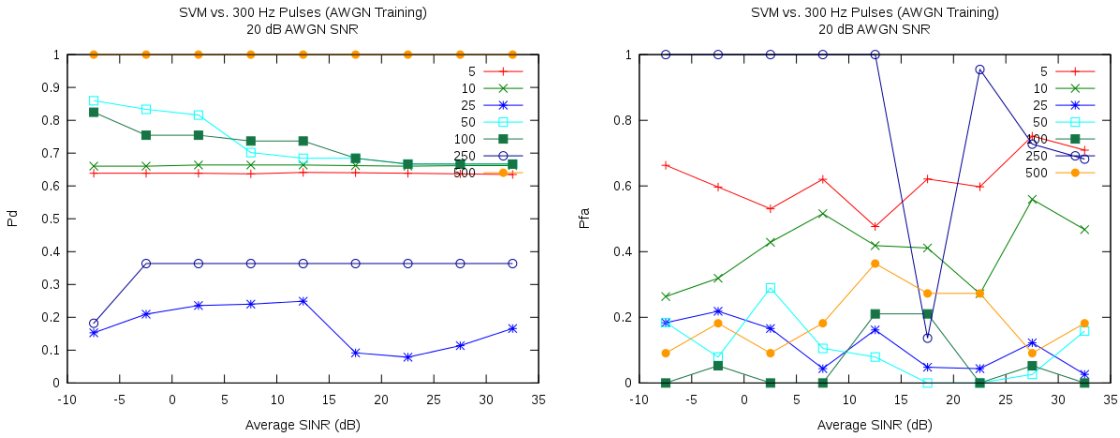

(a) P_d **(b)** P_{fa}

Figure A.131: *SVM Detector with 0dB AWGN Training vs. 300Hz Pulses, 20 dB AWGN SNR*

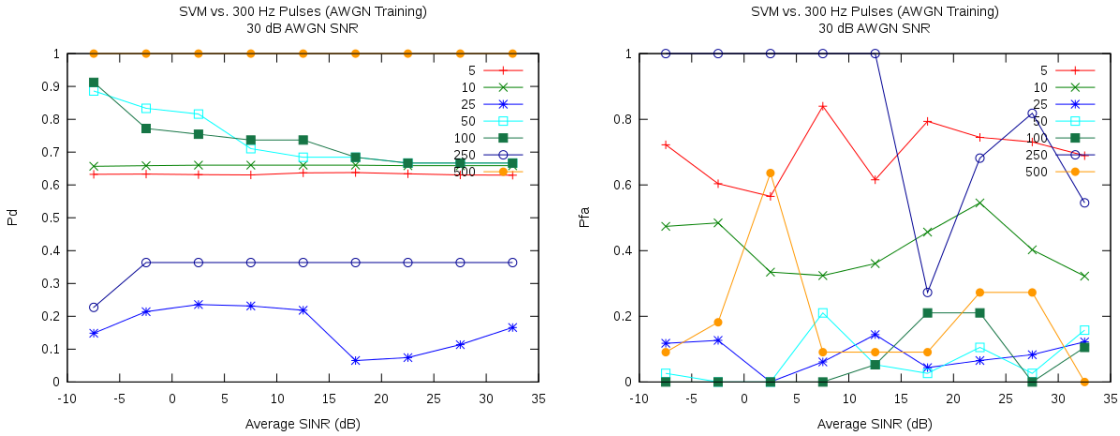

(a) P_d **(b)** P_{fa}

Figure A.132: *SVM Detector with 0dB AWGN Training vs. 300Hz Pulses, 30 dB AWGN SNR*

A.8 Support Vector Machine - 0dB SINR Pulse Training

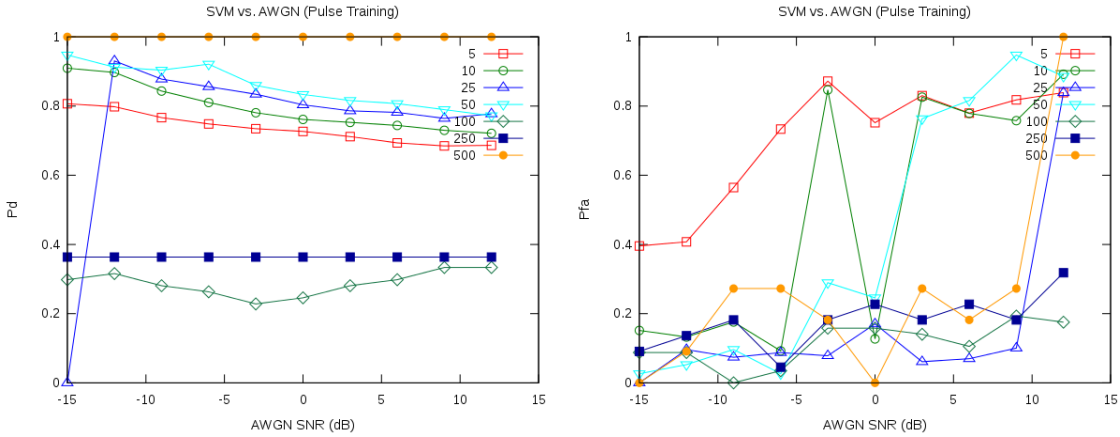

(a) P_d **(b)** P_{fa}

Figure A.133: *SVM Detector with 0dB SINR Pulse Training vs. AWGN*

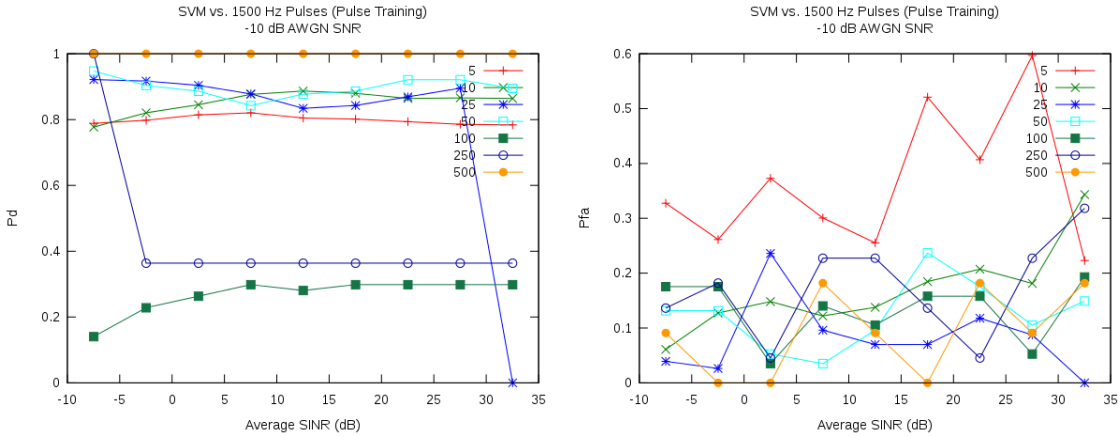

(a) P_d **(b)** P_{fa}

Figure A.134: *SVM Detector with 0dB SINR Pulse Training vs. 1500Hz Pulses, -10 dB AWGN SNR*

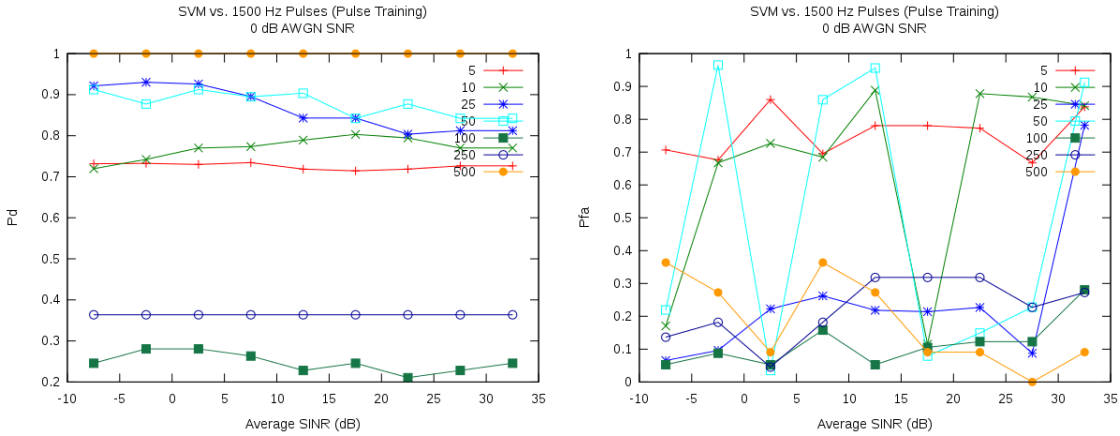

(a) P_d **(b)** P_{fa}

Figure A.135: *SVM Detector with 0dB SINR Pulse Training vs. 1500Hz Pulses, 0 dB AWGN SNR*

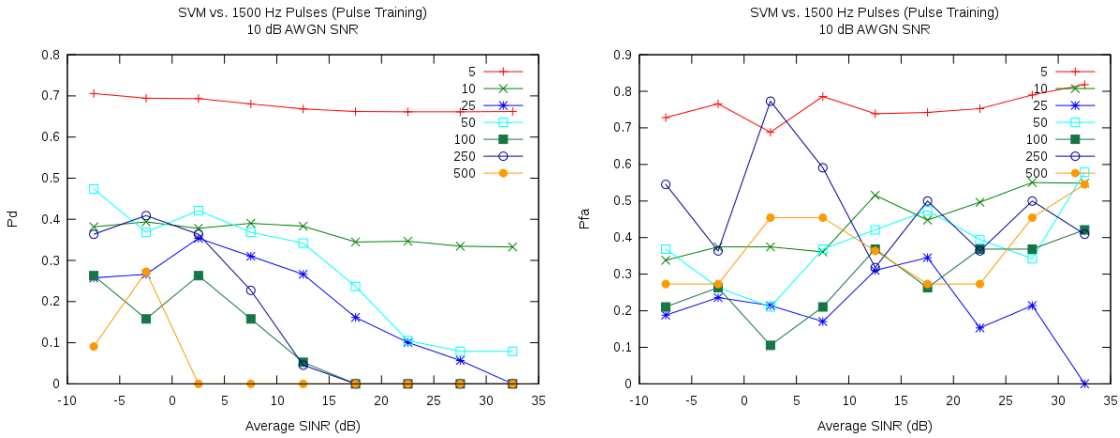

(a) P_d **(b)** P_{fa}

Figure A.136: *SVM Detector with 0dB SINR Pulse Training vs. 1500Hz Pulses, 10 dB AWGN SNR*

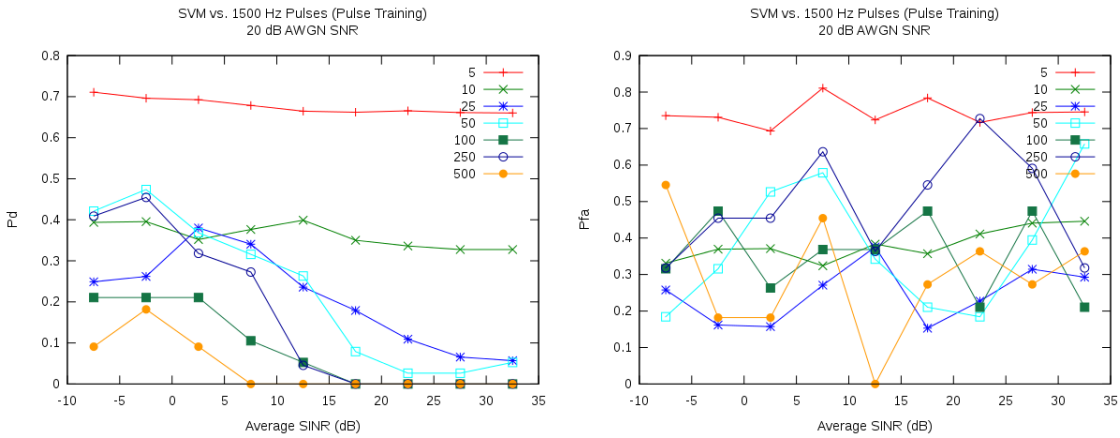

(a) P_d **(b)** P_{fa}

Figure A.137: *SVM Detector with 0dB SINR Pulse Training vs. 1500Hz Pulses, 20 dB AWGN SNR*

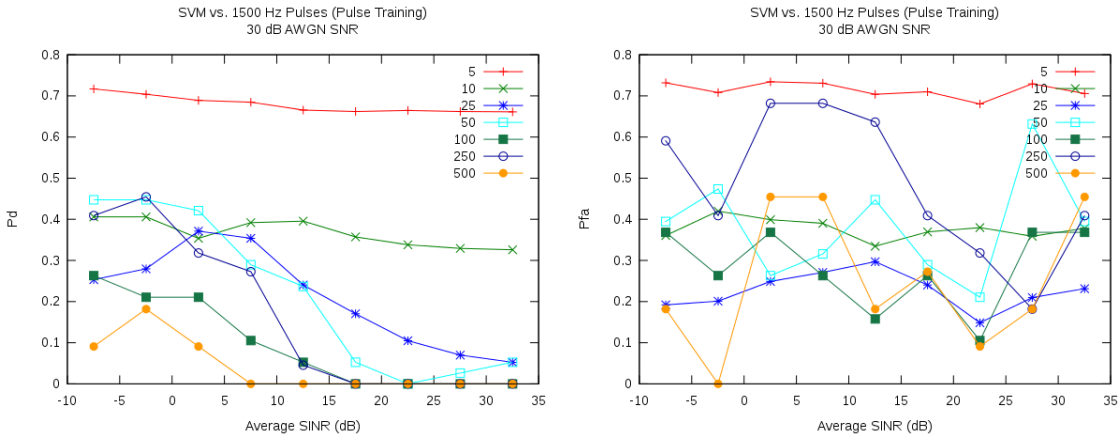

(a) P_d **(b)** P_{fa}

Figure A.138: *SVM Detector with 0dB SINR Pulse Training vs. 1500Hz Pulses, 30 dB AWGN SNR*

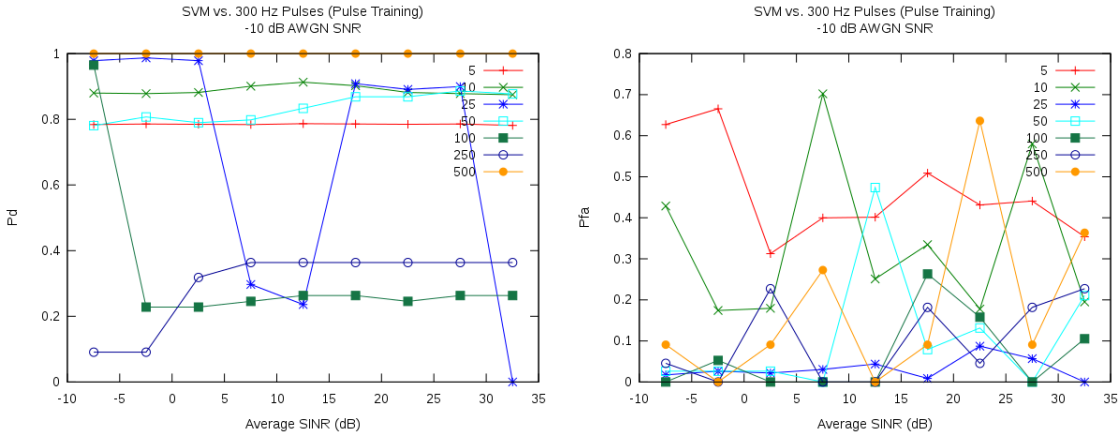

(a) P_d **(b)** P_{fa}

Figure A.139: *SVM Detector with 0dB SINR Pulse Training vs. 300Hz Pulses, -10 dB AWGN SNR*

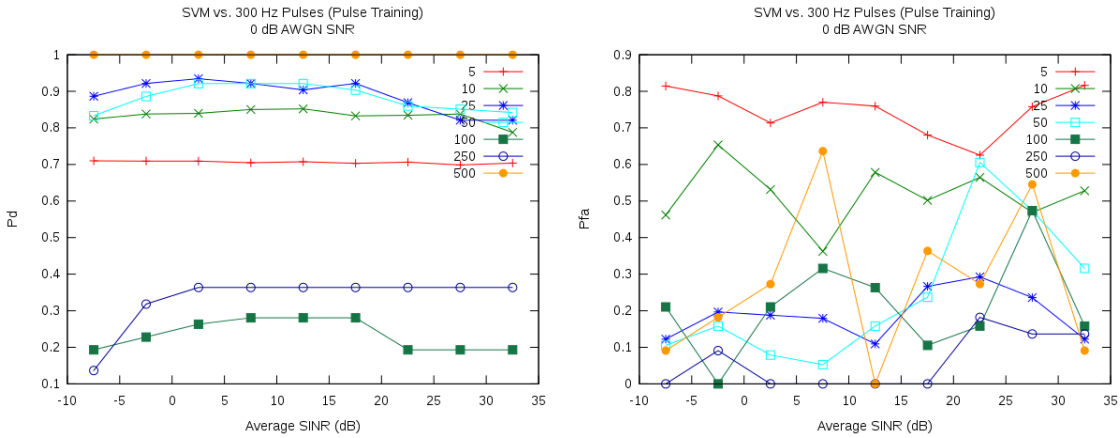

(a) P_d **(b)** P_{fa}

Figure A.140: *SVM Detector with 0dB SINR Pulse Training vs. 300Hz Pulses, 0 dB AWGN SNR*

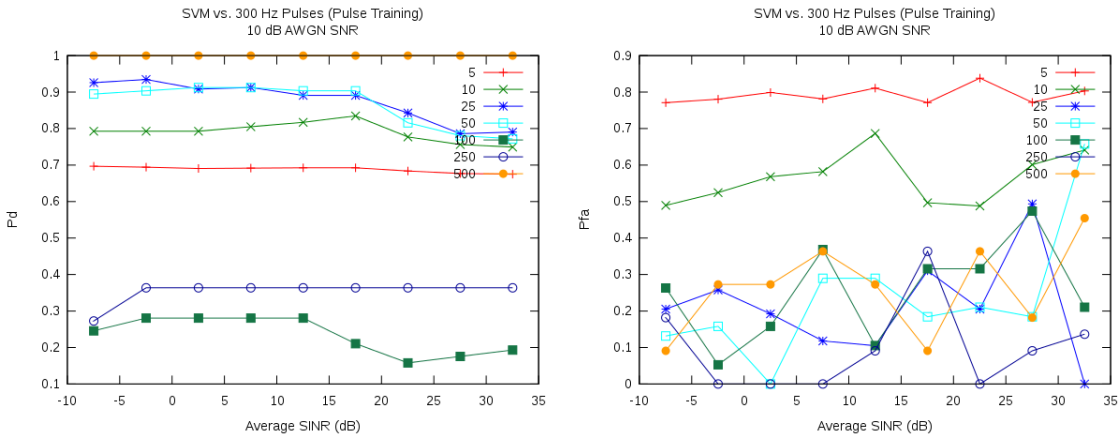

(a) P_d **(b)** P_{fa}

Figure A.141: *SVM Detector with 0dB SINR Pulse Training vs. 300Hz Pulses, 10 dB AWGN SNR*

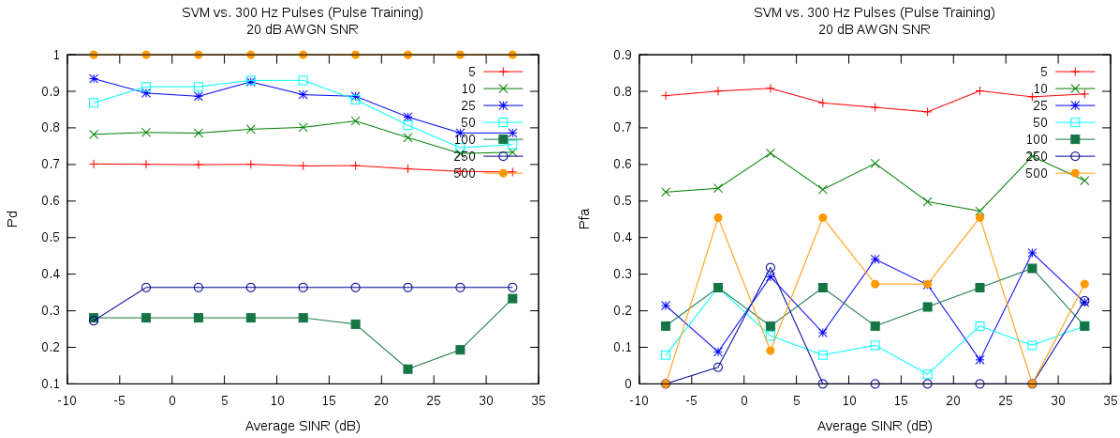

(a) P_d **(b)** P_{fa}

Figure A.142: *SVM Detector with 0dB SINR Pulse Training vs. 300Hz Pulses, 20 dB AWGN SNR*

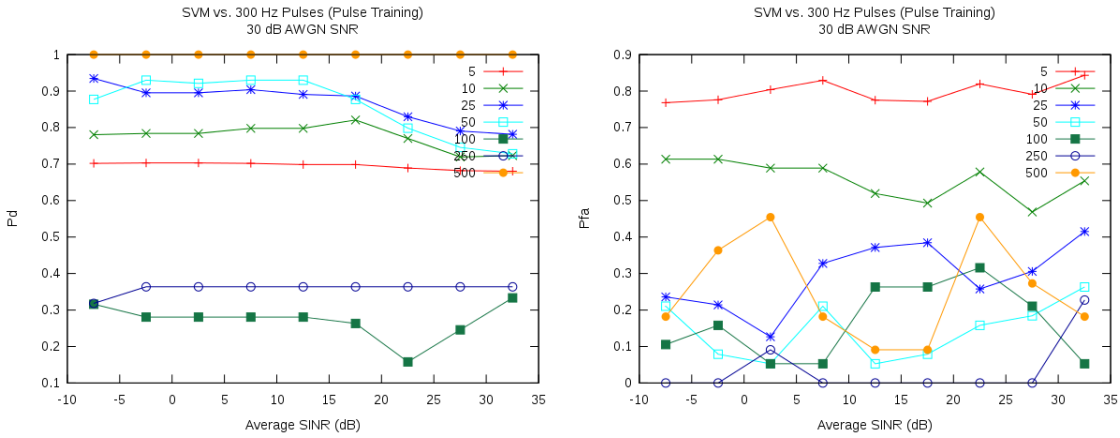

(a) P_d **(b)** P_{fa}

Figure A.143: *SVM Detector with 0dB SINR Pulse Training vs. 300Hz Pulses, 30 dB AWGN SNR*